MAGNETOTELLURIC INVESTIGATION OF THE SANTO DOMINGO BASIN, RIO GRANDE RIFT, NEW MEXICO

A Thesis

Presented to the

Faculty of

San Diego State University

In Partial Fulfillment

of the Requirements for the Degree

Master of Science

in

Geological Sciences

---

by

Peter Karl Winther

Spring 2009

SAN DIEGO STATE UNIVERSITY

The Undersigned Faculty Committee Approves the

Thesis of Peter Karl Winther:

Magnetotelluric Investigation of the Santo Domingo Basin, Rio Grande Rift, New Mexico

_____

George R. Jiracek, Chair
Department of Geological Sciences

_____

Kim Bak Olsen
Department of Geological Sciences

_____

Paul T. Kolen
Department of Electrical and Computer Engineering

_____

Approval Date

DEDICATION

I dedicate this thesis to my mother, Louise L. Winther who never finished her master's program in nursing but instead decided to start a family late in life. I am eternally grateful to her and wish she could still be alive to witness my graduation.

If you never try, you will never succeed.

- Anonymous

Try not. Do or do not, there is no try.

- Yoda

ABSTRACT OF THE THESIS

Magnetotelluric Investigation of the Santo Domingo Basin, Rio Grande Rift, New Mexico

by
Peter Karl Winther
Master of Science in Geological Sciences
San Diego State University, 2009

Magnetotelluric (MT) investigations of the Santo Domingo Basin were made in 2000-2007 to assess the deep stratigraphy and tectonics of an intra rift basin. The studies were conducted during the SAGE (Summer of Applied Geophysical Experience) program to provide 'hands-on' learning experiences for students and to evaluate the local hydrologic regime. Most MT soundings were accomplished using Quantec Geoscience's Titan 24 MT system. The Titan system is a distributed array MT instrument that allows the collection of up to 24 MT soundings simultaneously with a station spacing of 100 m. Sixty-five Titan MT soundings were collected along a 6.4 km-long profile where a petroleum exploration seismic survey was recorded during the 1970's. The MT data were modeled using a smooth, two-dimensional (2-D) inversion code developed by Geosystem, Inc. Modeled resistivity values vary from 2-1000 ohm-m in the 2 - 4.5 km-thick sedimentary section. Resistivities exceed 1000 ohm-m in the basement interpreted to underlie the sediments. The sedimentary sequence indicates three distinct regimes: (1) an upper, unsaturated and freshwater saturated, basin-fill that ranges from 350 - 800 m-deep with resistivities of 8 - 85 ohm-m, (2) a deeper, mostly conductive region with higher brine and/or clay concentrations approximately 3 km thick with resistivities varying between 2 - 100 ohm-m and (3) a resistive sedimentary cover over the crystalline basement that ranges from 100 - 1000 ohm-m. Tectonic interpretations of the 2-D MT inversion model agree with the locations of several fault traces extended into the basin by the U. S. Geological Survey from aeromagnetic interpretations. A geologic structure model for the area includes two grabens with the graben on the west down dropped with respect to the graben on the east.

TABLE OF CONTENTS

PAGE

LIST OF TABLES

PAGE

LIST OF FIGURES

PAGE

ACKNOWLEDGEMENTS

I would like to thank my advisor, Dr. George Jiracek, whose guidance, constructive criticism, praise and financial assistance made this work possible. I still may not understand everything there is to know about magnetotellurics but I have a strong foundation. I would also like to thank Dr. Kim Olsen and Dr. Paul Kolen for their edits.

This work would not be possible without the cooperation of Cochiti people who graciously allowed SAGE to operate on their lands and to publish the findings. I would like to recognize Lee Suina, Jacob Pecos, and Gary Valdo from the Cochiti Pueblo Department of Natural Resources and Conservation. All the faculty of SAGE past and present deserve my gratitude as well. I would like to give thanks to the many companies that support SAGE through financial assistance, equipment donation, and expertise. I would especially like to recognize Bill Doerner formally from Quantec Geoscience, Mauricio Berrios from Quantec Geoscience, and Scott Urquhart from Zonge Engineering and Research. The students of SAGE who assisted in the instrument setup and data collection deserve my thanks.

I would like to thank my father, Karl Winther, for instilling the curiosity of discovering how things work which lead to my studies in the sciences. I again would like to thank my mother for sacrificing so much so that my brother and I grew up in a good home. I would like to thank all the friends that I have made here at SDSU and at ASU that helped me along the way. I would especially like to thank my officemate, Andrew Gritz, for careful edits of several of the chapters.

CHAPTER 1

INTRODUCTION

The basins of the Rio Grande rift have been the study of the Summer of Applied Geophysical Experience (SAGE) program since the program's conception in 1983. Since 1990 SAGE has been a National Science Foundation (NSF) REU (research for undergraduates) site that immerses students in exploration geophysics. At SAGE both graduate and undergraduate students install and operate scientific instruments to record geophysical data. Data are then computer-modeled and interpreted to yield geologically consistent results. Types of data collected include seismic reflection and refraction, gravity, magnetic, transient electromagnetic (TEM), magnetotelluric (MT), and various other electromagnetic methods.

Pertinent data for this investigation of the northern Santo Domingo Basin include MT, TEM, and gravity data that were collected by the students during 2000-2003, 2005, and 2007 SAGE programs. Quesada (2004), in his master thesis at San Diego State University, presented the results from SAGE 2000-2003 years. Presented here will be a reevaluation of these data as well as modeling of new data from SAGE 2005 and 2007. The new data were collected adjacent to the older data, mainly within the northern part of the Santo Domingo Basin to the west of where the Santa Fe River incises into the La Bajada Fault escarpment. The SAGE program relies on its industry partners for partial funding and major equipment donations and as such was fortunate to have Quantec Geoscience's Titan 24 distributed array magnetotelluric system at SAGE for the 2002 and 2005 field seasons. During the 2002

season, 41 Titan MT sites were occupied in the Santo Domingo Basin along a bearing of N73W, 107º azimuth. During the 2005 season, an additional 24 Titan MT sites were occupied adjacent to the 2002 data, along the same bearing and further west into the basin. An additional 45 MT soundings bringing the total to 110 MT soundings have been recorded in the SAGE MT study area during the above mentioned SAGE programs.

The main purpose of SAGE is educating students in exploration geophysical methods but one secondary purpose is the geophysical investigation of the basins that comprise the Rio Grande rift system. The subsurface geology of the northern Santo Domingo Basin is complex and not well-understood. The basin is of rising economic concern to the cities and towns adjacent to it as well as the Native Americans that inhabit it. The geophysical data collected during the SAGE program highlights stratigraphic as well as structural features in the near-surface down to a few kilometers depth provided that contrasts in the measured/modeled physical parameters exist.

The identification of stratigraphic relationships between subsurface units and the evaluation of recently projected faults into the basin by the U. S. Geological Survey (USGS) based on the analysis of aeromagnetic data (Minor, 2006) are of crucial importance in understanding the basin as a whole and any future economic plans of the Native Americans. Identifying the contact between the electrically resistive late to middle Cenozoic basin-fill sediments that contain fresh water aquifers and the highly conductive early Cenozoic to Paleozoic sedimentary rocks that contain poorer quality aquifers is of vital importance in understanding the hydrogeology of the basin. The contacts between the highly conductive early Cenozoic sedimentary sequence and the more resistive, deeper Mesozoic and late to middle Paleozoic sedimentary sequence and the even more resistive, deeper still, early

Paleozoic limestone and Precambrian crystalline basement sequence may not be as economically important but are still important for understanding the geologic and tectonic history of the basin.

A complete structural interpretation of the basin will have to await further work. However, an evaluation of hypothesized faults along SAGE MT survey lines in the basin is important because this impacts the shape, extent, and confinement of any aquifer containing units. Two slightly different structural interpretations have been proposed for the subsurface structure beneath the survey. One model presented by Quesada (2004) includes two parallel, dipping faults displaying offset layers and two igneous intrusive bodies on each end of the survey lines. The other model is a graben/horst structure put forth by Minor (2006) from the USGS. The present geophysical results, mainly MT, are not able to strictly resolve this question at this time, however, a modification of both previous models is proposed.

CHAPTER 2

PREVIOUS WORK

INTRODUCTION

The geologic history of the Santo Domingo Basin is closely tied to the tectonic history of the Rio Grande rift. A broad review of that tectonic history as well as the basin's geographic and geologic location within the rift system is necessary to provide the context for understanding the basin as a whole. The basin is a complex feature based on its location in the rift system. The subsurface structure of the Santo Domingo Basin is not as well studied as the neighboring basins to the north and south. Recent geophysical data highlights what is known structurally about the basin. After reviewing the structure and tectonic history of the basin, the basin sediments and their depositional history will be discussed. A combined interpreted history of the Santo Domingo Basin is then presented.

GEOLOGIC AND TECTONIC HISTORY

The Rio Grande rift is a prominent continental rift present in the southwestern United States. The rift is composed of a series of asymmetrical grabens that extend for more than a 1000 km from Chihuahua, Mexico, to central Colorado (Figure 1). It is a relatively young continental rift, being only 30 Ma (Olsen et al., 1987). However, the basement crust here has experienced several tectonic events before the rifting. These events include the Proterozoic collisional tectonics of island arc accretion and the associated Grenville orogeny as well as the later (late Devonian – early Mississipian) Antler orogeny.

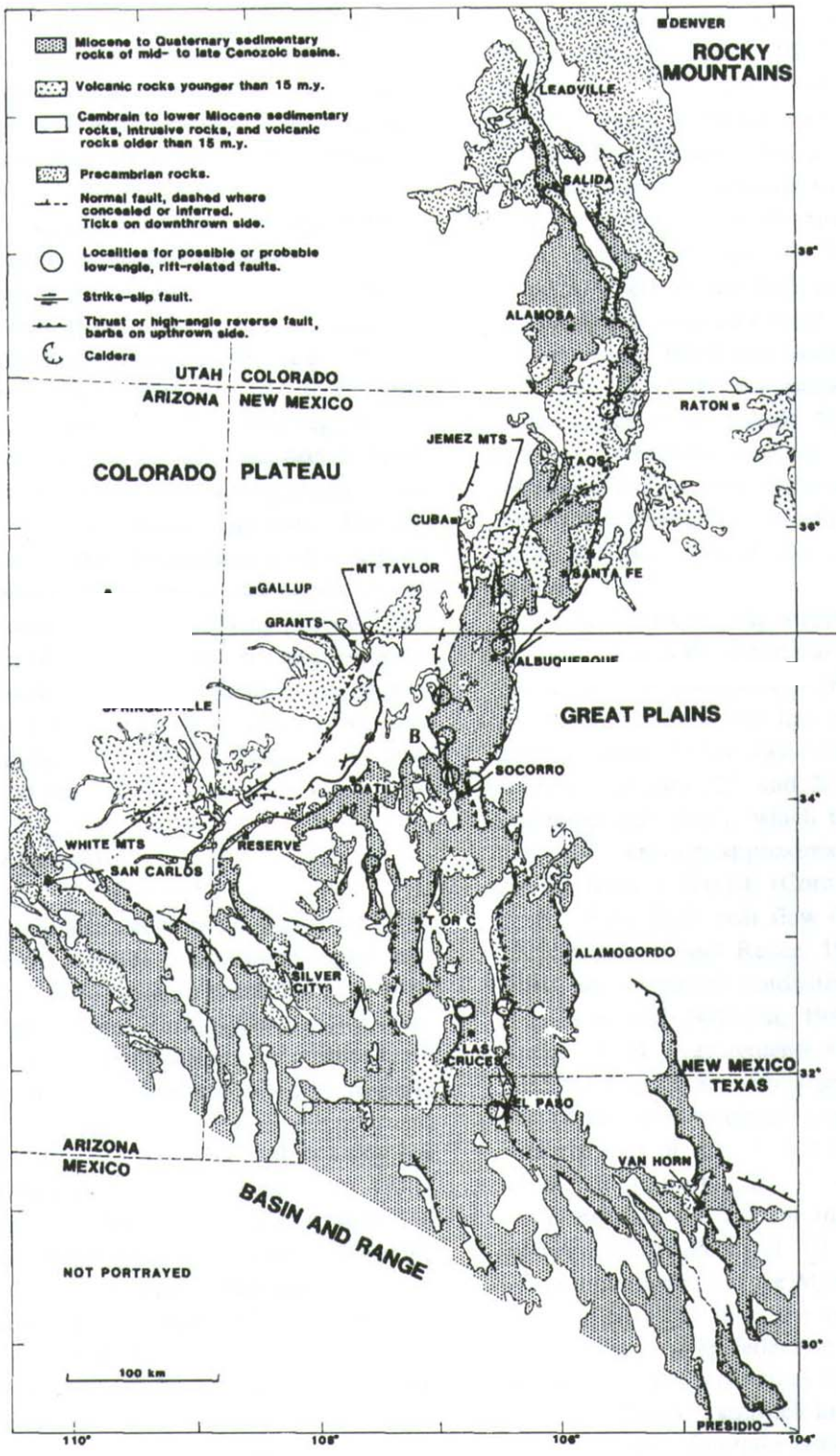

Figure 1. Geologic map of the Rio Grande rift (modified from Olsen et al., 1987).

The history of the rift is tied closely to the subduction of the Farallon Plate beneath the western edge of the North American Plate. The angle of subduction for the Farallon Plate varied from steep to shallow during the late Mesozoic to Cenozoic. The Laramide orogeny (40 – 70 Ma) was the result of a shallow subducting angle and resulted in volcanic activity during this time in the southwestern U.S. due, in part, to the detachment of a portion of the Farallon slab as the plate continued to be subducted (Baldridge et al., 1991). These events contributed to the weakening of the crust beneath the rift's initial location. The structural features of the rift formed as a result of back arc spreading of this weakened crust.

The rift developed during two rapid extensional events accompanied by a lull in extensional activity between them. The earlier event was from 30-18 Ma, Oligocene-early Miocene (Olsen et al., 1987). The volcanic rocks used to date this event are dominantly calc-alkaline intermediate to silicic in composition (Baldridge et al., 1991). This event resulted in a broad, relatively shallow basin bound by low-angle faults. The extension was focused along a NE-SW direction on the order of 30-50% (Keller et al., 1991). The second event was from 10-3 Ma, middle Miocene-Holocene (Olsen et al., 1987). Volcanic rocks used to date this event are alkalic and tholeiitic basaltic in composition (Baldridge et al., 1991). This event resulted in a north- to northeast-trending series of asymmetrical grabens bound by high-angle faults and was part of the Basin and Range extensional event. The extension was on the order of 5-20% (Keller et al., 1991). During this last event a regional uplift of about 1 km occurred and seems to be related to the uplifting of the Colorado Plateau region.

PHYSIOGRAPHIC FEATURES OF THE RIFT VALLEY BASINS

The rifting and uplift resulted in the Rio Grande rift valley presenting itself as a series of four right-stepping, offset basins in New Mexico and southern Colorado (Figure 2). In order from north to south are the San Luis Basin in southern Colorado and northern New Mexico, the Espanola Basin, which is slightly offset to the west, the Santo Domingo Basin to the southwest of Santa Fe, which is again offset to the west, and the Albuquerque-Belen Basin. Rift flank uplifts include the Laramide-age Sangre de Cristo and younger Sandia Mountains on the eastern side of the rift and the San Juan and Jemez Mountains on the western side of the rift.

Focusing on the Santo Domingo Basin, several extra-basin and intra-basin geographic and geologic features are significant (Figure 3). Extra-basin uplifts include the Jemez and Sandia Mountains, the Cerrillos uplift, and the La Bajada fault-zone escarpment. Major drainage systems in the basin include the Rio Grande, Jemez River, and Santa Fe River. Volcanic features include the extra-basin Valles Caldera and Cerros del Rio volcanic field and the intra-basin Santa Ana Mesa volcanic field.

SANTO DOMINGO BASIN STRUCTURE

From recent geophysical work by the USGS (Minor, 2006), a clearer picture of the structure of the basin has emerged. The boundaries of the basin are defined in an isostatic residual gravity model (Figure 4). The basin has a southwest northeast elongation, whereas most of the faults trend north to northwest. The model also displays several subsurface features such as the Ziana Horst to the southeast, the Hagan Embayment to the east, and the

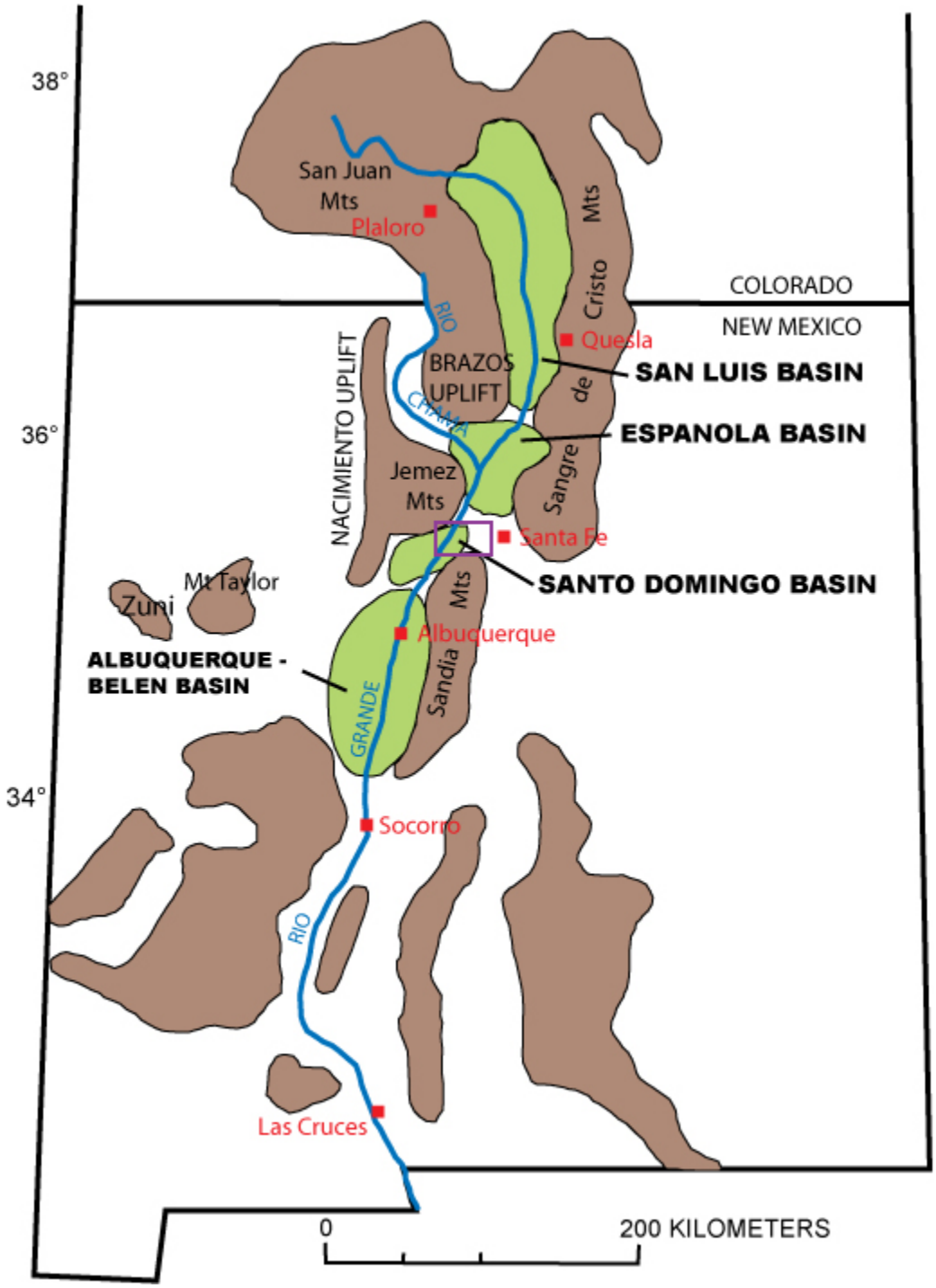

Figure 2. Basin map of the Rio Grande rift. The four major basins are the San Luis Basin in the north, the Espanola Basin in the middle, the Santo Domingo Sub-basin in the middle, and the Albuquerque-Belen Basin to the south. Purple box indicates location of study area (modified from Manley, 1979).

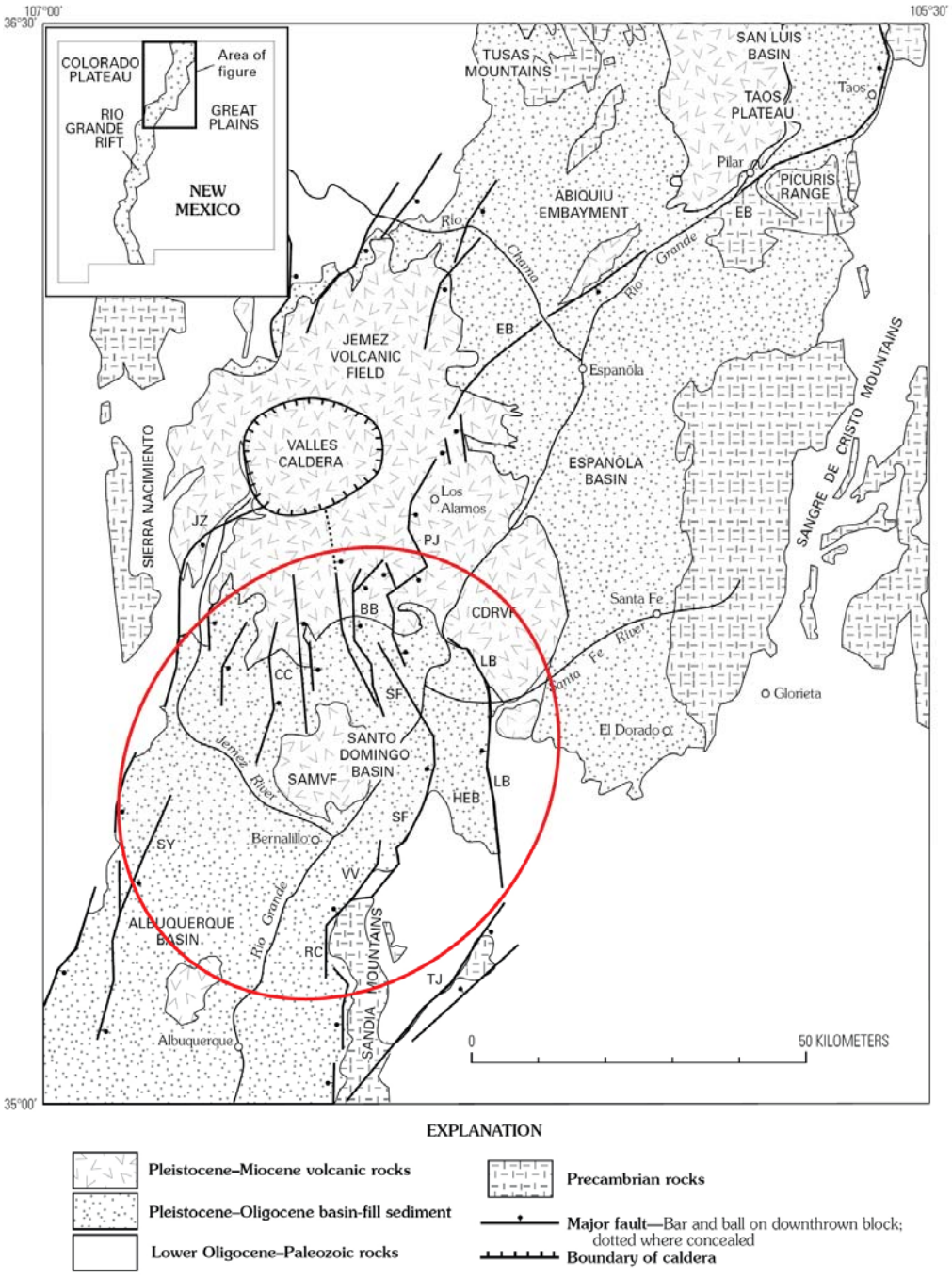

Figure 3. The Santo Domingo Basin and near-by geologic features. The Santo Domingo Basin is inside the red oval. Abbreviations are: BB, Bearhead Basin; CC, Cañada de Cochiti fault; CDRVF, Cerros del Rio volcanic field; EB, Embudo fault zone; HEB, Hagan embayment; JZ, Jemez fault; LB, La Bajada fault zone; PJ, Pajarito fault zone; RC, Rincon fault; SAMVF, Santa Ana Mesa volcanic field; SF, San Francisco fault; SY, San Ysidro fault; TJ, Tijeras fault zone; VV, Valley View fault (modified from Minor, 2006).

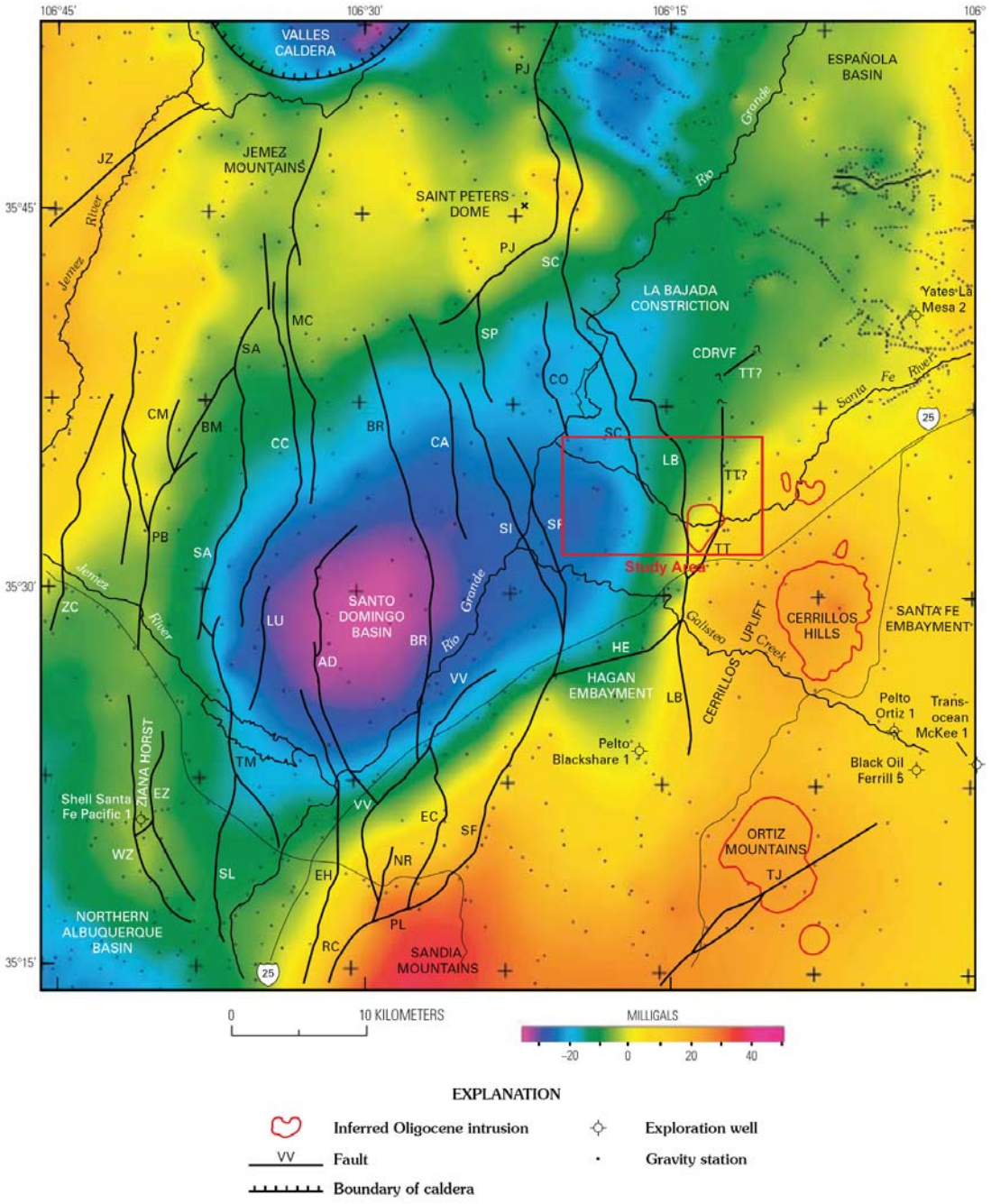

Figure 4. Isostatic residual gravity model for the Santo Domingo Basin. Fault abbreviations are: AD, Algodones; BM, Borrego Mesa; BR, Borrego; CA, Camada; CC, Cañada de Cochiti; CM, Chamisa Mesa; CO, Cochiti; EC, Escala; EH, East Heights; EZ, East Ziana; HE, Hagan Embayment; JZ, Jemez; LB, La Bajada; LU, Luce; MC, Mesita Cocida; NR, North Rincon; PB, Pico Butte; PJ, Pajarito; PL, Placitas; RC, Rincon; SA, Santa Ana; SC, Sanchez; SF, San Francisco; SI, Sile; SL, South Luce; SP, South Pajarito; TJ, Tijeras; TM, Tamaya; TT, Tetilla; VV, Valley View; WZ, West Ziana; ZC, Zia County Dump (modified from Minor, 2006).

La Bajada constriction to the northeast. These subsurface features indicate that the Santo Domingo Basin in not a closed basin which has certain hydrogeologic implications.

The USGS upper Cenozoic basin fill thickness model (Figure 5) indicates that the deeper deposits in the basin coincide with the Santa Ana Mesa volcanic field and that there is a shallow northeast-trending, 10–14 km wide trough that projects under the Cerros del Rio volcanic field (Minor, 2006). A geophysical model (Figure 6) based on gravity and aeromagnetic data of the northern part of the basin presents a complex horst and graben structure. It is noted by the USGS researchers that the model along their cross section does cut the faults obliquely (Minor, 2006).

These results agree with the hypothesis that the basin is bounded by steeply dipping faults with large vertical displacements on the eastern side and bounded by a homocline or series of down-to-basin faults on the western side (Minor, 2006). An important structural observation is that the Santo Domingo Basin is located between the gently eastward tilted Albuquerque Basin and the westward tilted Espanola Basin (Minor, 2006).

Aeromagnetic data from the northern part of the basin were used to try and extend several surface mapped fault traces into the subsurface of the basin (Figure 7). These data as well as previous work were compiled to make an updated fault map of the basin (Figure 8). In the USGS report several important observations were made about the fault patterns: (1) basin bounding faults along the northwestern and southeastern margins of the basin are parallel to the northeastern elongation, and (2) intra-basin faults close to the basin center form a symmetric, semi-concentric, inward dipping fault pattern (Minor, 2006).

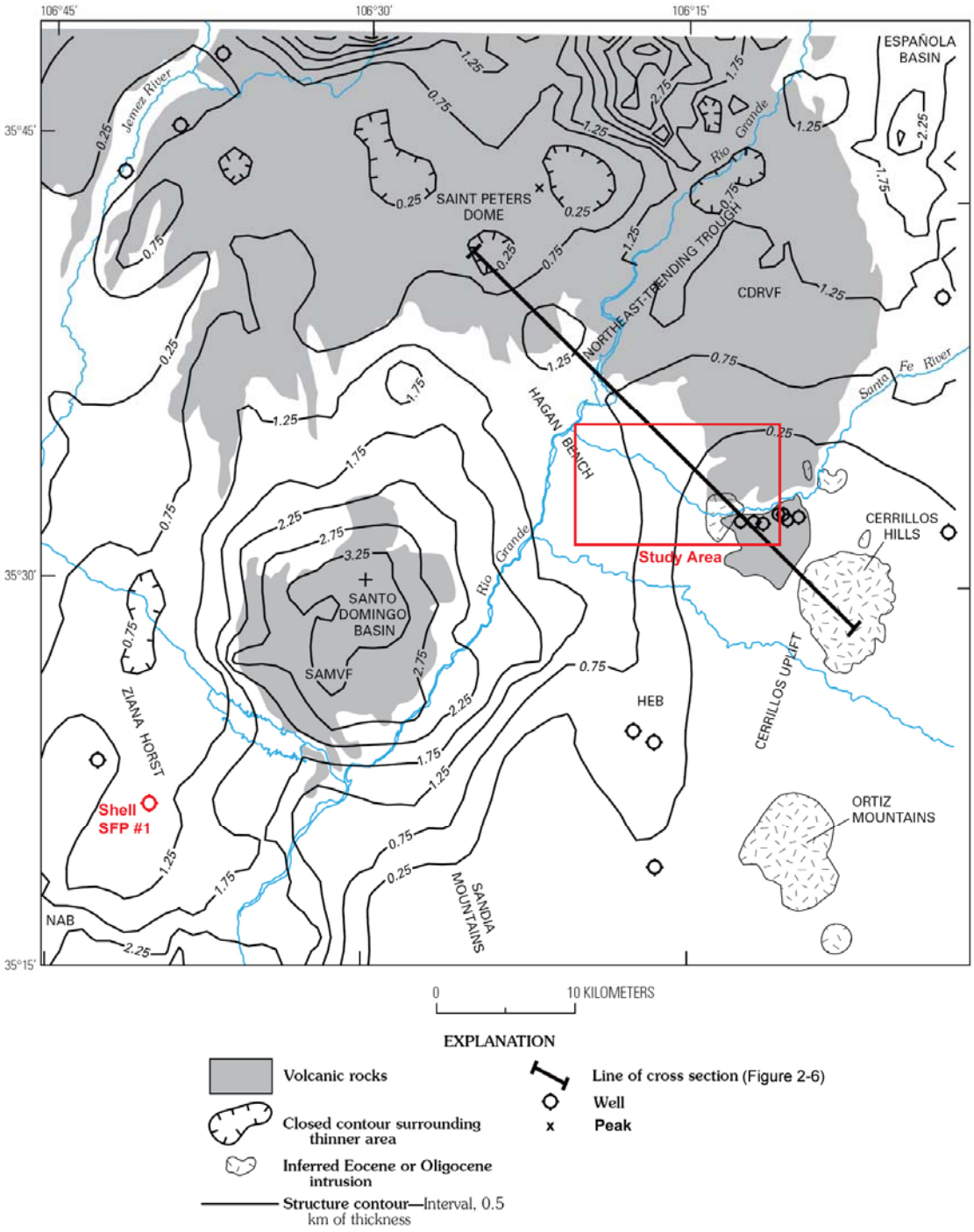

Figure 5. Estimated thickness of upper Cenozoic basin fill in Santo Domingo Basin. Basin-fill is primarily of Santa Fe Group sediments interbedded with basalts erupted from the Cerros del Rio (CDRVF) and Santa Ana Mesa (SAMVF) volcanic fields. Abbreviations are: HEB, Hagan embayment; NAB, northern Albuquerque Basin (modified from Minor, 2006).

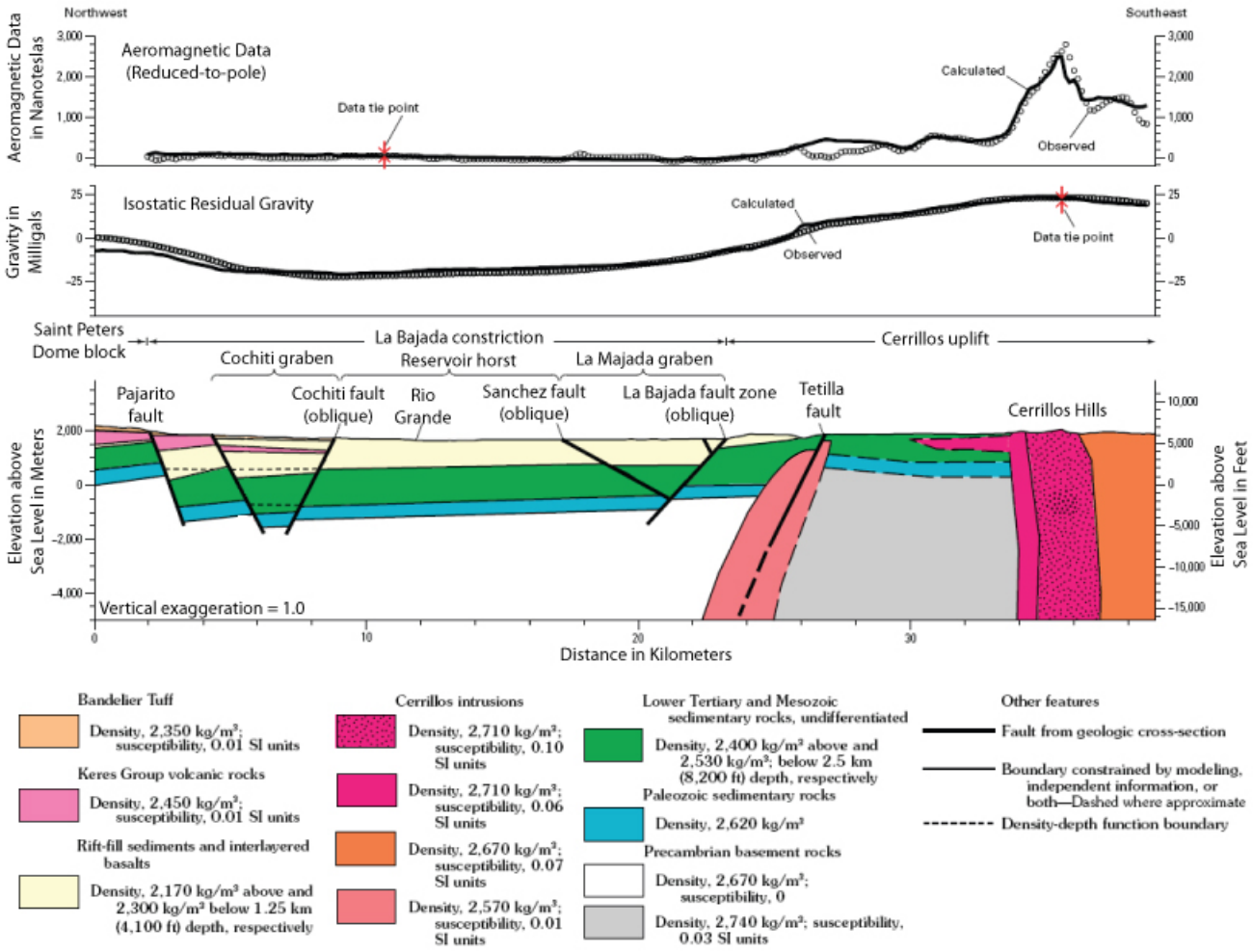

Figure 6. Geophysical model based on observed isostatic residual gravity and reduced-to-pole aeromagnetic data. The model is located along the cross section in Figure 5. The La Bajada constriction, the northeastern end of the Santo Domingo Basin, is modeled as consisting of the Cochiti graben, the Reservoir horst, and the La Bajada graben (modified from Minor, 2006).

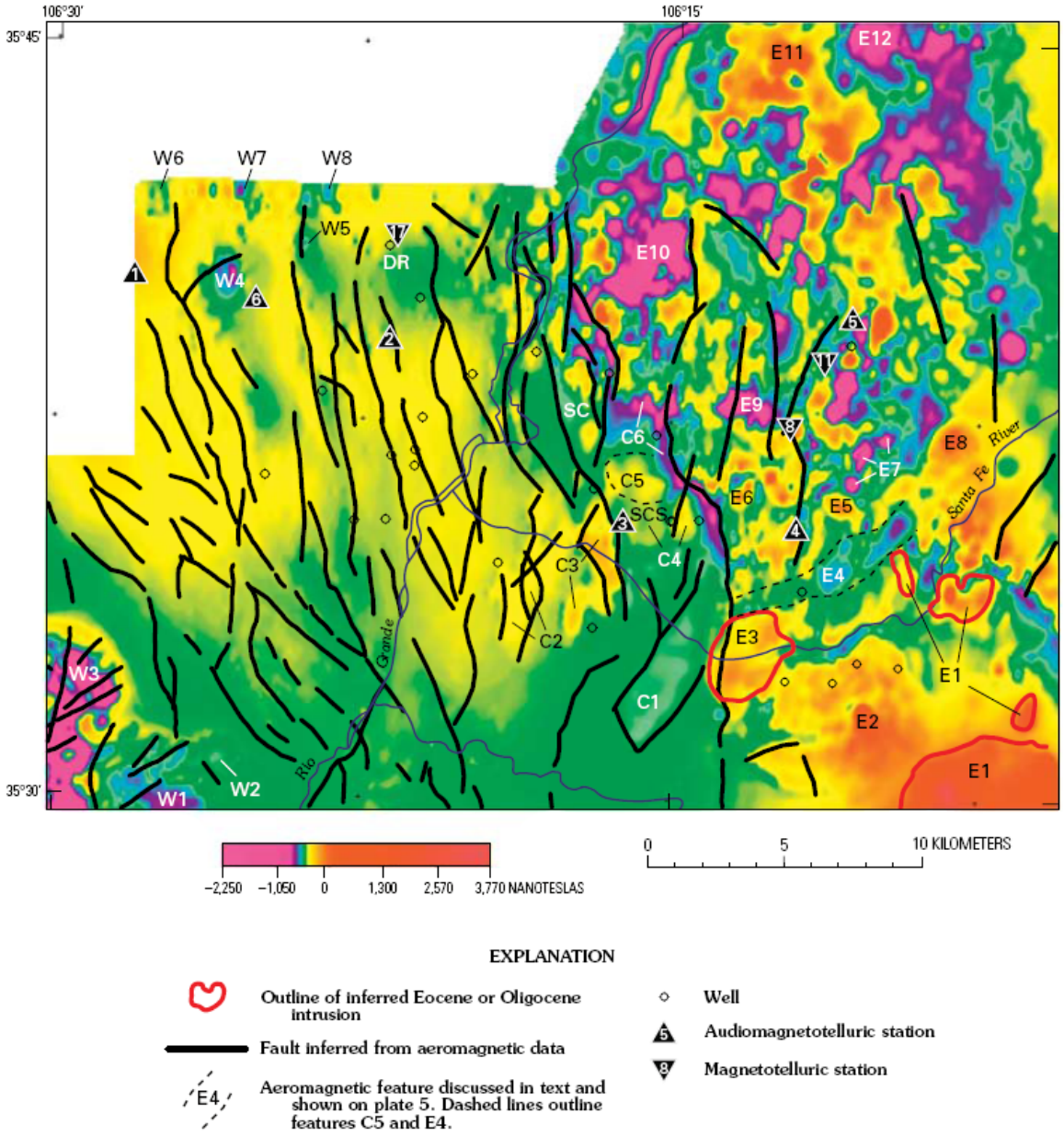

Figure 7. Aeromagnetic data of the northern part of the Santo Domingo Basin with interpreted faults. MT and AMT stations where used to ground truth aeromagnetic data (from Minor, S.A., ed., 2006, The Cerrillos uplift, the La Bajada constriction, and hydrogeologic framework of the Santo Domingo Basin, Rio Grande rift, New Mexico: U.S. Geological Survey Professional Paper 1720, 189).

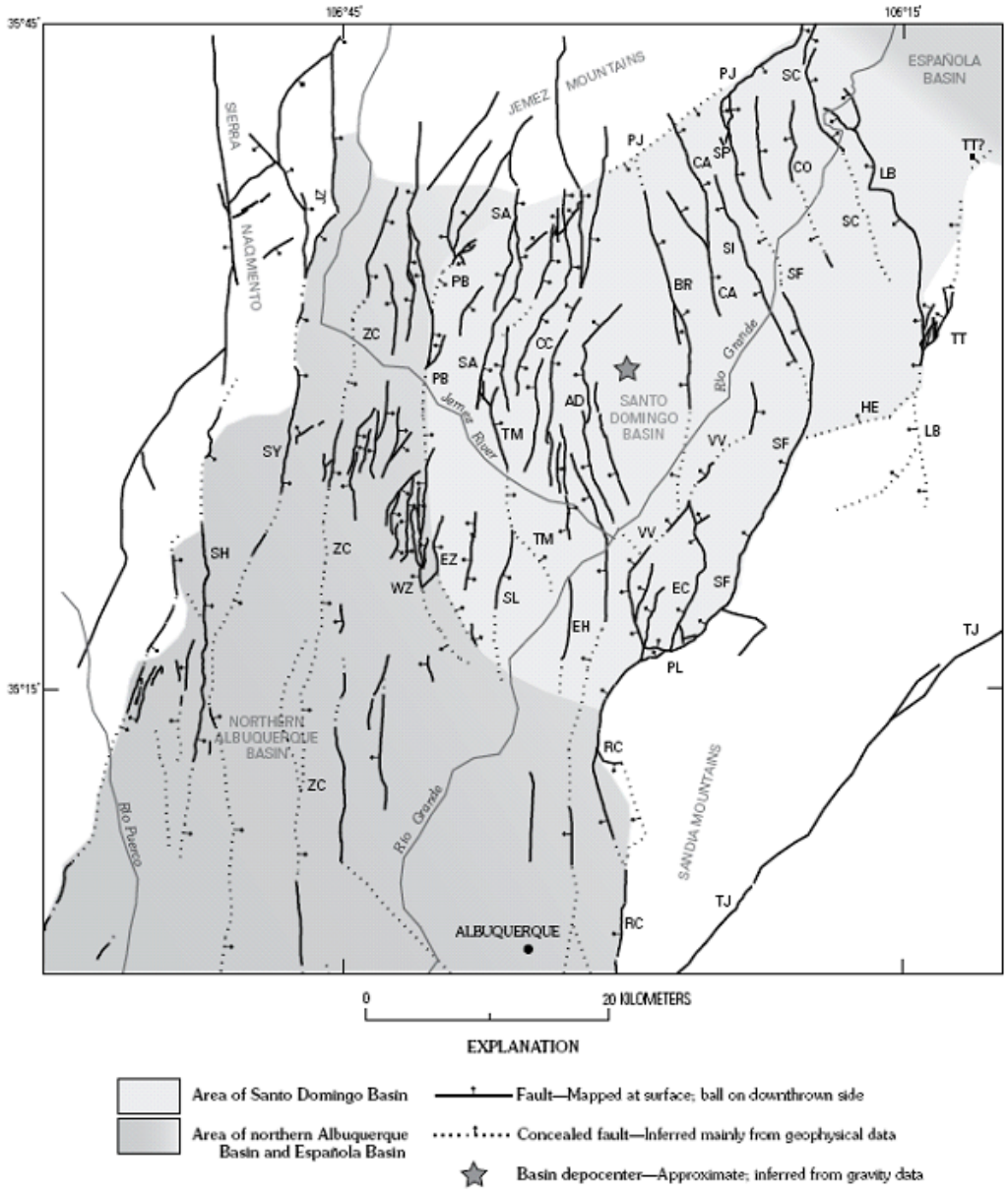

Figure 8. Major intrabasin and basin-bounding faults of the Santo Doningo Basin. Fault abbreviations are: AD, Algodones; BR, Borrego; CA, Camada; CC, Cañada de Cochiti; CO, Cochiti; EC, Escala; EH, East Heights; EZ, East Ziana; HE, Hagan Embayment; JZ, Jemez; LB, La Bajada; PB, Pico Butte; PJ, Pajarito; PL, Placitas; RC, Rincon; SA, Santa Ana; SC, Sanchez; SH, Sand Hill; SI, Sile; SF, San Francisco; SL, South Luce; SP, South Pajarito; SY, San Ysidro; TJ, Tijeras; TM, Tamaya; TT, Tetilla; VV, Valley View; WZ, West Ziana; ZC, Zia County Dump (from Minor, S.A., ed., 2006, The Cerrillos uplift, the La Bajada constriction, and hydrogeologic framework of the Santo Domingo Basin, Rio Grande rift, New Mexico: U.S. Geological Survey Professional Paper 1720, 189.).

These above mentioned observations lead to the idea that active faulting migrated basinward resulting in a narrowing of the active rifting zone. The intra-basin faults may also have been active the longest and thus have more pronounced growth-fault geometries (Minor, 2006). As a result of this fault pattern analysis, a two-stage tectonic history for the fault development was put forth (Minor, 2006). In the early stage of structural development of the basin, oblique-normal rifting along northeast-striking faults, possibly related to northeast-striking Proterozoic shear zones, was dominant (Minor, 2006). In the later stage, a network of intra-basin, semicircular faults developed to accommodate intra-rift, roughly east-west, extension concentrated around the basin depocenter (Minor, 2006). This argument is in agreement with the two-stage history of the Rio Grande rift as a whole.

SANTO DOMINGO BASIN FILL

From youngest to oldest, the fill of the Santo Domingo Basin is predominantly of three lithologic units, the Santa Fe Group, the Espinaso Formation, and the Galisteo Formation. The Santa Fe Group is comprised of mainly the Tesuque Formation, with small portions of the Sierra Ladrones Formation and Cochiti Formation included as well. The Tesuque Formation is composed of eastern pediment deposits derived from the Precambrian granitic basement rocks of the Sangre de Cristo Mountains that intertongue with coarser axial-river gravel and sand derived from granite and distinctive quartzite sources (Minor, 2006). The Tesuque Formation was described by Grant (1999) as being primarily a pinkish-tan, soft, arkosic, silty sandstone with minor conglomerate and siltstone members. The Sierra Ladrones Formation is similar to the Tesuque Formation but, instead, the pediment is derived from the Sandia Mountains. The Cochiti Formation

is derived from western pediment deposits, which contain more gravel and coarser sand than the eastern pediment sediments, and are dominated by compositionally diverse volcanic clasts derived from the Jemez volcanic field (Minor, 2006). Estimated thicknesses for the Santa Fe Group in the Santo Domingo Basin vary considerably from between 300 to 1500 m (Quesada, 2004).

The Espinaso Formation underlies the Santa Fe Group within the basin and is comprised of volcaniclastic sediments eroded from the nearby Ortiz Mountains and Cerrillos Hills (Figures 4 and 5). The sediments are composed of braided stream deposits, water-laid immature classic sandstones, conglomerates, and boulder conglomerates (Grant, 1999). These sediments are then interbedded with matrix-supported pebble to boulder debris-flow deposits and air-fall/ash-flow deposits (Grant, 1999). In the canyon outcrops on the edges of the basin the Espinaso Formation has been estimated to be 400 m thick (Stearns, 1953a,b).

Located beneath the Espinaso Formation in section is the Galisteo Formation. It is thought to be derived as an erosional byproduct of the initial rise of the Sangre de Cristo and Nacimiento mountains (Grant, 1999). The formation consists of two-thirds calcite-cemented argillaceous red and white sandstones and conglomerates, with the other one-third being red clays, shales, and water laid tuffs (Stearns, 1943, 1953a,b, and Grant, 1999). The Galisteo Formation is also present within the canyon on the edges of the basin where Stearns (1943) estimates its thickness at 400 m. The Galisteo Formation sits unconformably on top of the Late Cretaceous Mancos Shale Formation (Stearns, 1943).

The Miocene to Pleistocene Santa Fe Group in the Santo Domingo Basin is related to the more recent stage of rift development, while the late Eocene Espinaso

Formation and early Eocene Galisteo Formation date back to the earlier rift stage. The Santa Fe Group is a focus topic of Minor (2006) where they have presented a depositional history. The location of the axial sand and gravel exposures can be seen in Figure 9. In the northern part of the basin, the Santa Fe Group is interlayered with and is overlain by volcanic rocks of the Cerros del Rio volcanic field and early Pleistocene Bandelier Tuff erupted from the nearby Valles Caldera.

Three different facies are presented based on whether the sediments are derived from the western piedmont, axial sand and river gravel, or the eastern piedmont. In Figure 10 is a plot displaying the distribution of these facies over time. From the distribution and continuity of these facies a depositional history for the Santa Fe Group was deduced. The late Miocene through late Pilocene axial sand and gravel facies indicate mainly an aggradation event (Minor, 2006). Between 2.7 and 1.1 Ma, volcanic activity increased, resulting in large-scale lava flows and ash-fall tuffs where the ancestral Rio Grande was dammed and rerouted. From post-Bandelier Tuff time onward the basin went through several episodes of aggradation and incision forming many different terraces. This recent history is thought to be related to climate cycles (Minor, 2006).

SUMMARY

The Santo Domingo Basin is a structurally complex basin located between two dip-opposing basins within the Rio Grande rift. But, a clearer picture has emerged of the geologic history of the Santo Domingo Basin through a better understanding of subsurface geology aided by structural mapping, gravity, and aeromagnetic data. This has been put into the context of a two-stage tectonic history of the Rio Grande rift. In the

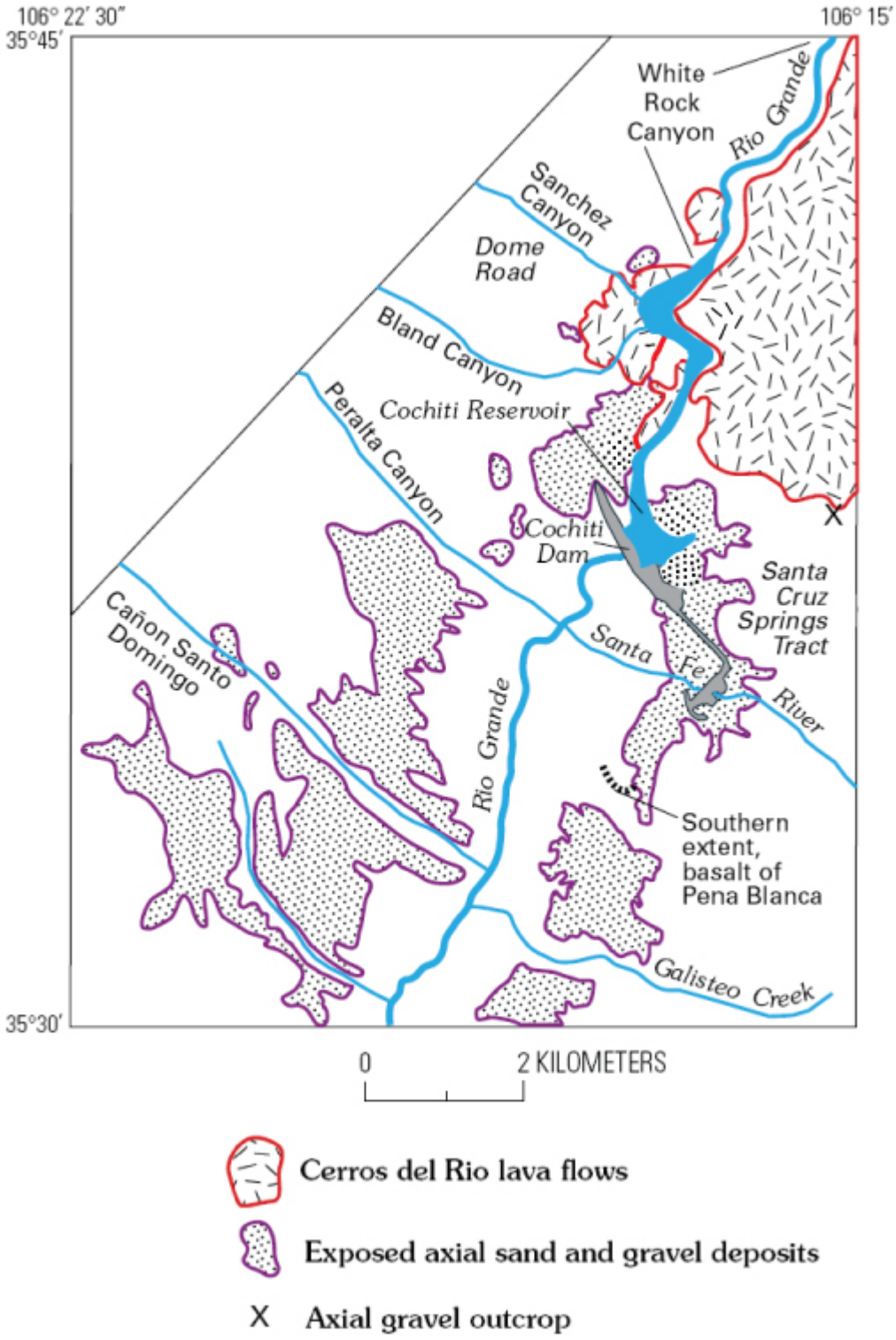

Figure 9. Distribution of exposed axial river gravel deposits and Cerros del Rio lava flows. The deposits of importance to the present work include the deposits along the Santa Fe River (modified from Minor, 2006).

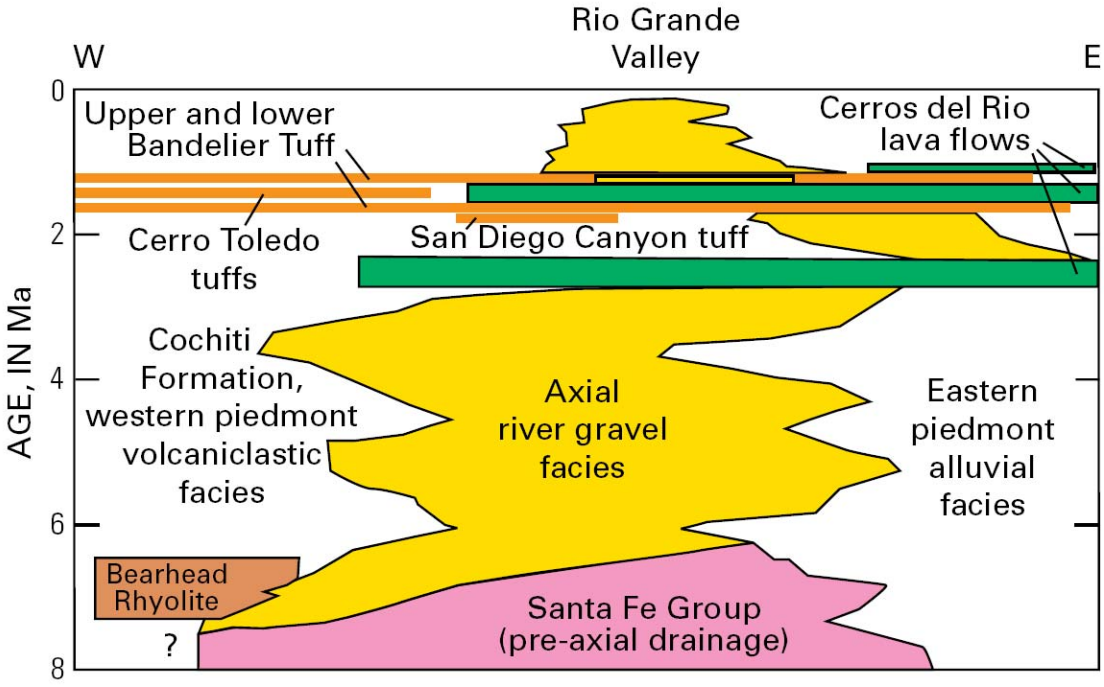

Figure 10. Time-position distribution of basin-fill deposits. Width of figure represents approximately 20 km (from Minor, S.A., ed., 2006, The Cerrillos uplift, the La Bajada constriction, and hydrogeologic framework of the Santo Domingo Basin, Rio Grande rift, New Mexico: U.S. Geological Survey Professional Paper 1720, 189.).

earlier stage, rifting occurred along a northeastern trend, which is related to the northeastern elongation of the Santo Domingo Basin. During a lull in tectonic activity, basin sedimentation was mainly an aggradation event of the ancestral Rio Grande and the sediments were mainly composed of the Santa Fe Group. As a result of the second tectonic stage of rift development, a renewal of volcanic activity dammed the ancestral Rio Grande drainage and forced a resettlement of the river. The renewed tectonic activity was then in a more east-west direction and the uplift had a complicating effect on the structure of the intra-basin faults in the Santo Domingo Basin. With the return to a lull state in tectonic activity, the Rio Grande incised into the volcanic tuff layers and returned

to a more central location in the basin. Through possible climate change influences in the recent geologic past, the basin has experienced a series of aggradation and canyon incising events. This history results in the present Santo Domingo Basin being cut by a complicated series of faults and comprised of many different terraces composed of the Santa Fe Group.

CHAPTER 3

METHODOLOGY

LOCATION

Since 2000 considerable geophysical data have been collected in the Santo Domingo Basin during the SAGE program. The land status in the Santo Domingo Basin is a complex mosaic of federal (National Forest, National Park, and Bureau of Land Management), State of New Mexico, Native American, and private control (Figure 11). The focus of the present work is the data collected in and around the Santa Fe River and La Bajada Fault escarpment on the Cochiti Pueblo. Specifically, the data are MT and TEM soundings from 2000-2003, 2005, and 2007 (Figures 12 and 13). The gravity data are a composite data set including data from all of the SAGE years as well as several other outside sources (Figure 14). Since this is a sequel to Quesada (2004), who analyzed the 2000-2003 data, the emphasis will be on the newer 2005 and 2007 data. Field work and data processing discussed here will be of the newer data. Parties interested in the earlier field work and data processing are referred to Quesada (2004). When it comes to the pre-inversion work, MT impedance tensor rotation, data editing, and the smooth two-dimensional (2-D) inversions of the data, all of the data will be discussed.

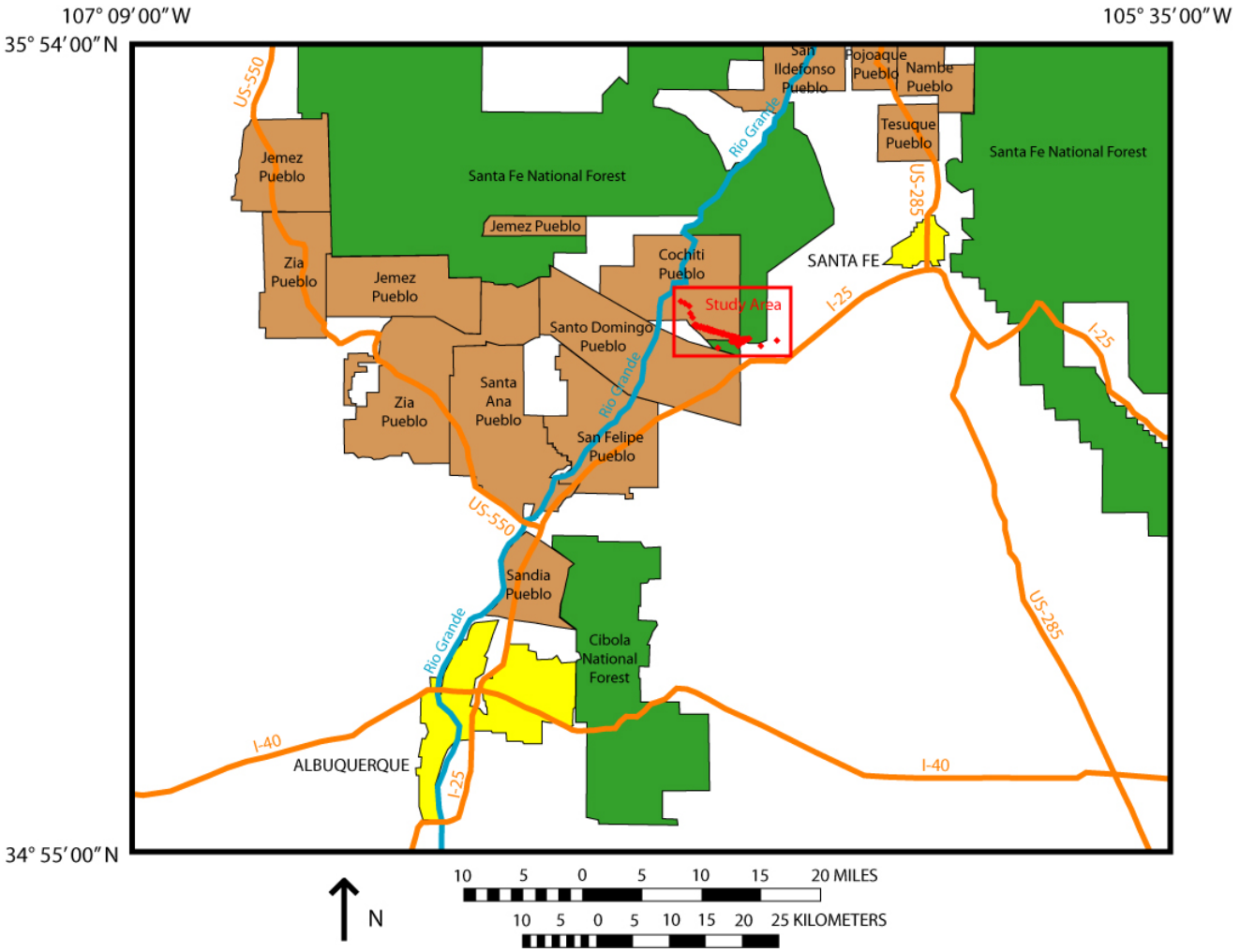

Figure 11. The mosaic of land status in the SAGE MT study area. The general location of the study area is enclosed by the red box. Red diamonds indicate MT sounding locations. The mosaic of land status is illustrated in brown for Native American lands, green for National Forests, and yellow for cities. What is not shown is the further patchwork of BLM and state owned land.

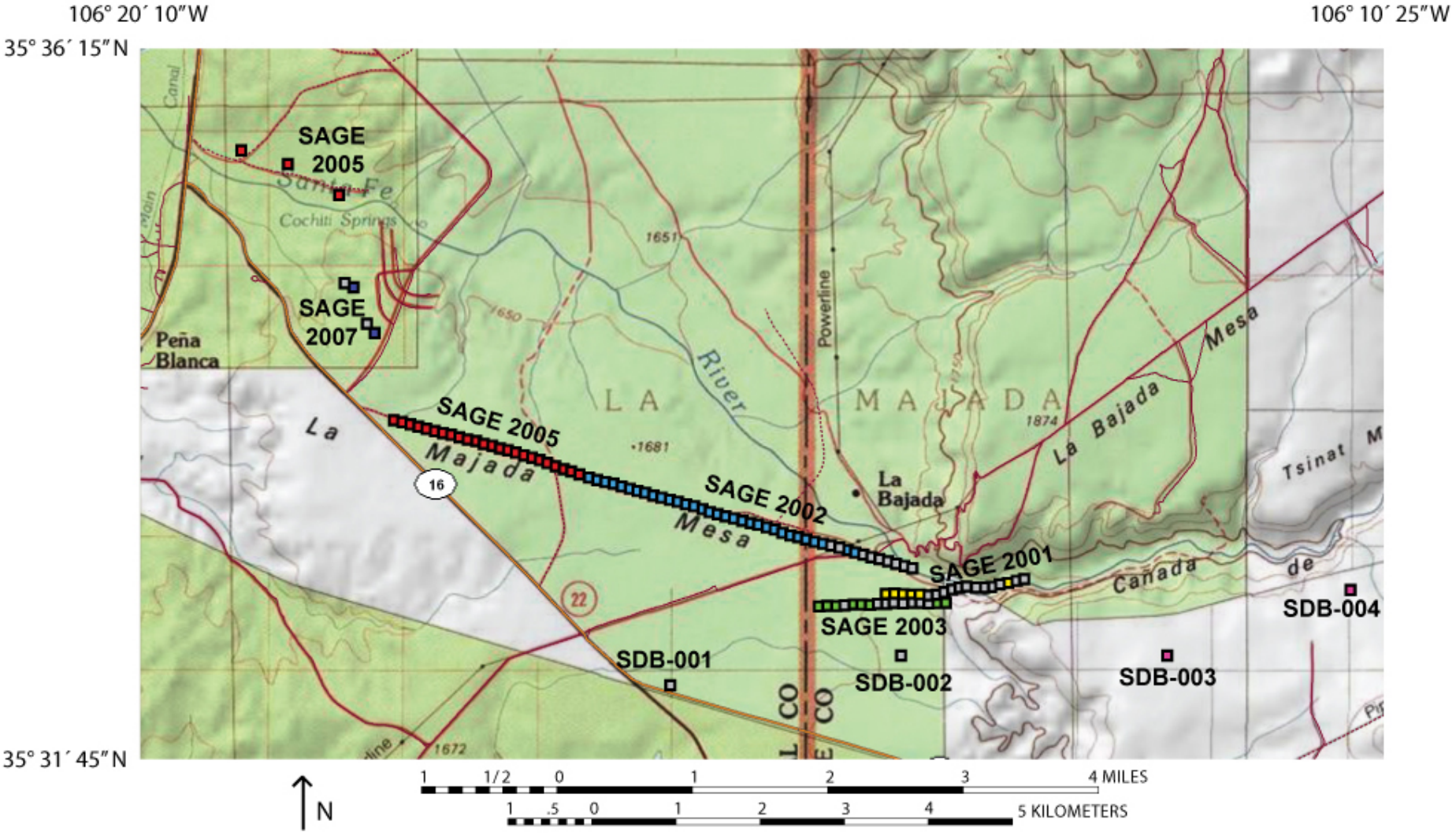

Figure 12. SAGE MT sounding locations. Colored squares indicate MT soundings utilized in the smooth 2-D inversion. Grey boxes indicate MT soundings not utilized in the smooth 2-D inversion.

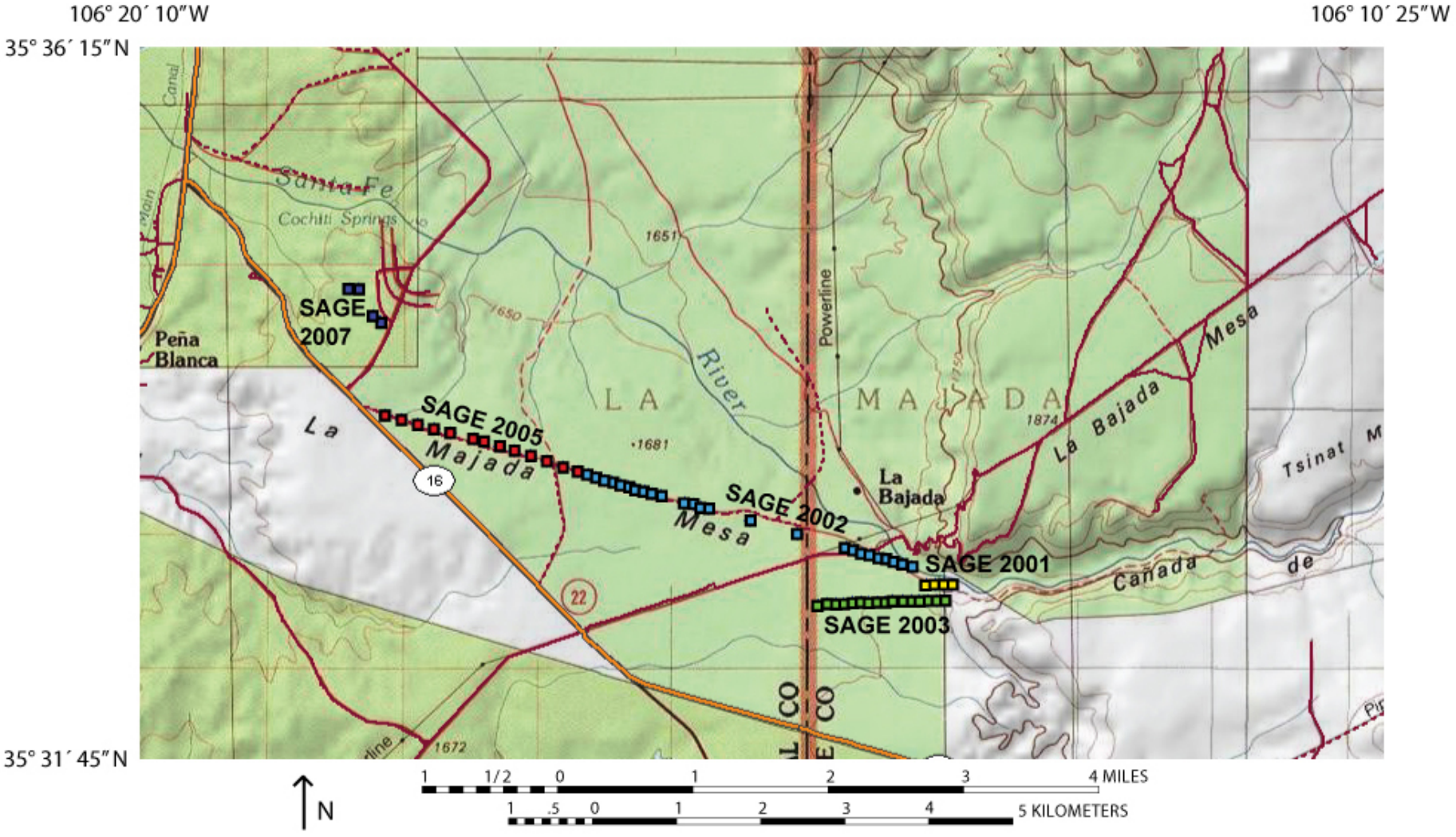

Figure 13. SAGE TEM sounding locations. Colored squares indicate the TEM soundings.

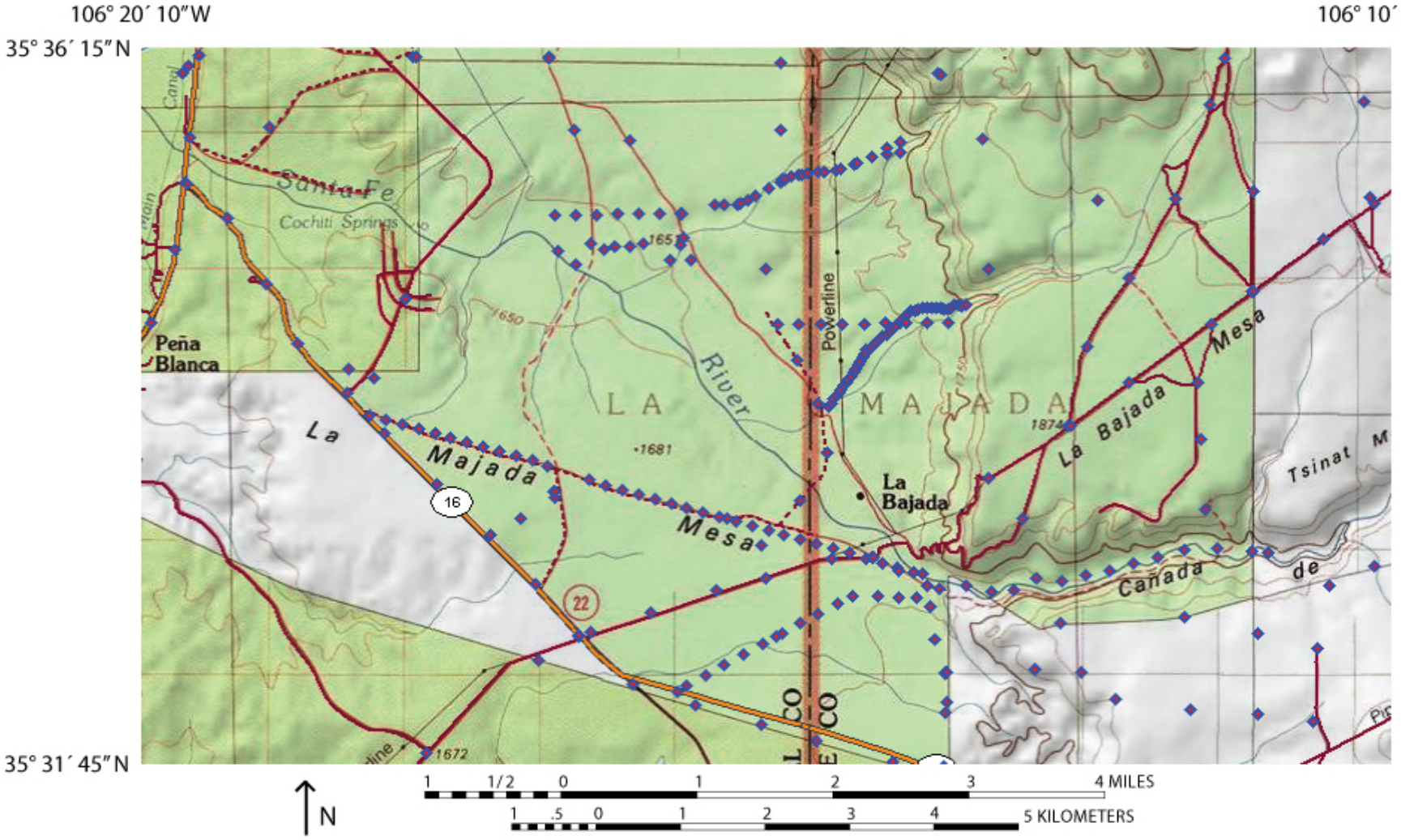

Figure 14. Gravity measurements in the SAGE MT study area. Blue and red diamonds indicate the locations of gravity measurements. The gravity data set is a composite from various SAGE years as well as outside sources (Biehler, personal communication, 2007).

FIELD WORK

MT measurements are recordings of the naturally occurring time-varying electric and magnetic fields at the Earth's surface. For a further discussion on MT theory and sources see Appendix A. During SAGE 2005, Quantec Geoscience donated half of a Titan 24 MT system that included enough equipment to collect 12 MT soundings simultaneously. The full Titan 24 system is a distributed array MT system consisting of 24 electric dipoles laid out end to end along the profile direction at a fixed station spacing, 12 electric dipoles laid out in the orthogonal direction at an interval equal to double the station spacing, and two horizontal magnetic induction coils, setup parallel and perpendicular to the profile direction (Figure 15). In the Titan system each MT station recording consists of the potential difference measurements across the electric dipoles, inline and orthogonal, and current measurements from the single set of magnetic induction coils. The system setup is greatly simplified by measuring the magnetic field at only one location. For a 2-D resistivity distribution, $\rho(x, z)$, and for an ideal Titan 24 MT system setup where the profile line is setup perpendicular to the geoelectric strike direction, the single set of magnetic field sensors yields a valid MT system response because the magnetic field parallel to geoelectric strike would not vary over the length of the profile (Appendix B).

To minimize the impact on the Cochiti Pueblo land, the Quantec Titan 24 system was set up along a preexisting dirt road used in the late 1970's for a petroleum exploration seismic line. The 2005 survey extends the SAGE 2002 survey conducted along the same road also using the Quantec Titan 24 system. The 2005 data consists of 24 MT soundings that where collected using two separate equipment setups. During the first setup, MT sites SDB-013

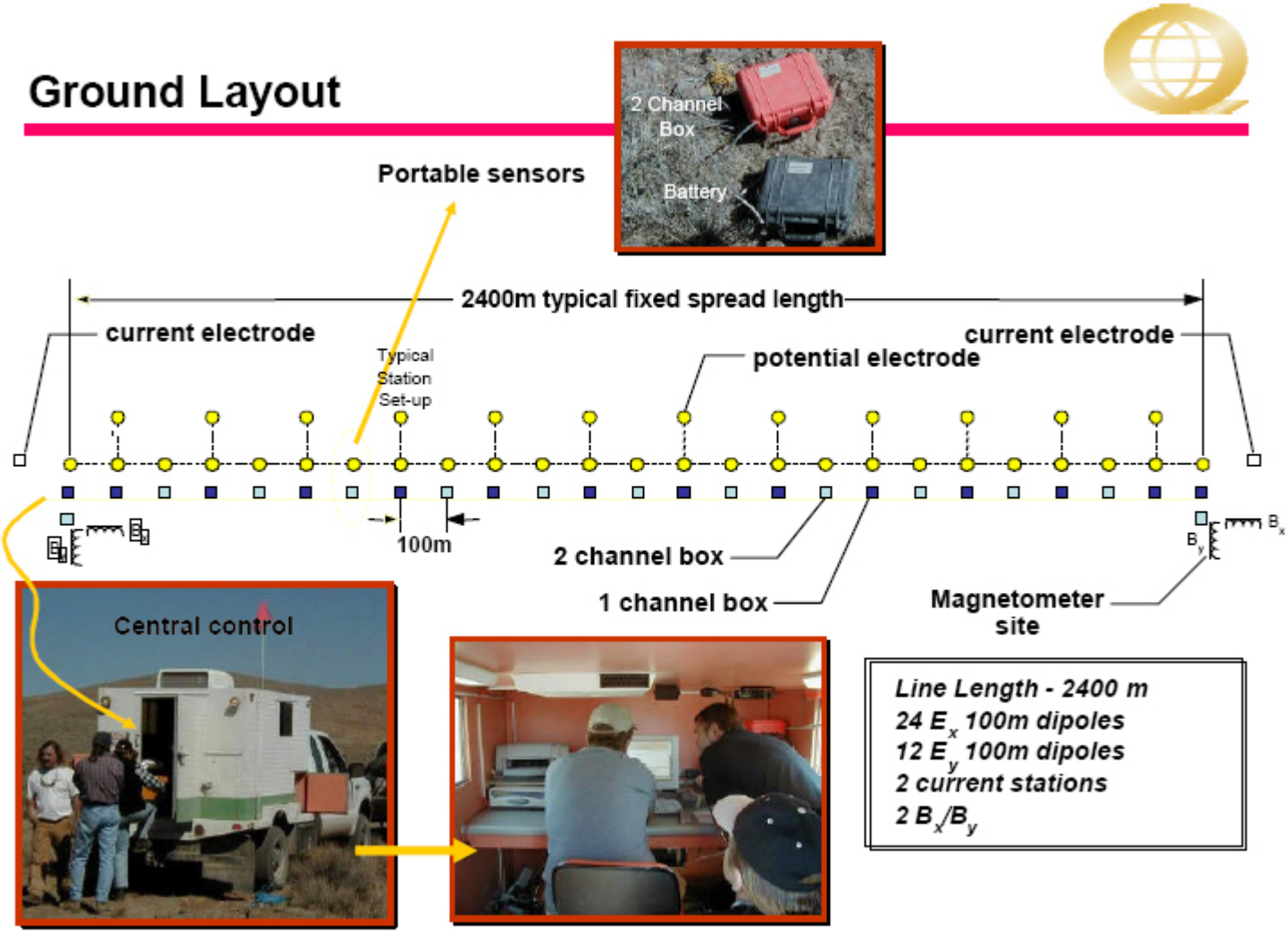

Figure 15. The ground layout for the Quantec Titan 24 system (courtesy of Quantec Geoscience).

through SDB-024 were occupied with the magnetic field sensors located near SDB-024. During the second set up, MT sites SDB-001 through SDB-012 were occupied with the magnetic field sensors located near SDB-001. A power line ran though the survey between MT sites SDB-008 and SDB-010. A magnetic remote reference site was used for both setups and consisted of a second set of horizontal magnetic field sensors. The data collection from the survey line and the remote reference were coordinated by the Quantec-provided MT operators. MT recording start times, the sample rates, and record lengths were communicated over handheld radios and synchronized using a set of internal GPS clocks.

Also during SAGE 2005, Quantec Geoscience donated two complete single site full tensor MT data logger systems, the Quantec Spartan System, which were setup on the Santa Fe River floodplain near the Cochiti Dam spillway (Figure 12). Each Spartan MT system consist of two perpendicular electric dipoles set up in a "L" shaped configuration and three induction coils: two magnetic induction coils setup in orthogonal, horizontal directions and an additional magnetic induction coil setup in the vertical direction allowing for full tensor recording of the magnetic field (Figure 16). The two systems operated so that each could be used as a remote reference for the other. Three over night soundings were recorded with the Spartan systems over a period of two nights.

SAGE 2007 data included four audio magnetotelluric (AMT) soundings in the Cochiti Dam spillway recorded with a Geometrics Stratagem system. The system setup consisted of two orthogonal, electric dipoles and two horizontal, magnetic induction coils. The system also included a transmitter antenna setup at least three skin depths (Appendix A) distance away from the recording site. The transmitter was used to fill-in AMT frequencies with low natural signal strength. The equipment records high frequency MT data from 10 to

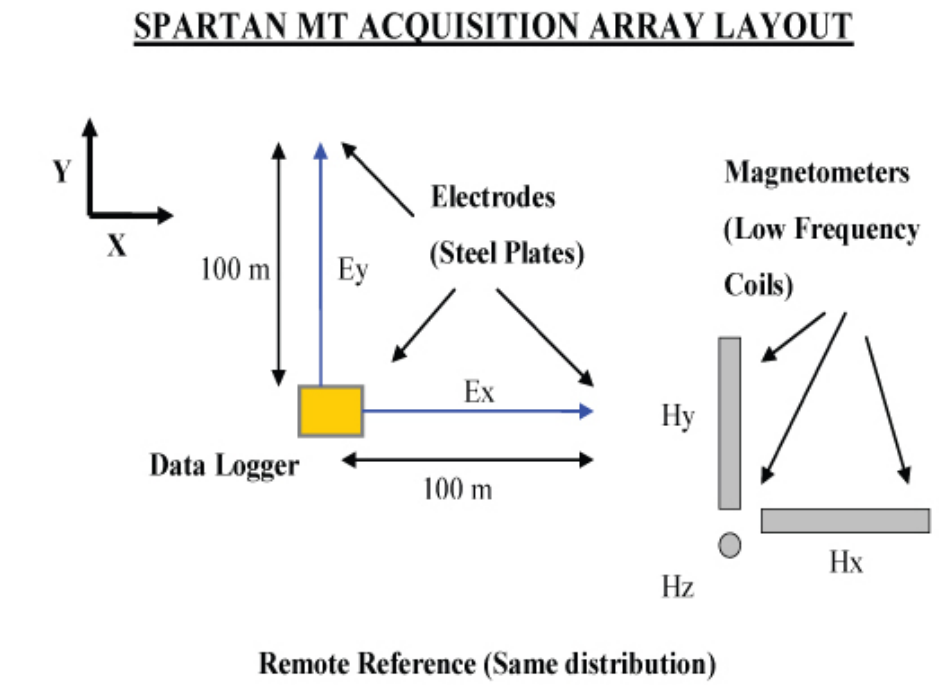

Figure 16. The ground layout for the Quantec Spartan MT system (courtesy of Quantec Geoscience).

100,000 Hz and thus is restricted to much shallower depths of investigation compared to the Quantec Titan and Spartan systems. There is no remote reference capability with the Stratagem system so it was employed as a stand alone instrument.

Gross errors in the MT station locations will affect the data analysis. So coordinates for each MT site were verified on a map and the elevations were corrected to a digital elevation model, DEM, implemented in National Geographic State Series: New Mexico software. This was required because of inaccuracies in the elevations for some of the older MT sounding locations. The locations from the 2002 and 2005 Titan surveys were within a meter of the standard because differential GPS was used. However MT sounding locations from other SAGE years used less accurate hand held GPS units and in some cases the elevations were extrapolated from topographic maps. Even so, all elevations are estimated to be within 10 m accuracy.

In the TEM method the primary electromagnetic fields are induced into the Earth by transient pulses of electrical current in a single wire transmitter loop. The resulting secondary magnetic fields due to the induced eddy currents in the ground are commonly recorded by a loop-centered, vertical magnetic induction coil when the transmitter current is turned off. Zonge Engineering and Research Organization provided expertise in the use of their TEM system during the 2001-2007 SAGE programs. In 2005, 13 in-loop TEM soundings with a station spacing of 200 m were recorded along the MT profile utilizing a single-wire 100 x 100 m square transmitter loop. In 2007, 4 in-loop TEM soundings were recorded at the AMT sites. The TEM soundings were recorded primarily as a way to check for and correct for static shifts (amplitude shifts in the MT data due to charge build ups and/or topographical features) that may or may not be present in the 2005 MT and 2007 AMT data (Pellerin and Hohmann, 1990).

In the gravity method, measurements of the Earth's acceleration of gravity are recorded at the surface. The gravity data were collected with LaCoste-Romberg and Scintrex

self-leveling gravity meters. Differential GPS was utilized to provide precise gravity station elevations. Gravity measurements were collected to improve/detect lateral density variations, their value for this study was to determine the basement structure, including geologic strike direction to be used as a proxy for the geoelectric strike direction. In Figure 14 only the stations within the general MT survey area are displayed. The gravity data set extends far beyond the MT study area and includes over 11,000 measurements collected over 26 years of SAGE and from other outside sources.

APPARENT RESISTIVITY AND IMPEDANCE PHASE CURVE EDITING

MT data processing has a specific meaning since the recorded electric and magnetic field time series data, **e**(t) and **h**(t) respectively, must be processed into frequency domain impedances, **Z**(ω), ω is angular frequency (Appendix B). MT data processing is usually accomplished using proprietary software from the company that makes the MT instrument. It can be an automated process as it is with the Geometrics Stratagem inside the equipment while in the field as the data are collected. Or, it can be a more user intensive activity requiring an industry provided processor dedicated to the processing the MT data as it is with the Quantec Titan and Spartan systems. The final result of the MT processing step is the output of a SEG (Society of Exploration Geophysicists) standardized data file called an ".edi file" which contains complex values for the impedance elements.

After the MT data were processed into impedances, the ".edi files" were imported into Geosystem's WinGLink software. In the software the complex values for the impedances, **Z**, were converted into apparent resistivity, $\rho_a(\omega)$, and impedance phase, $\varphi(\omega)$, values

$$\rho_{a(xy)}(\omega) = \frac{1}{\mu_0 \omega}\left|Z_{xy}(\omega)\right|^2, \quad (1)$$

$$\rho_{a(yx)}(\omega) = \frac{1}{\mu_0 \omega}\left|Z_{yx}(\omega)\right|^2, \quad (2)$$

$$\varphi(\omega)_{xy} = \tan^{-1}\left(\frac{\mathrm{Im}\{Z_{xy}(\omega)\}}{\mathrm{Re}\{Z_{xy}(\omega)\}}\right), \quad (3)$$

and

$$\varphi(\omega)_{yx} = \tan^{-1}\left(\frac{\mathrm{Im}\{Z_{yx}(\omega)\}}{\mathrm{Re}\{Z_{yx}(\omega)\}}\right), \quad (4)$$

where μ_0 is the magnetic permeability of free space. The subscript terms indicate the orientation of the electric field measurement, first term, and the magnetic field measurement, second term. Apparent resistivity is the average resistivity of an equivalent homogeneous half-space. When the impedance phase is 45° and for a homogeneous half-space the apparent resistivity is equal to the true resistivity. The apparent resistivity and impedance phase data were then displayed on log-log plots versus period (Figure 17) where period, T, is defined as $T = 2\pi/\omega$.

The resulting data points were then edited (deleted) to remove obvious outliers or if they caused the fitting curve to have a slope greater than $\pm$45 degrees on the log-log plot. Such removal of data points is somewhat subjective. However, it does recognize that sounding curves from a diffusion process such as MT must be smooth and that log ρ_a versus log T results rarely exceed slopes of 45 degrees (only in pronounced multi-dimensional cases). The WinGLink software allows for the superposition of a D+ smoothing curve fit to the data which aids in the identification of the obvious outliers. In a D+ smoothing, the

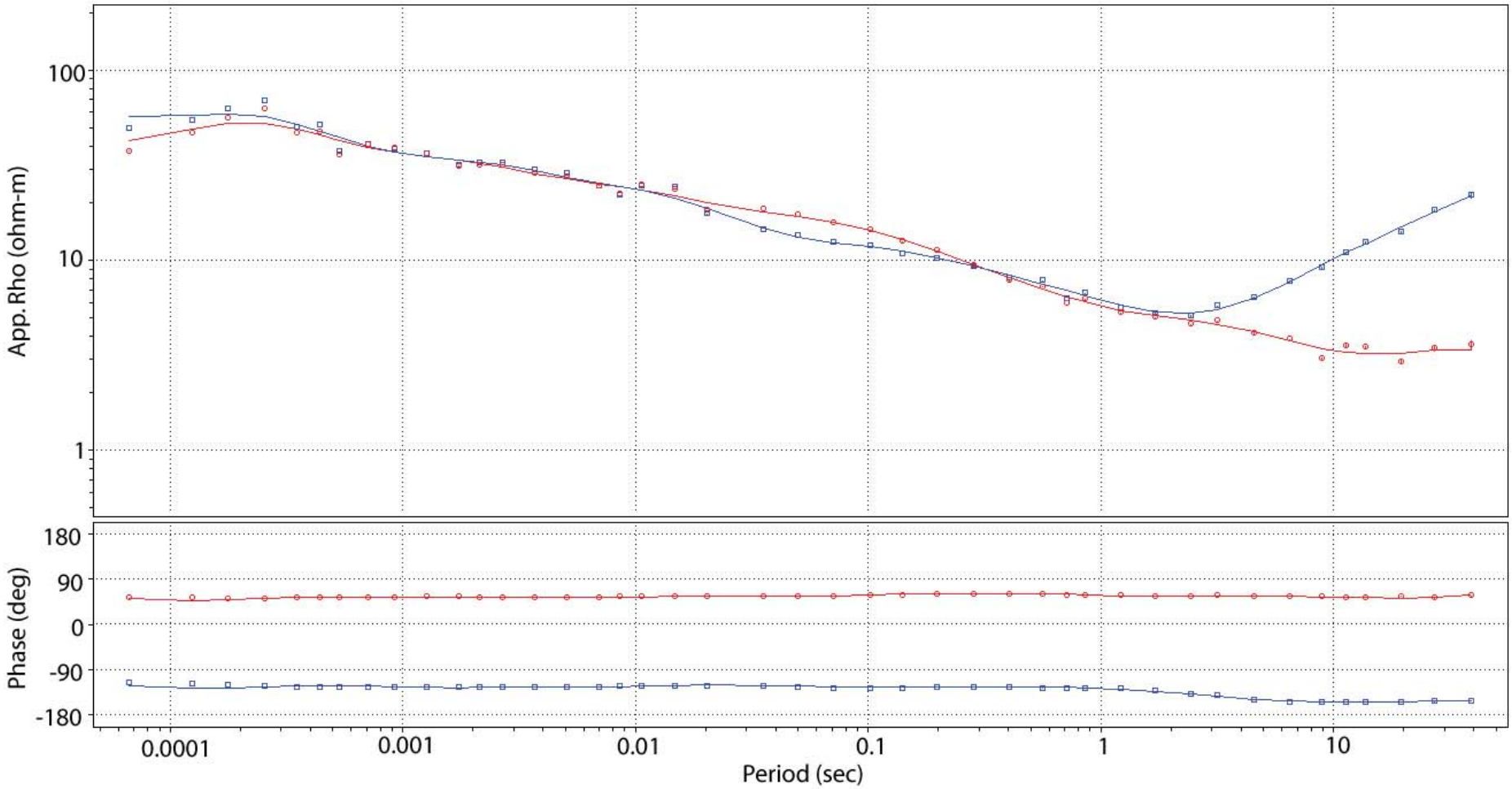

Figure 17. An example of apparent resistivity and impedance phase curves for MT station SDB-222.

results from a 1-D inversion of the MT data are used to construct a smooth version of the log-log apparent resistivities and phase. The D+ smoothing operation accomplishes this by extracting layer depths and conductances from 1-D inversions to produce a finite number of fictitious delta functions (layers of zero thickness but finite conductance) separated by perfect insulators (Parker, 1980; Beamish and Travassos, 1992).

DETERMINING THE GEOELECTRIC STRIKE DIRECTION

Since the study area is mostly contained within the conductive basin but does cross the La Bajada fault on the eastern end, a 2-D interpretation of the resistivity distribution is reasonable. This means that there should be a preferred, regional geoelectric strike direction that can be determined. The geoelectric strike direction may or may not be aligned with the geological strike direction of the La Bajada fault. One problem that immediately arises is that the survey was not setup perpendicular to geoelectric strike as determined by Quesada (2004). This is common in geophysics due to surveys with limited access or in order to minimize the impact on the land. Even if the Titan system was setup ideally perpendicular to geoelectric strike and if the resistivity distribution was perfectly 2-D, using a single pair of horizontal magnetic field measurements to process multiple MT soundings will not yield standard MT soundings (equations 1 and 2) because the cross-strike magnetic fields would vary over the length of the survey.

Realizing this major problem but still wishing to continue to 2-D model and interpret the data, a second problem arises. In actual MT data the geoelectric strike direction varies between sites and different periods because the geoelectric structure varies with depth as well as laterally. Therefore, the concept of a preferred constant geoelectric strike direction is a

compromise that is influenced greatly by the geologic problem under investigation. In the present problem, to determine the gross structural features present in the basin, the most significant geoelectric strike direction is associated with MT data collected at long periods when the MT results are sensing regional trends in the resistive basement. Therefore the emphasis for geoelectric strike determination will be on MT data in the period range from 9 s to 105 s. This should result in 2-D resistivity inversion results that are particularly sensitive to variations in the crystalline basement. Inversion results from the short period data are not thought to be overly affected by the choice of geoelectric strike. This is because the short period data are consistent with a 1-D resistivity distribution, $\rho(z)$, which is independent of any assumed geoelectric strike direction.

Two graphical methods used to determine the preferred geoelectric strike from the MT data were polar diagrams and phase tensor plots (see Appendixes C and D). Because the MT data were collected in a basin filled with electrically conductive sediments the long axis of both the polar diagrams and phase tensor plots will be aligned parallel with the geoelectric strike direction. From the data set there are seven, full tensor long period MT soundings, four on the eastern end (SDB-001, SDB-002, SDB-003, and SDB-004) and three on the western end (SDB-525, SDB-526, and SDB-527) of the survey profile. Figure 18 displays the polar diagrams for the MT soundings on the eastern end, while Figure 19 displays the polar diagrams for the MT soundings on western end. Figure 20 displays phase tensor plots for the eastern end, while Figure 21 displays phase tensor plots for the western end. The diagrams and plots in these figures display a wide range of orientations for the long axis. Of the MT soundings on the eastern side of the survey, SDB-001 and SDB-002 are the more important ones to consider because they lie within the basin on the La Majada Mesa, while

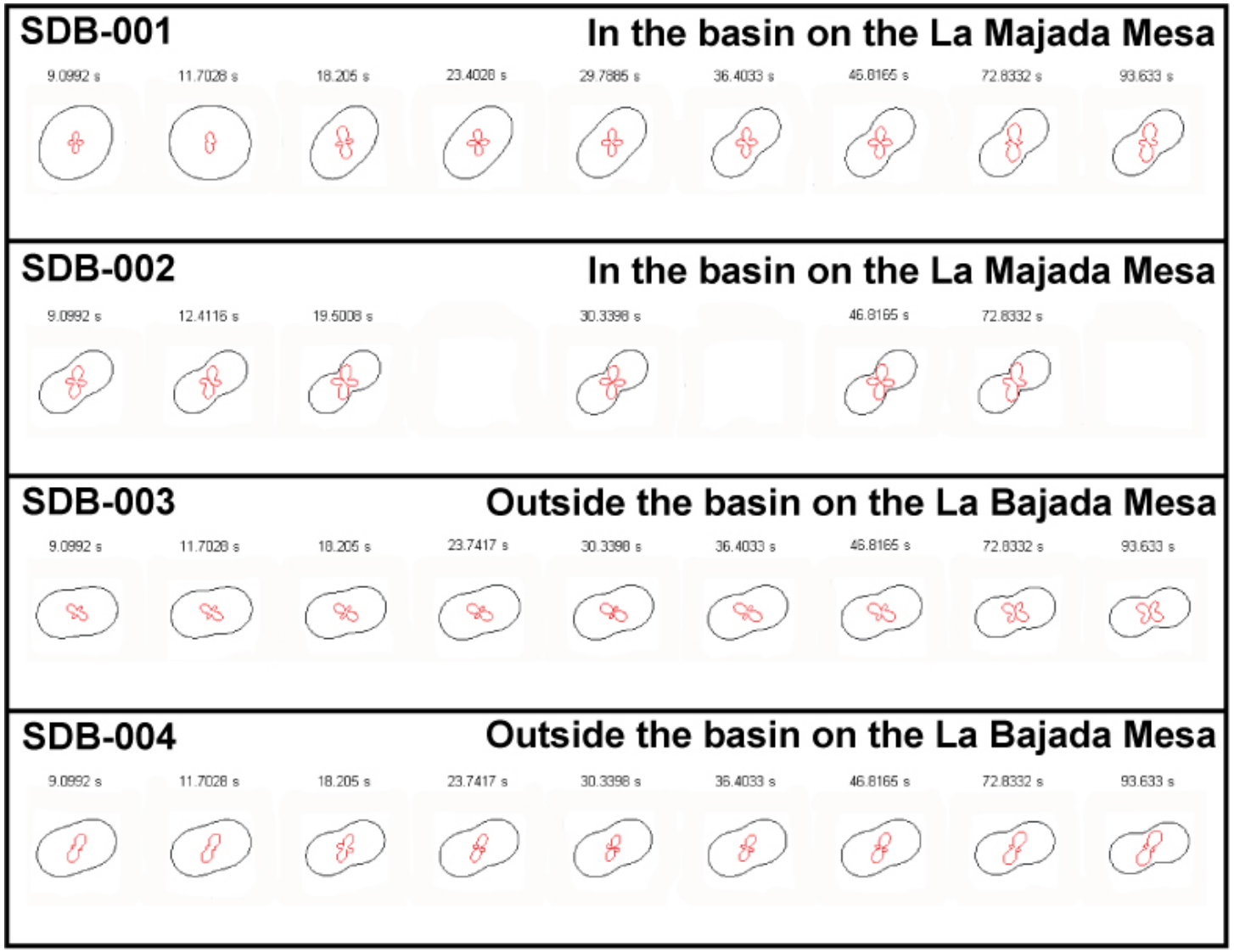

Figure 18. Long period polar diagrams from MT soundings on the eastern end of the profile. The numbers above each diagram indicate the period in seconds.

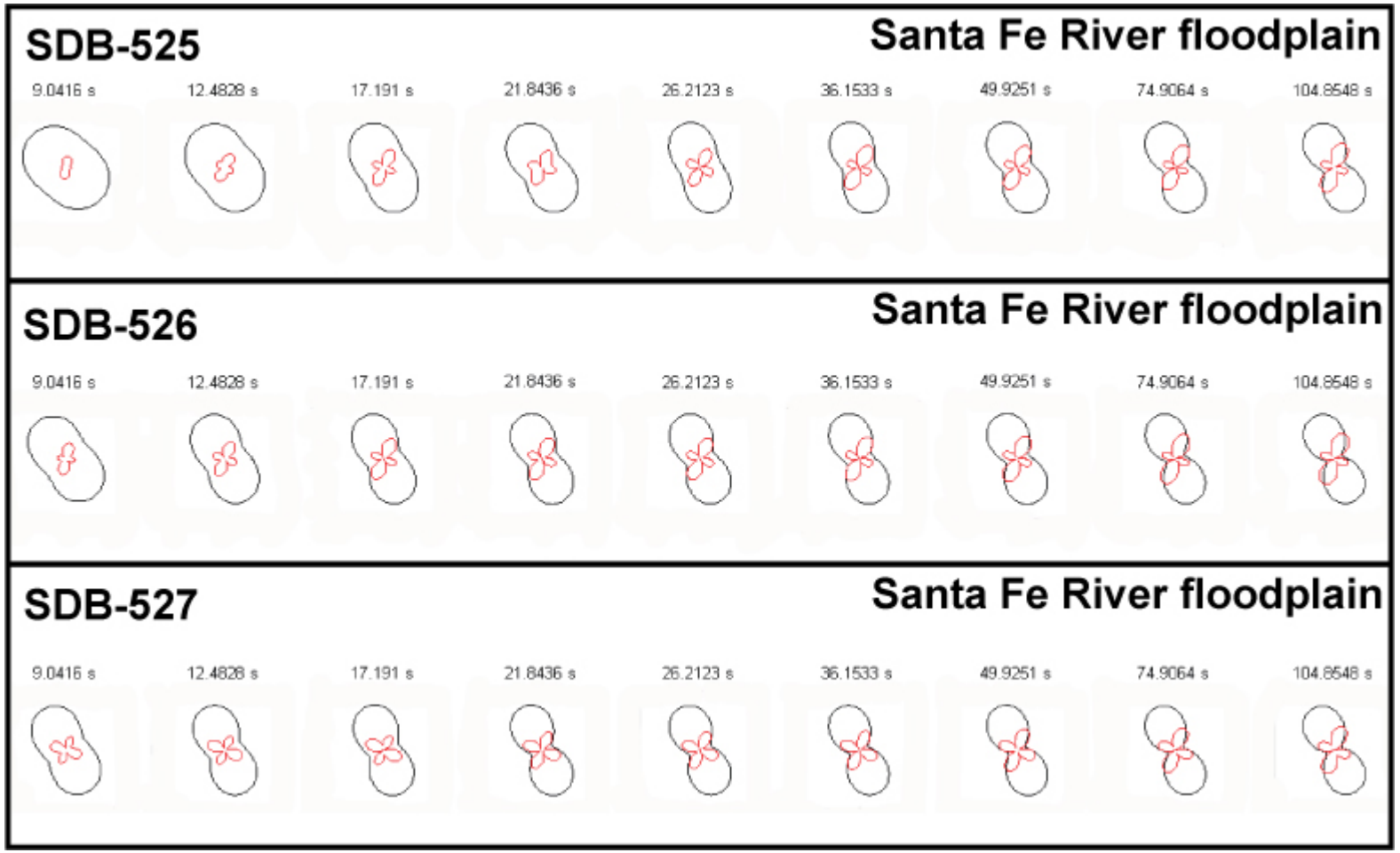

Figure 19. Long period polar diagrams from MT soundings on the western end of the profile. The numbers above each diagram indicate the period in seconds.

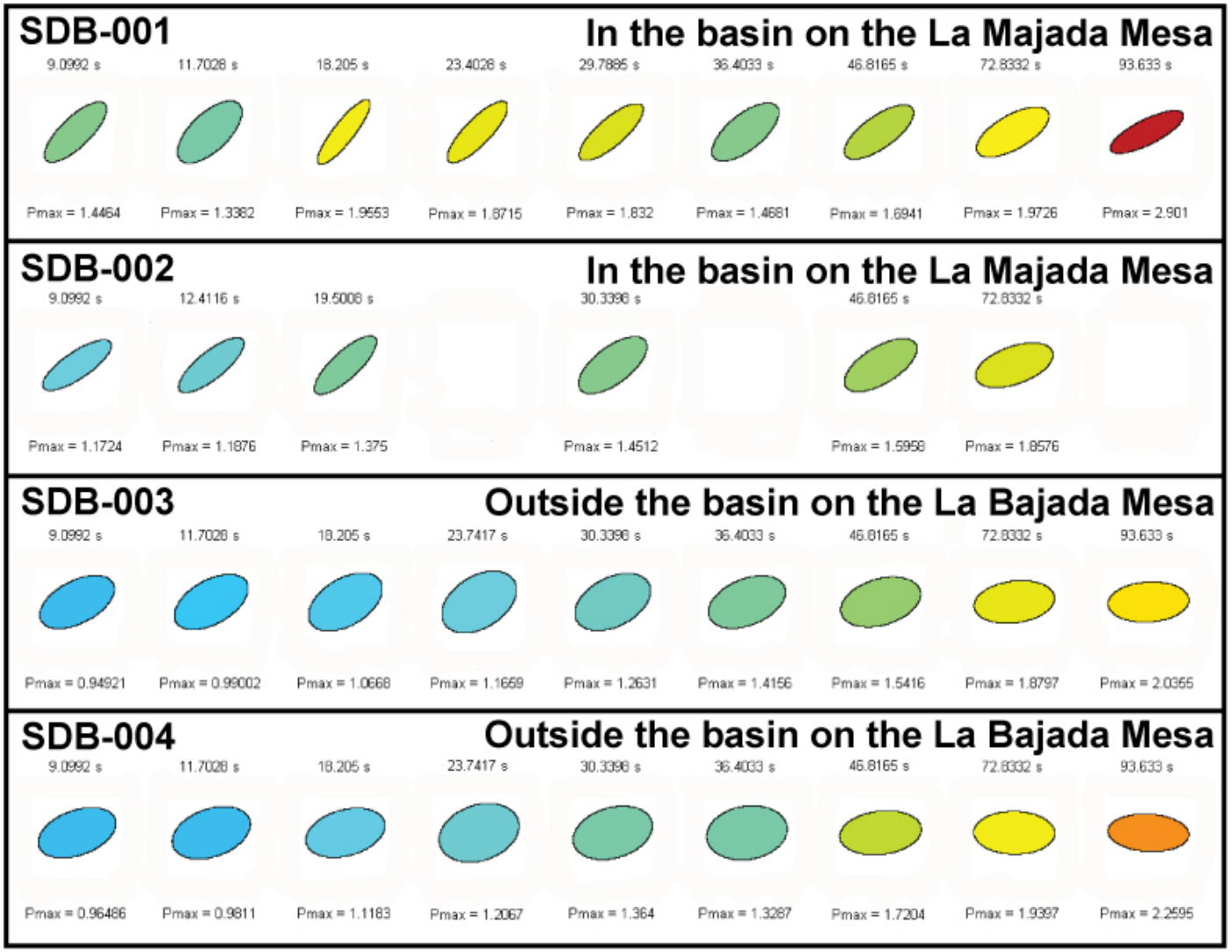

Figure 20. Long period phase tensor plots from MT soundings on the eastern end of the profile. The numbers above each plot indicate the period in seconds. The fill color and the Pmax value both indicate the maximum phase value used to normalize the plots.

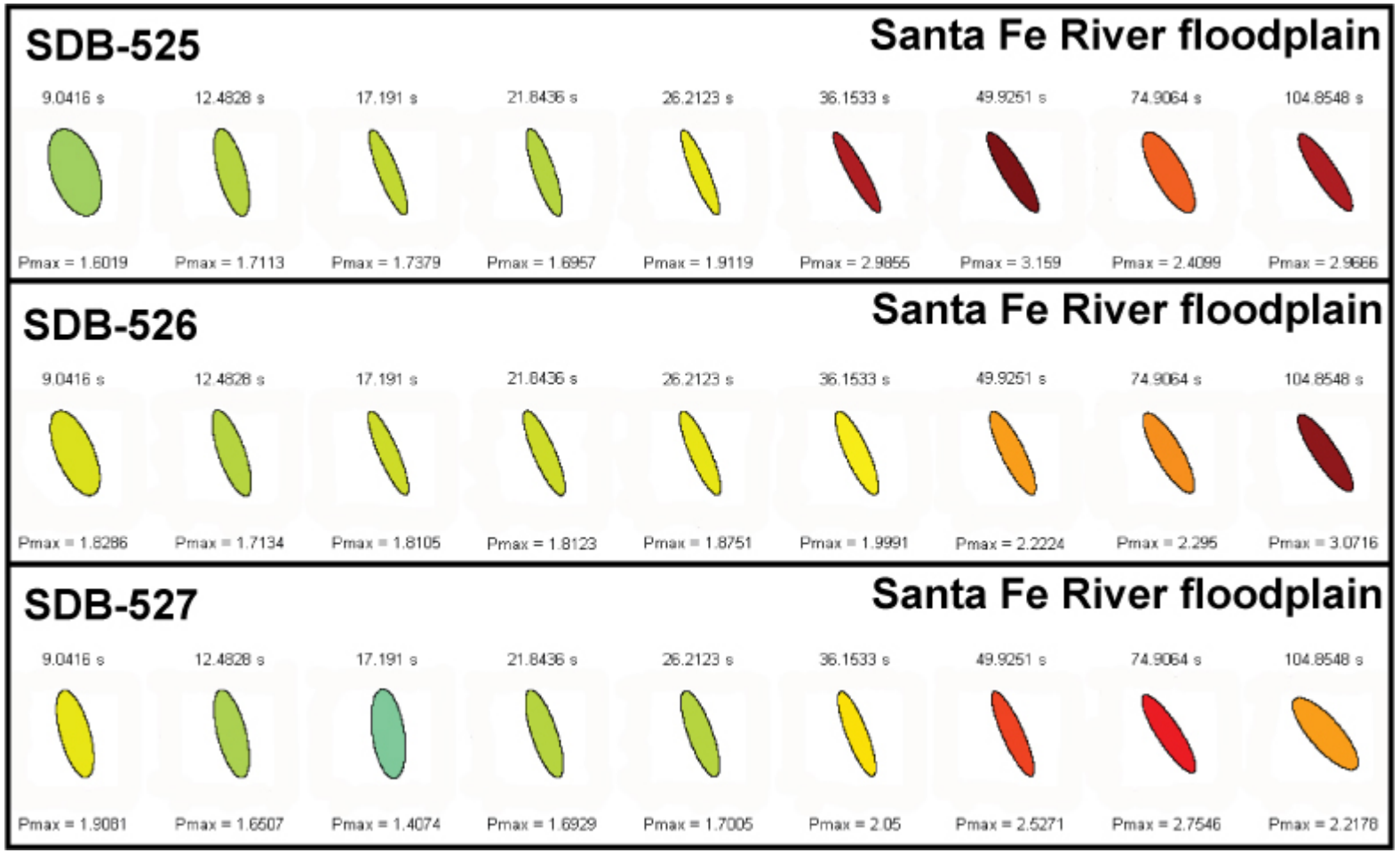

Figure 21. Long period phase tensor plots from MT soundings on the western end of the profile. The numbers above each plot indicate the period in seconds. The fill color and the Pmax value both indicate the maximum phase value used to normalize the plots.

SDB-003 and SDB-004 are outside the basin on La Bajada Mesa. The MT soundings on the western end of the survey lie within the basin but on the Santa Fe River floodplain and have different orientations of their long axis when compared to soundings up on the La Majada Mesa (SDB-001 and SDB-002). These differences may indicate that there is a possible change in the geoelectric strike within the basin related to the basement rock or may the result of differences in the properties of the sediments near the river and up on the mesa. In either case the results violate the invariance of geoelectric strike that is strictly assumed when using a 2-D inversion code.

A compromised rotation angle was reached after examining the MT soundings, SDB-001 and SDB-002, and a complete Bouguer gravity anomaly map (Figure 22). From the figure one can see a trend in both the polar diagrams and phase tensor plots at these two sites that relates to the trend in the gravity contours. The long axes of the diagrams and plots are aligned with a direction of ~N45E which is also aligned with the N45E trends in the gravity contours. This trend is chosen to be the geoelectric strike direction for all the 2-D modeling.

MT IMPEDANCE TENSOR ROTATION

Since a smooth 2-D inversion is to be applied to the data, the multi-dimensional impedance tensor,

$$\mathbf{Z} = \begin{bmatrix} \mathbf{Z}_{xx} & \mathbf{Z}_{xy} \\ \mathbf{Z}_{yx} & \mathbf{Z}_{yy} \end{bmatrix}, \tag{5}$$

needs to be rotated to the impedance tensor that would have resulted from the survey profile line being setup perpendicular to geoelectric strike. This requires minimizing the diagonal elements and maximizing the off diagonal elements, i.e.,

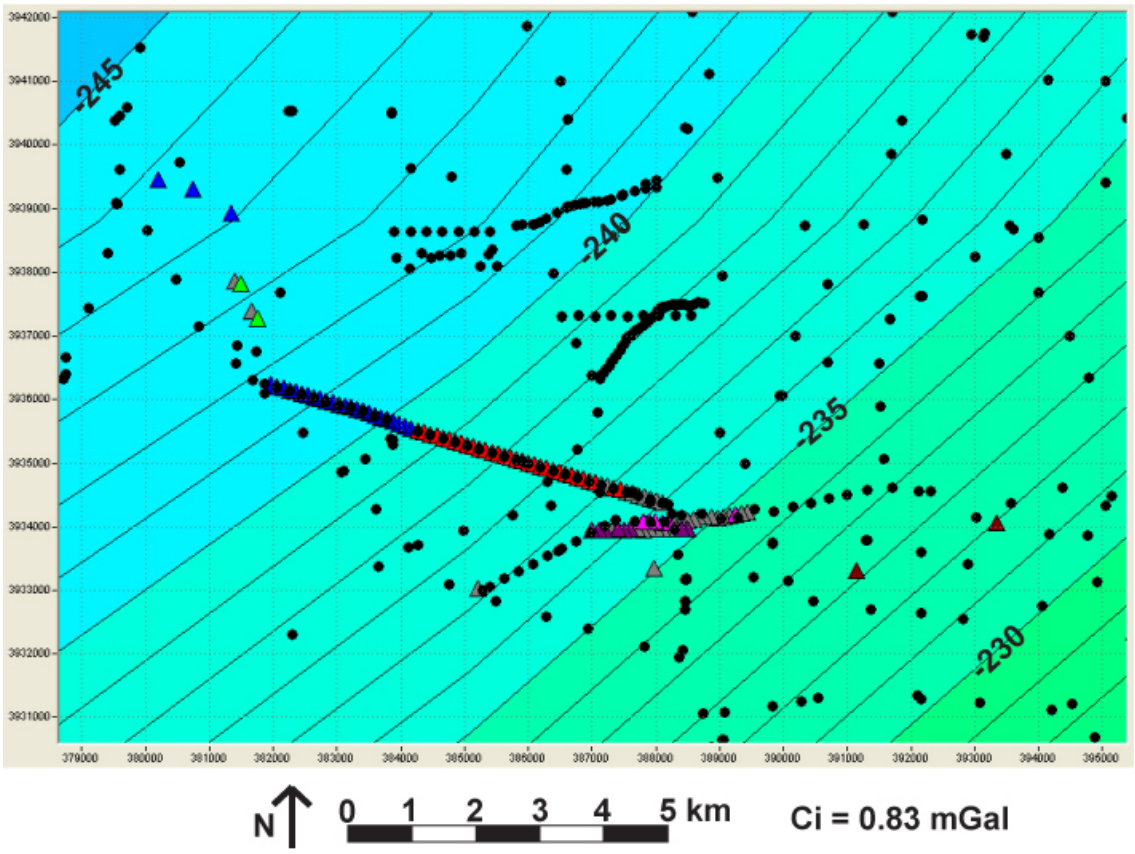

Figure 22. Regional complete Bouguer anomaly map. Black dots indicate locations of the gravity measurements. Colored triangles indicate locations of MT soundings. Contour lines indicate trends in the gravity data and thus a possible direction of geoelectric strike.

$$\mathbf{Z}_{2D} = \begin{bmatrix} 0 & \mathbf{Z}_{xy} \\ \mathbf{Z}_{yx} & 0 \end{bmatrix}, \tag{6}$$

consistent with a 2-D Earth. If the diagonal elements are actually equal to zero after the rotation then the impedance tensor represents exactly the theoretical 2-D Earth case. If it is exactly the theoretical 2-D Earth case, the rotation angle would be the same at all MT sites along the profile and at all sounding periods.

In order to correctly invert the data to utilize the 2-D smooth inversion capabilities of WinGLink the MT soundings must be rotated perpendicular to the compromised geoelectric strike direction using the following equations

$$\mathbf{Z}'_{xx} = \mathbf{Z}_{xx}\cos^2\alpha + (\mathbf{Z}_{xy} + \mathbf{Z}_{yx})\sin\alpha\cos\alpha + \mathbf{Z}_{yy}\sin^2\alpha\,, \tag{7}$$

$$\mathbf{Z}'_{xy} = \mathbf{Z}_{xy}\cos^2\alpha + (\mathbf{Z}_{xx} + \mathbf{Z}_{yy})\sin\alpha\cos\alpha - \mathbf{Z}_{yx}\sin^2\alpha\,, \tag{8}$$

$$\mathbf{Z}'_{yx} = \mathbf{Z}_{yx}\cos^2\alpha + (\mathbf{Z}_{yy} + \mathbf{Z}_{xx})\sin\alpha\cos\alpha - \mathbf{Z}_{xy}\sin^2\alpha\,, \tag{9}$$

and

$$\mathbf{Z}'_{yy} = \mathbf{Z}_{yy}\cos^2\alpha + (\mathbf{Z}_{yx} + \mathbf{Z}_{xy})\sin\alpha\cos\alpha - \mathbf{Z}_{xx}\sin^2\alpha \tag{10}$$

where α is the rotation angle. The SAGE MT soundings were rotated implementing these equations in the WinGLink software and then projected onto an inversion profile trending in the direction of N45W or 135º azimuth.

MT MODE IDENTIFICATION

The polar diagrams and phase tensor plots of the long period soundings have indicated possible mode identifications but up until this point the apparent resistivity and phase curves have not been identified as to what MT mode they represent. All the apparent resistivity and phase curves need to be identified prior to the 2-D inversion process. If the resistivity distribution is 2-D depending on both the x and z directions, $\rho(x,z)$, then there exist two distinct polarizations of the electromagnetic wave corresponding to the electrical field aligned with or normal to the independent coordinate (y). When the electric field is normal to and the orthogonal magnetic field is aligned with the y direction this polarization is known as the transverse magnetic (TM) polarization because the magnetic field is transverse

to the plan of symmetry, the x-z plane. When the electric field is aligned with and the orthogonal magnetic field is normal to the y direction this polarization is known as the transverse electric (TE) polarization because the electric field is transverse to the plan of symmetry. These two polarizations are the basis for the two 2-D MT modes, the TM mode and the TE mode.

If the geoelectric strike direction was known ahead of time, the survey could have been set up where the assigned x direction was exactly perpendicular to geoelectric strike and the assigned y direction was exactly parallel to geoelectric strike direction. In this hypothetical ideal case the $\mathbf{e}_x$ (e-field in the x direction) and $\mathbf{h}_y$ (h-field in the y direction) data would form $\mathbf{Z}_{xy}$ and would represent the TM mode. Similarly the $\mathbf{e}_y$ (e-field in the y direction) and $\mathbf{h}_x$ (h-field in the x direction) data would form $\mathbf{Z}_{yx}$ and would represent the TE mode. But knowing the geoelectric strike direction ahead of time is not always the case. The survey was set up with the profile, x direction, trending N73W or 107º azimuth and with the orthogonal electric dipoles, y direction, trending N17E or -163º azimuth. This setup was approximately perpendicular to the La Bajada fault zone. The geoelectric strike direction was found to be N45E meaning the ideal profile set up direction, perpendicular to geoelectric strike, would have been N45W direction or 135º azimuth. This requires a tensor impedance rotation from the original profile direction of approximately 28° clockwise. This means that for the present work the impedance element $\mathbf{Z}_{xy}$ should represent the TM mode while impedance element $\mathbf{Z}_{yx}$ should represent the TE mode, i.e. the rotation is 28° which is less than 90°. A rotation angle greater than 90° would require that the x and y directions to be switched.

This mode identification was verified by examining mode splits in the apparent resistivity curves. In the case of a vertical contact separating two different resistivity distributions (Figure 23) the TM mode is discontinuous, while the TE mode is continuous across the interface resulting in the splitting of the sounding curves (Appendix C). When the sounding curves coincide as in the 1-D case, the modes are identical and are therefore not defined. The relationship between the larger impedance magnitude and the MT mode is key.

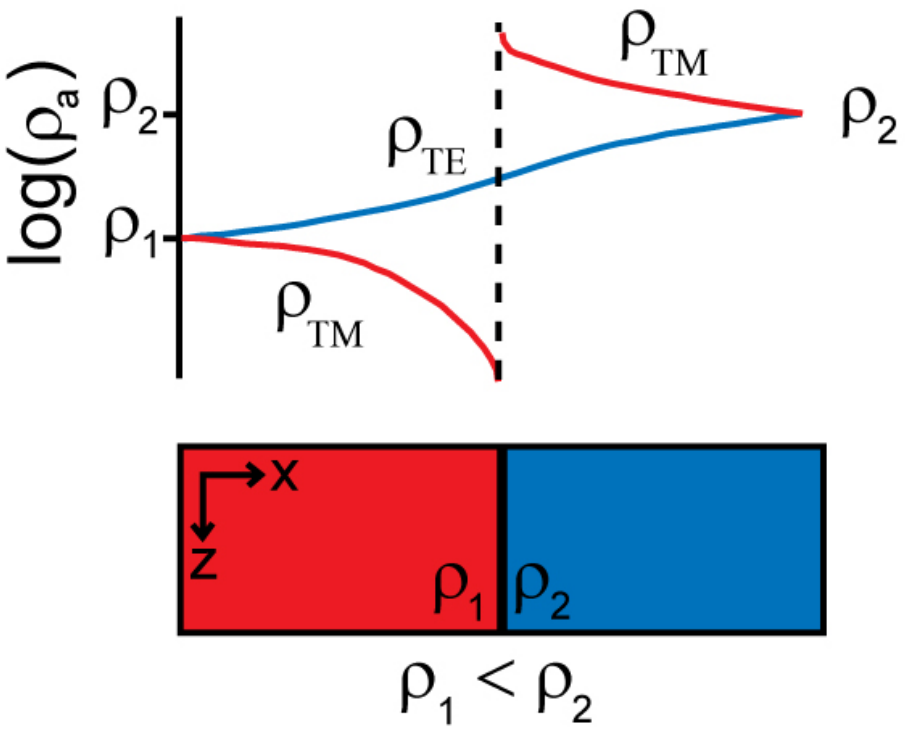

Figure 23. The results of a vertical contact on the TM and TE mode apparent resistivity curves. The TE mode is continuous across the contact while the TM mode is not (modified from Jiracek et al., 1995).

On the conductive side near the boundary, the TE mode is larger in magnitude then the TM mode while on the resistive side the TM mode impedance magnitude is greater than the TE mode impedance magnitude. In a simple conductive basin like the Santo Domingo Basin the TE apparent resistivity curve will always be above the TM apparent resistivity curve

(Appendix C). From studying the MT mode splits the MT modes were identified and the MT modes associated with the Z_{xy} curves are identified in Table 1 for each MT sounding.

Some issues that did arise in the identification process related to the Quantec Titan and Geometrics Stratagem data sets. Even if the Titan system was set up ideally, perpendicular to geoelectric strike and the magnetic field was constant in the geoelectric strike direction, the TM mode measurements would correspond to true MT mode measurements, but the TE mode measurements would not correspond to true MT mode measurements. This is because the magnetic field measurements recoded would not be correct for the TE mode. The result is that the Titan TE mode measurements can be thought of as normalized electric field measurements instead of true TE mode measurements. All of the Titan soundings from 2005 did not record long enough periods to indicate a mode split and in essence can be looked upon as 1-D. The 2007 AMT soundings were recorded at frequencies well above any basement-causing mode splits. Also presented in Table 1 is the number of data points resulting from a resampling of D+ smoothed, edited log apparent resistivity and phase versus log period data allowing for five data points per decade.

MT Static Shift Correction

The MT method is susceptible to static shifts in the apparent resistivity curves due to a build up of electrical charges resulting from near-surface inhomogeneities and/or topographic effects (Pellerin and Hohmann, 1990). Static shifts are easily identified by parallel offsets in the TE and TM apparent resistivity curves with no associated change in the impedance phase curves at high frequencies/short periods (Figure 24). The shifts are referred

Table 1. Identified TE Mode and Number of Data Points per Sounding Curve (from a D+ smoothing of the data allowing for five points per decade)

Station	TE	Data	Station	TE	Data	Station	TE	Data
SDB-525	xy	23	**SDB-522**	yx*	23	**SDB-224**	yx	23
SDB-526	xy	23	**SDB-523**	yx*	23	**SDB-225**	yx	25
SDB-527	xy	23	**SDB-524**	yx*	25	**SDB-226**	yx	26
SDB-702	yx*	15	**SDB-201**	yx	29	**SDB-227**	yx	27
SDB-704	yx*	17	**SDB-202**	yx	29	**SDB-228**	yx	27
SDB-501	yx*	28	**SDB-203**	yx*	28	**SDB-229**	yx	29
SDB-502	yx*	27	**SDB-204**	yx	28	**SDB-230**	yx	29
SDB-503	yx*	27	**SDB-205**	yx	28	**SDB-233**	yx	27
SDB-504	yx*	27	**SDB-206**	yx*	28	**SDB-234**	yx	27
SDB-505	yx*	27	**SDB-207**	yx	28	**SDB-301**	yx	22
SDB-506	yx*	27	**SDB-208**	yx	28	**SDB-302**	yx	17
SDB-507	yx*	28	**SDB-209**	yx	28	**SDB-303**	yx	17
SDB-508	yx*	27	**SDB-210**	yx*	25	**SDB-305**	yx	19
SDB-509	yx*	28	**SDB-211**	yx	28	**SDB-306**	yx	22
SDB-510	yx*	24	**SDB-212**	yx	28	**SDB-307**	yx	22
SDB-511	yx*	28	**SDB-213**	yx	29	**SDB-101**	yx	12
SDB-512	yx*	27	**SDB-214**	yx	28	**SDB-102**	yx	12
SDB-513	yx*	25	**SDB-215**	yx	28	**SDB-103**	yx	12
SDB-514	yx*	25	**SDB-216**	yx	28	**SDB-104**	yx	16
SDB-515	yx*	25	**SDB-217**	yx	28	**SDB-105**	yx	11
SDB-516	yx*	25	**SDB-218**	yx	26	**SDB-315**	yx	17
SDB-517	yx*	25	**SDB-219**	yx	28	**SDB-316**	yx	17
SDB-518	yx*	25	**SDB-220**	yx	28	**SDB-116**	xy	16
SDB-519	yx*	25	**SDB-221**	yx	28	**SDB-003**	yx	26
SDB-520	yx*	25	**SDB-222**	yx	28	**SDB-004**	yx	26
SDB-521	yx*	25	**SDB-223**	yx	27	**TOTAL**		**1887**

*** Indicates that there is no clear mode split in the sounding curves.**

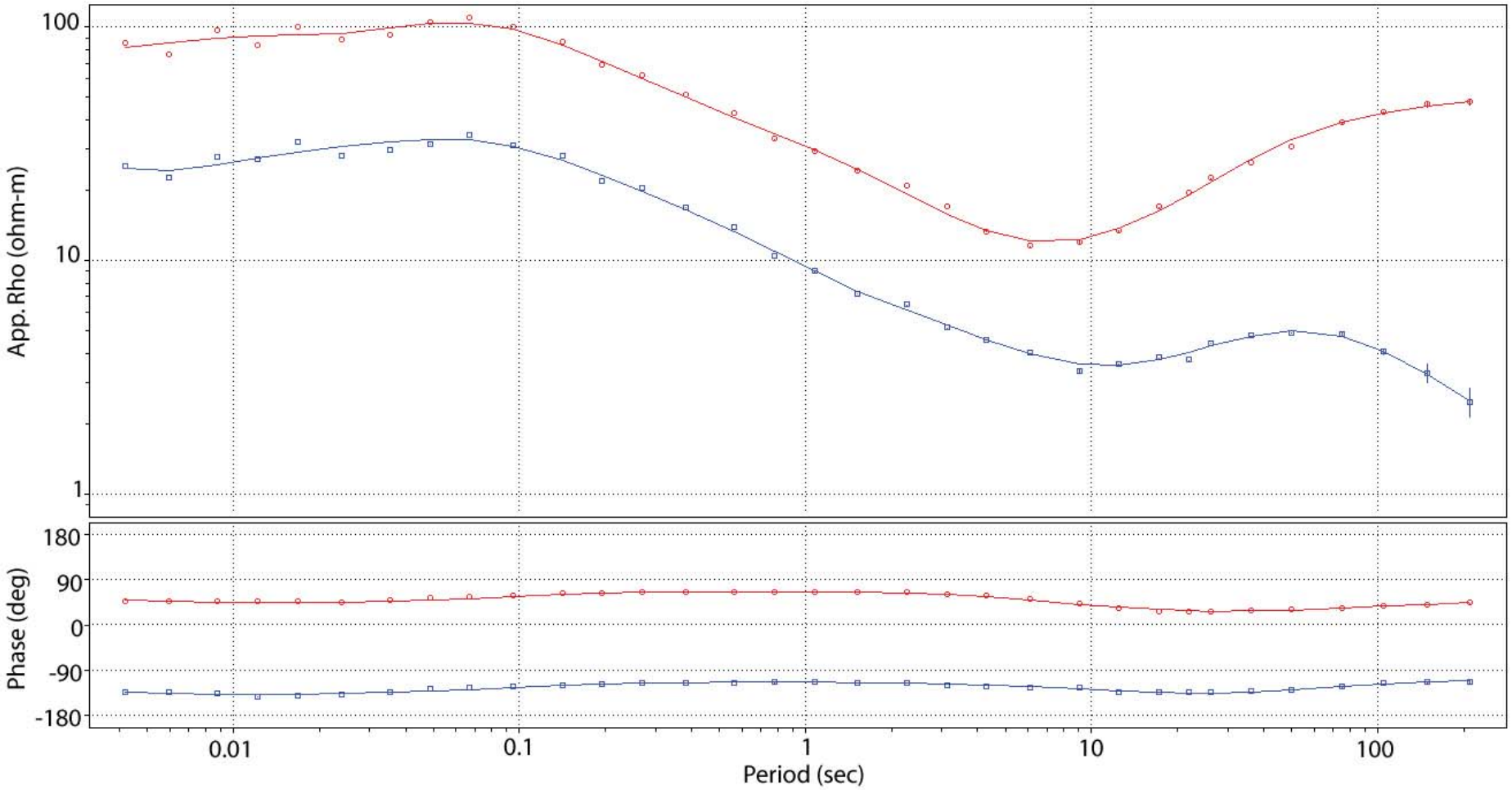

Figure 24. An example of a static shift in apparent resistivity curves from MT sounding SDB-526. The red apparent resistivity curve, TE mode, needs to be shifted down to the blue apparent resistivity curve, TM mode. Notice the lack of any apparent change in the impedance phase curves.

to as being static because the conservation of current at conductive discontinuities is not a time-dependent process (Simpson and Bahr, 2005).

Further information is needed to determine which direction to shift the curves in order to correct for the static shift. The electrical charge build up is responsible for the static shifts which mainly affects the electric field measurements. So it is natural to consider geophysical techniques that instead measure the magnetic field as a means to identify and correct for the shifts (Pellerin and Hohmann, 1990). TEM measurements are commonly transformed into pseudo MT apparent resistivity sounding curves and used for this purpose. Static shifts may occur were both TE and the TM curves are shifted by the same amount and in the same direction. In this case a comparison to a TEM pseudo MT apparent resistivity curve would be the only way to identify the presence of a static shift.

In WinGLink, pseudo MT apparent resistivity curves were computed from 1-D TEM inversions and were used as a guide for determining the proper static shift correction applied for each MT apparent resistivity sounding curve (Table 2). TEM measurements however were not recorded at every MT sounding location so if there was not a colocated TEM sounding then the nearest appropriate TEM sounding was used.

MT Sounding Inclusion and Exclusion

Since some spatial overlap occurs in the MT soundings after they are rotated and projected onto the profile, some soundings cannot be included in the smooth 2-D inversion. A careful review of these soundings is required in order to pick the most appropriate set of sounding based on data quality, frequency range, and data similarity/differences to include in

Table 2. Minimal Static Shifts Utilizing the Appropriate TEM Sounding Curve Applied to the MT Sounding Apparent Resistivity Curves

Station	xy	yx	Station	xy	yx	Station	xy	yx
SDB-525	0.434	1.000	**SDB-522**	1.000	1.000	**SDB-224**	1.042	1.896
SDB-526	0.307	1.000	**SDB-523**	1.000	1.000	**SDB-225**	0.472	2.075
SDB-527	0.233	1.000	**SDB-524**	1.000	1.000	**SDB-226**	0.594	1.372
SDB-702	1.358	1.000	**SDB-201**	1.228	1.343	**SDB-227**	0.571	1.000
SDB-704	1.000	0.367	**SDB-202**	1.301	1.549	**SDB-228**	0.582	1.000
SDB-501	1.000	1.000	**SDB-203**	1.492	1.461	**SDB-229**	0.627	1.000
SDB-502	0.849	1.000	**SDB-204**	1.425	1.548	**SDB-230**	0.589	1.000
SDB-503	1.000	1.000	**SDB-205**	1.729	1.485	**SDB-233**	0.705	1.000
SDB-504	1.000	1.000	**SDB-206**	1.692	1.676	**SDB-234**	0.751	1.000
SDB-505	1.000	1.000	**SDB-207**	1.460	1.520	**SDB-301**	1.000	0.830
SDB-506	1.000	1.000	**SDB-208**	1.484	1.440	**SDB-302**	1.000	0.726
SDB-507	1.000	1.000	**SDB-209**	1.620	1.306	**SDB-303**	0.650	0.394
SDB-508	1.000	0.766	**SDB-210**	1.685	1.381	**SDB-305**	0.791	0.779
SDB-509	0.655	0.681	**SDB-211**	1.488	1.366	**SDB-306**	1.000	0.758
SDB-510	1.000	1.000	**SDB-212**	1.740	1.450	**SDB-307**	1.000	1.000
SDB-511	1.000	1.000	**SDB-213**	1.554	1.488	**SDB-101**	1.000	1.000
SDB-512	1.000	1.000	**SDB-214**	1.684	1.553	**SDB-102**	1.000	1.000
SDB-513	1.000	1.000	**SDB-215**	1.841	1.494	**SDB-103**	1.000	1.000
SDB-514	1.000	1.000	**SDB-216**	1.893	1.488	**SDB-104**	1.000	1.000
SDB-515	0.762	0.925	**SDB-217**	1.707	1.435	**SDB-105**	1.000	1.000
SDB-516	1.000	1.218	**SDB-218**	1.711	1.450	**SDB-315**	0.735	0.834
SDB-517	1.000	1.000	**SDB-219**	1.000	1.000	**SDB-316**	0.664	1.000
SDB-518	1.000	1.573	**SDB-220**	0.847	1.000	**SDB-116**	1.000	1.000
SDB-519	0.974	1.411	**SDB-221**	0.720	1.161	**SDB-003**	1.000	1.000
SDB-520	1.000	1.000	**SDB-222**	0.661	1.147	**SDB-004**	1.000	1.000
SDB-521	1.000	1.000	**SDB-223**	1.267	1.847			

If > 1.000, the curve was moved up. If < 1.000, the curve was moved down.

the inversion. Quesada (2004) went through a similar review of the soundings with his work however a slightly different sounding subset is preferred with the present work.

The overlapping soundings in question are located on the eastern end of the survey where several different data sets from SAGE 2000-2003 are combined. In agreement with Quesada (2004) on the SAGE 2000soundings, soundings SDB-003 and SDB-004 are included while SDB-001 and SDB-002 are rejected based on their non similarity with other soundings within the basin. With the soundings from 2001, the first five soundings on the western end of the line are included as with Quesada but the choice of the single sounding chosen on the eastern end of the survey is different. Quesada has chosen to include SDB-117 (Quesada's MT102) while I have chosen to include SDB-116. In sounding SDB-117 there is a large mode split at the beginning of the sounding which does not appear consistent with other nearby soundings while sounding SDB-116 does not display this feature. Of the soundings from 2002, Quesada and I both agreed not to include soundings SDB-231 and SDB-235 through SDB-241. I have in addition decided not to include sounding SDB-232. These choices are based on poor data quality and the availability of better quality, longer period data from the SAGE 2001 and 2003 years. With the SAGE 2003 soundings, Quesada has chosen to include only the first seven on the western end and the last three soundings on the eastern end of the survey line. My sounding selection here is the same but with the additional exclusion of station SDB-304 on the western end and station SDB-314 on the eastern end again because of poor data quality.

Data collected during the summer SAGE 2007 season included four AMT soundings and the data quality was poor. The apparent resistivity curves were heavily edited and two of the four soundings were rejected because they were found to be too noisy and were not

included in the 2-D inversion. These rejected stations are SDB-701 and SDB-703. Only SDB-702 and SDB-704 were included in the 2-D inversion.

Final processing of the MT data prior to inversion resulted in a set of 77 MT soundings that were edited to remove bad points, rotated and projected onto a profile line aligned along a direction of N45W or 135 degrees azimuth, identified as either TM or TE curves, shifted to correct for static shifts, and selected based on data quality, frequency range, and similarities/differences. Table 3 lists the number of soundings, frequency range, and equipment used for the various SAGE years.

SMOOTH 2-D INVERSION

The solution to the MT inversion problem given the measurements made at the surface solved by WinGLink is the resistivity distribution of the subsurface. Difficulties arise because the data are incomplete and noisy. The problem is stated as

$$d_i = F_i(m) + e_i \tag{11}$$

where d_i, i = 1,2,…,N, are the observed data, $F_i(m)$, $F_1(m)$,…,$F_N(m)$, are nonlinear forward modeling functions, m is the modeled resistivity distribution, and e_i, i = 1,2,…,N, are the error or noise. The data are log apparent resistivity and impedance phase values for a particular frequency and MT mode, TE or TM. The errors are associated with the calculation of the impedance elements from the MT processing step where the errors have been propagated through to apparent resistivity and impedance phase errors. The inverse problem is non-unique meaning there are many models that equally fit the data within a given misfit. Stability is also a factor with the inverse problem because arbitrary small errors in the data can still generate arbitrary large errors in the solution model (Oldenburg and Li, 2005). The

Table 3. SAGE Data Sets, MT Equipment, Period Range, and Number of Soundings Included in the 2-D Inversion

SAGE Year	Soundings Collected	Soundings Used	Equipment	Period Range (s)	Edited Period Range (s)	Analog to Digital Resolution	Remote Reference	Tipper
2000	4	2	EMI, MT24	0.004 - 750	0.004 - 750	24 Bit	Yes (Station)	Yes
2001	18	6	EMI, MT24	0.003 - 210	0.02 - 92	24 Bit	Yes (Station)	No
2002	41	32	Quantec, Titan 24	0.00007 - 55	0.00007 - 55	24 Bit	Yes	No
2003	16	8	Zonge, GDP-32	0.0001 - 1429	0.002 - 128	16 Bit	No	No
2005a	24	24	Quantec, Titan 24	0.00007 - 26	0.00009 - 26	24 Bit	Yes	No
2005b	3	3	Quantec, Spartan	0.004 - 210	0.004 - 210	24 Bit	Yes (Station)	Yes
2007	4	2	Geometrics, StataGem	0.00001 - 0.1	0.003 - 0.064	18 Bit	No	No
Total	110	77						

inverse problem is solved through a joint minimization of the data misfit and spatial roughness by minimizing an objective function, $\phi(m)$,

$$\phi(m) = \chi(m) + \tau\psi(m) \tag{12}$$

(Jiracek et al, 1986). The function $\chi(m)$ is the classic chi squared data misfit function

$$\chi(m) = \sum_{i=1}^{N} \left(\frac{d_i - F_i(m)}{\sigma_i}\right)^2 \tag{13}$$

where σ_i, i = 1,2,…,N, are the variance of the error. Again the error is from the MT processing step. The function $\psi(m)$ is a measure of the spatial roughness

$$\psi(m) = \int_0^{z_{max}} \int_{x_{min}}^{x_{max}} (\nabla^2 m)^2 \, dxdz \tag{14}$$

where m is the model parameter associated with a model cell with dimensions ($x_{min} \le x \le x_{max}$) by ($0 \le z \le z_{max}$). In the WinGLink software the Laplacian operator is approximated by a simple, second-difference operator matrix (Rodi and Mackie, 2001). The symbol τ is the regularization parameter which is a positive number that controls the relative importance of data misfit and spatial roughness in the minimization (Jiracek et al, 1986).

The smooth 2-D inversion routine in WinGLink is based on the Rodi and Mackie (2001) nonlinear conjugate gradient algorithm, an iterative algorithm that performs line searches utilizing a modified Gauss-Newton method directed along search directions determined by a non-linear conjugate gradient method. Should a line search fail to converge a steepest decent method is then implemented. Initially in the algorithm, a forward model is run providing an initial reference model. Then a series of line searches are carried out along computed search directions where the model with the smallest objective function is saved. The line search converges if the estimated value for the objective function agrees with the

actual objective function within some prescribed tolerances. If the line search converges then a new search direction is computed. If the line search fails then the new search direction is taken to be the steepest descent direction breaking the conjugacy with the pervious search direction.

Within the 2-D smooth inversion routine in WinGLink, several ways to customize the starting model are available. The size and density of the cells in the model space are two aspects that can be modified. Two starting grid models are included in the program based on the MT skin depth concept (Appendix A), a coarse grid and a fine grid. With the present data set, the coarse grid option contains 31 rows and 89 columns while the fine grid option contains 231 rows and 581 columns. The program allows for the modification of these default choices with the addition and removal of rows and columns where needed, but it is problematic because it extends these row and column choices throughout the model space. The result is a finer grid where it is needed but at the computational expense of the same fine grid at depth and the extremities of the model where it is not needed. The starting grid for the present work contains 74 rows and 179 columns. The initial resistivity values assigned to each cell are another parameter of the starting model that can be adjusted. An a priori model can be included by selecting the appropriate resistivity for each cell and has the benefit of reducing the inversion time. For the present work the starting model was a 100 ohm-m half space where the cells were modified to include topography (Figure 25).

Additional parameters include the amount and type of data to invert on. A single MT mode, TE or TM apparent resistivity and phase data, can be selected to invert on or a joint inversion on both MT modes can be selected. For the present work a joint inversion was preformed. Another parameter is to invert on the actual data or a smoothed version of the

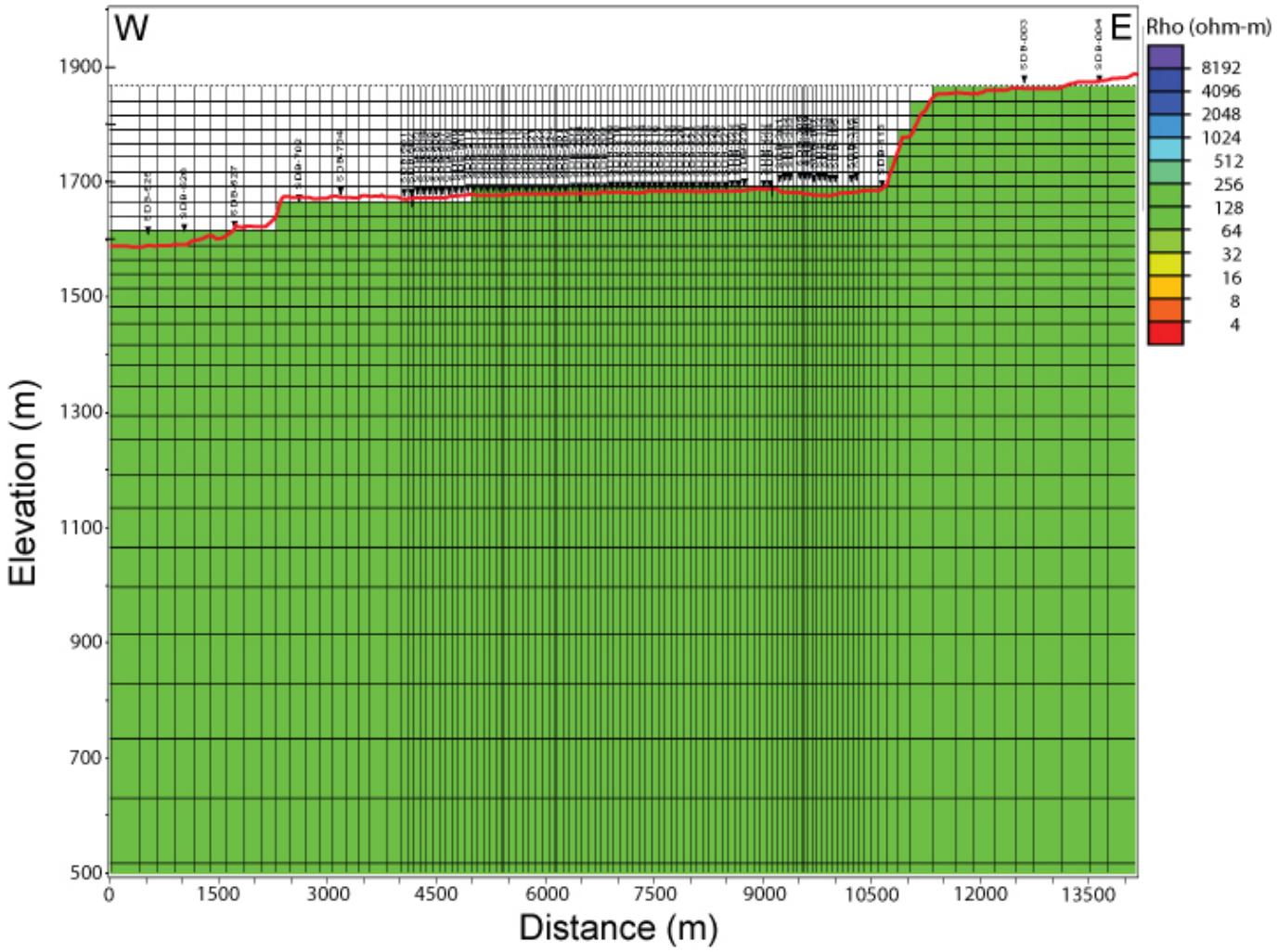

Figure 25. The homogeneous half-space starting model used in the 2-D inversion. The model contains 74 rows and 179 columns. The cell values are set to 100 ohm-m in the earth and 0 ohm-m in the air to correspond to the back projected elevations, red line.

data. If the smooth data option is selected the choice of smoothing method, the number of points per decade, the minimum frequency, and number of decades is required. In the present work the smooth data option was selected using the D+ smoothing option with five points per decade with the minimum frequency of 0.001 Hz and allowing for eight decades of data. The regularization parameter, τ, can also be changed in WinGLink. For the present work, several different values for the regularization parameter were chosen and the inversion was run to convergence. The results of varying the regularization parameter (Figure 26)

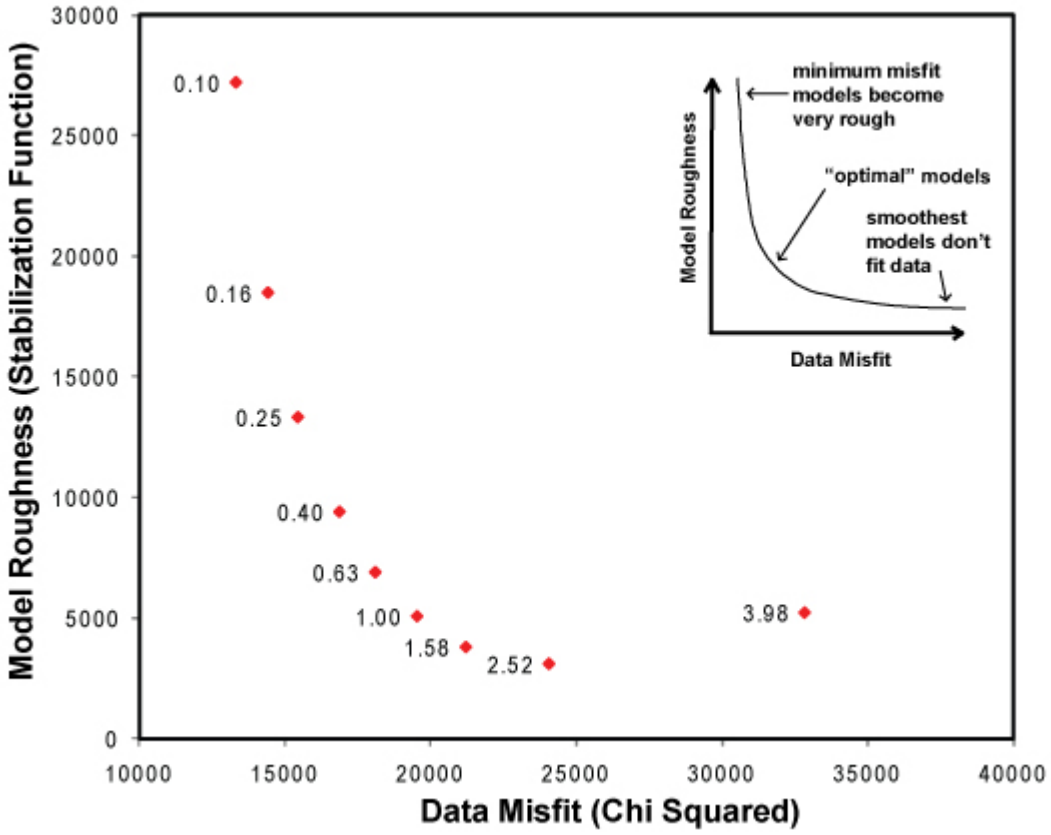

Figure 26. A plot of the data misfit versus model roughness. The points plotted represent smooth 2-D inversions carried out using the indicated regularization parameter, τ. The 2-D inversion model constructed using a regularization of τ = 1.00 appears to provide an acceptable trade-off between data misfit and model roughness.

indicate that a value of $\tau = 1.00$ would provide an acceptable trade-off between data misfit and model roughness for the present work. Values to the right of the point label 1.00 produce smooth models at the expense of larger data misfits, i.e., they under fit the data. Values to the left of the point labeled 1.00 produce smaller values of data misfit but at the expense of a rougher model, i.e., they over fit the data. The error floors used in the inversion can also be modified but in the present work were left at the default settings of 5.000 %.

Due to the non-uniqueness of the inverse problem the resulting model is one of many whose response fits the observed data within a given misfit. In the present work, the inversion result (Figure 27) using a $\tau = 1.00$ and starting with a 100 ohm-m half space (Figure 25) contains four questionable features. The first feature, (1), is a resistive prong extending upward into the large conductive layer central to the model. A second feature, (2), is a resistive break in the near-surface conductor on the eastern end of the model. A third feature, (3), is a sharp slope to the resistive basement layer on the western end of the model. The fourth feature, (4), is a vertically conductive region that separates the resistive basement layer central to the model.

Whether or not the data actually support these features or not can be examined with sensitivity testing. The particular feature was hypothesized to not exist and the region containing the feature was assumed to be laterally continuous. This hypothesis was implemented by modifying the cell resistivity values thus creating a new starting model (Figure 28). The effect of this change on the RMS (root mean squared) errors at the individual stations were then evaluated after a single forward inversion iteration using this new starting model. The original model and the resulting model RMS values were visually compared for the four questionable features (Figure 29). In test 1 the RMS errors were very

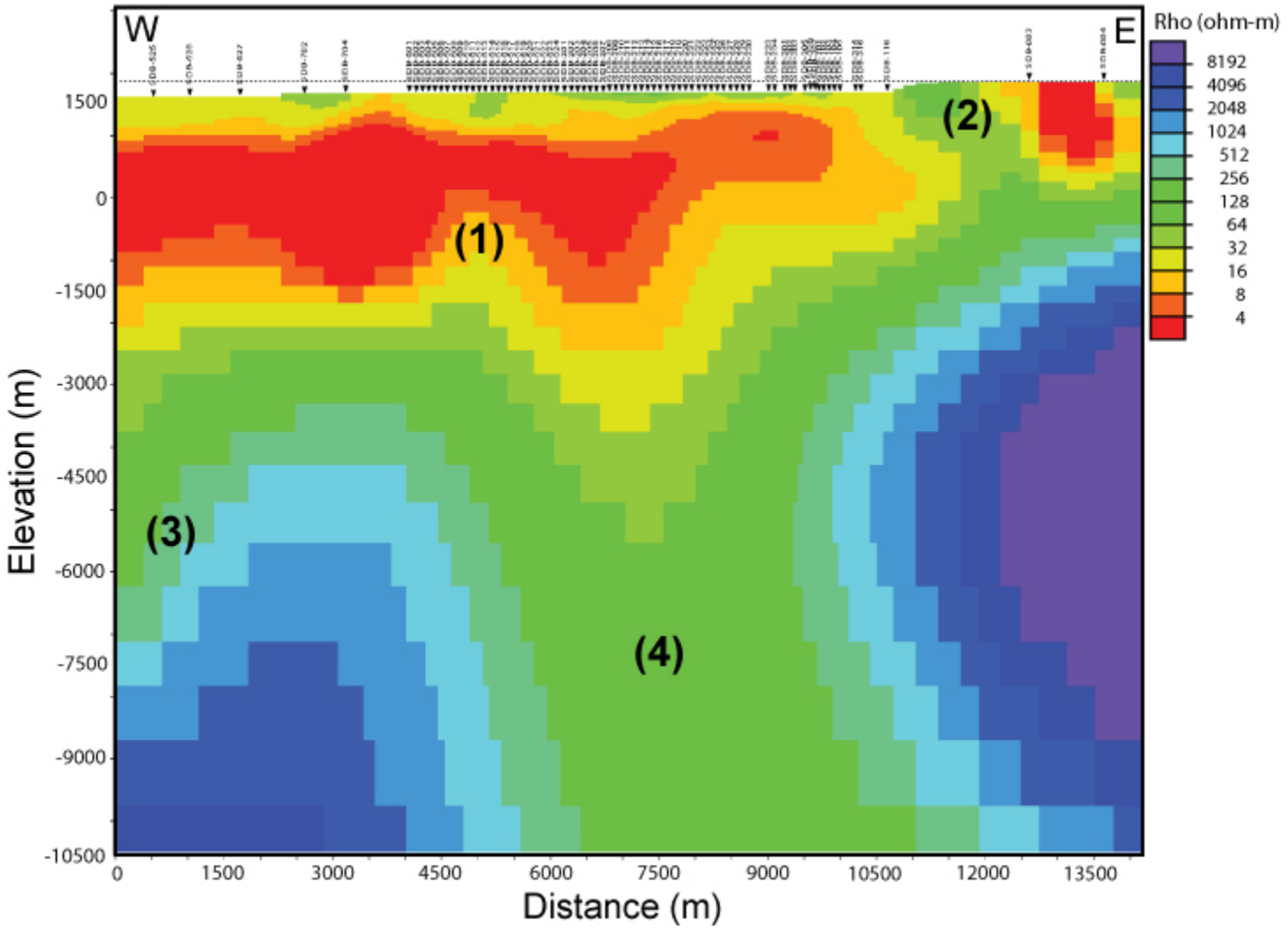

Figure 27. A smooth 2-D MT inversion model constructed using a $\tau = 1.00$. The numbered regions indicate four questionable features present in the model. Are these features required by the model to fit the data?

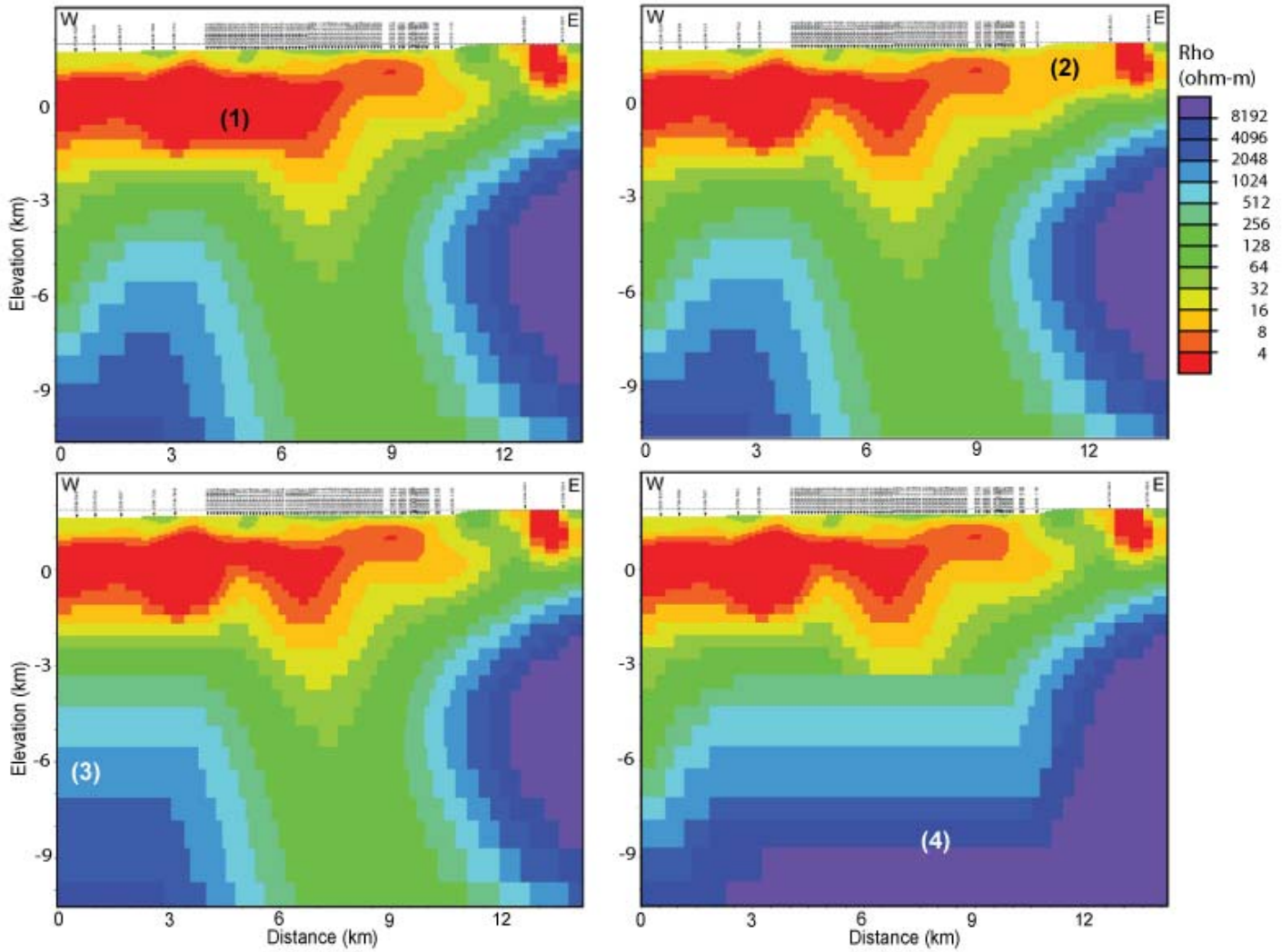

Figure 28. A set of four hypothesized continuous layer models used to test the 2-D inversion model. Numbers refer to questionable features present in the original model (Figure 27).

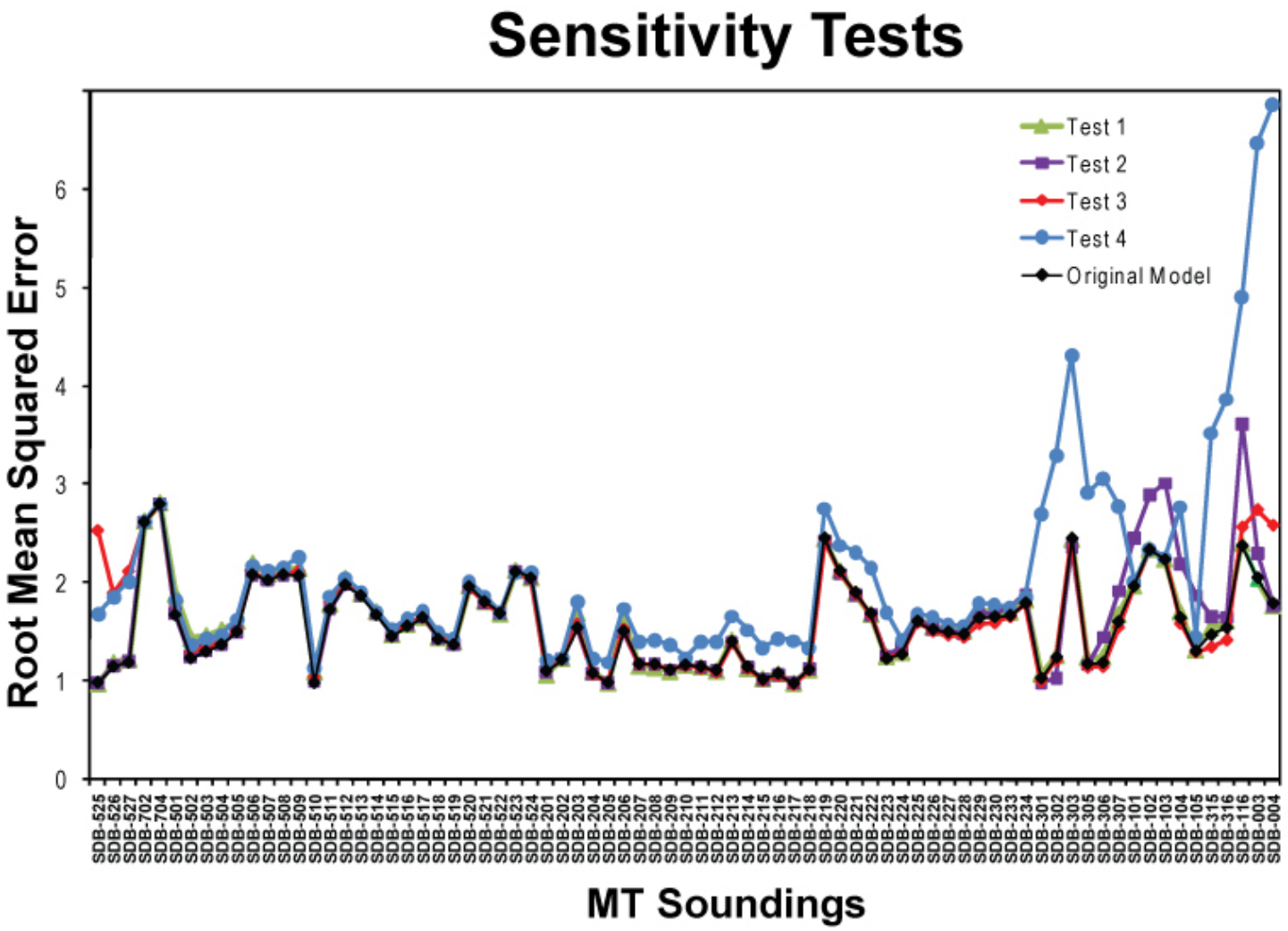

Figure 29. A plot of the RMS error versus MT sounding for each of the four sensitivity tests. The original model is in black. The results from one forward iteration using the four hypothesized continuous starting models (Figure 28) are shown with the colored lines.

close to the original values leading to the conclusion that feature (1) in Figure 27 was not required by the data. Tests 2 and 3 showed some mismatch between the original RMS values and because the features (2) and (3) are in regions of sparse MT soundings or are on the ends of the profile line these tests were found to be inconclusive. Test 4, which tested the presence of the large conductive break in the resistive basement, showed a large mismatch with the original RMS error values (Figure 29). In the case of feature (4), the resulting forward model was then used as a starting model and twenty additional inversion iterations were run to allow for the model resistivities and station RMS errors to readjust. The mismatch between the original model and the new model after twenty inversion iterations and was now more comparable (Figures 30). This indicates that the deep vertical conductive feature seen in the initial model (Figure 27) is not required to be as broad and conductive as in the original model to fit the data at the given RMS error level of misfit. However, the feature does seem to be required to fit the data.

A second way to visually present the sensitivity of the model and the four identified features is to look at a sensitivity map. There is an option in the WinGLink software to output a sensitivity map after it completes the smooth 2-D inversion routine. The results describe which parts of the model are more or less influential to the data. In Figure 31 are the results from a sensitivity test of the smooth 2-D model produced with $\tau = 1.00$ (Figure 27). A rough dividing line between regions that are more and less sensitive to the data is at an elevation of approximately -3000 m. This would indicate that the acceptable model should be terminated at approximately this elevation. Also, all four questionable features are in less sensitive regions when compared to the surrounding sensitivity values implying that these features are necessarily required by the observed data. Although both the comparison

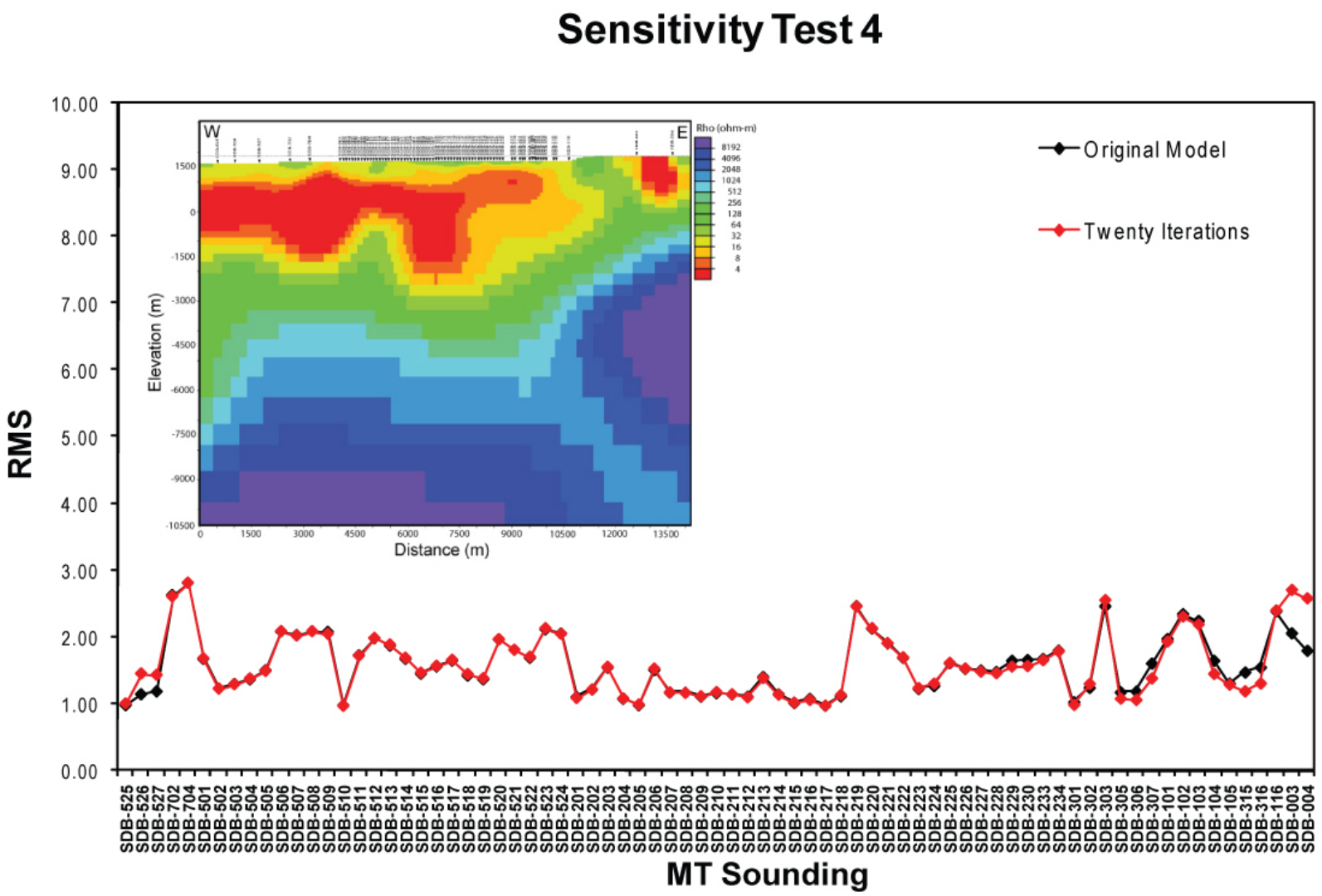

Figure 30. The hypothesized continuous resistive basement model, test 4, after twenty iterations. The conductive feature is narrower and less conductive but still present in the model.

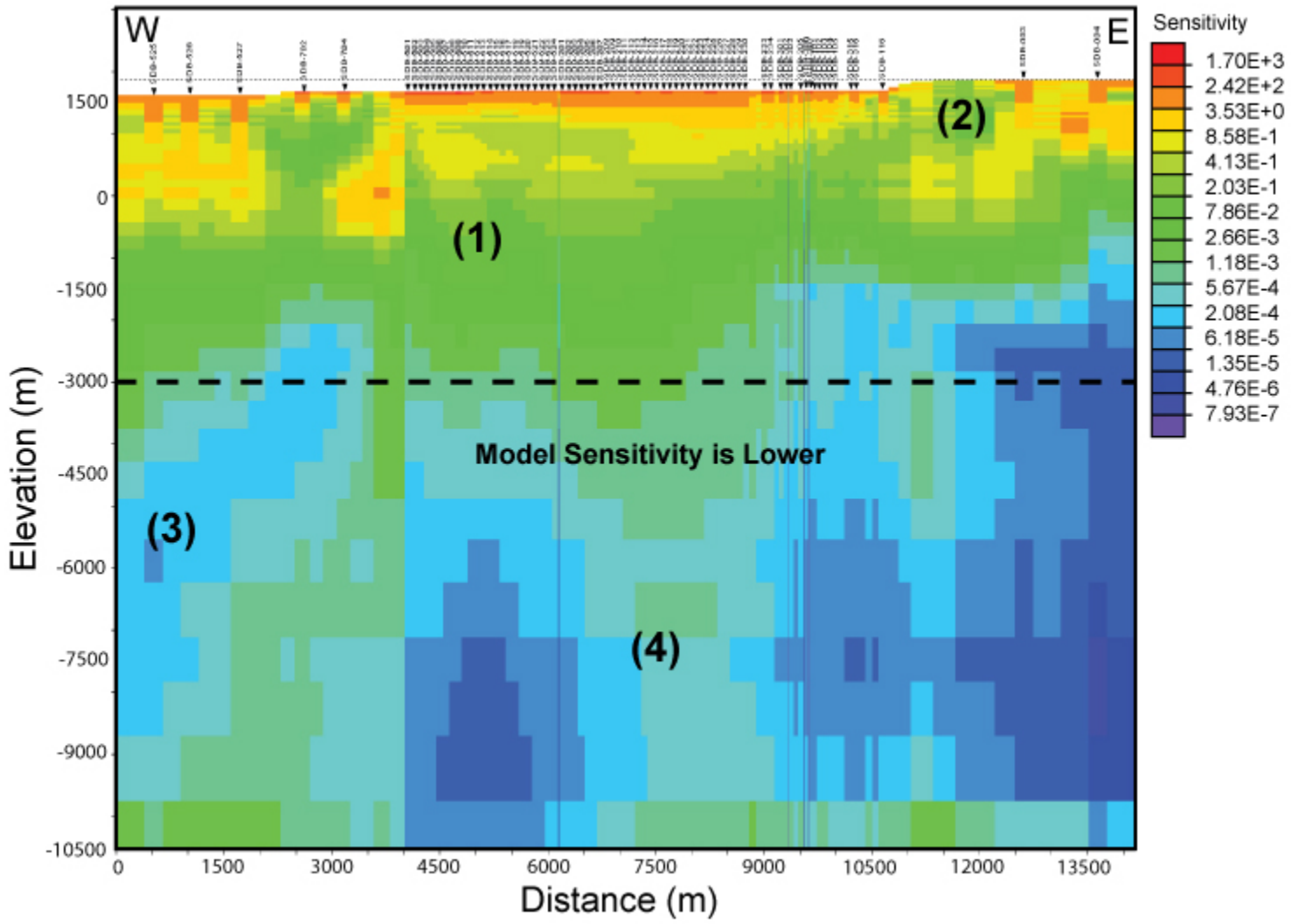

Figure 31. A sensitivity map for the smooth 2-D MT inversion model (Figure 27). The sensitivity map indicates lower model sensitivity below an elevation of -3000 m. Numbers refer to the four questionable features present in Figure 27.

of RMS errors (Figures 29 and 30) and the sensitivity map (Figure 31) are quantitative measures, there are no simple, objective criteria to reject or accept features in inverse MT resistivity models using Geosystem's WinGLink software. This would necessitate evaluation of the assumption of model dimensionality, inherent resolution of the MT diffusive process, a rigorous propagation and analysis of data errors, as well as the trade-off between model roughness and data misfit as discussed earlier. At the present time I am unaware of a strategy to select preferred MT resistivity models that encompass all of these considerations and a degree of subjectivity and geologic plausibility is invoked.

CHAPTER 4

RESULTS AND DISCUSSION

The MT method resolves differences in the resistivities of materials and requires careful interpretation to relate the results back to geology, including tectonics and hydrogeology. The smooth 2-D inversion model (Figure 27) is a 2-D physical distribution of resistivity values. The resistivity values from the model can be compared to laboratory results of common Earth materials (Figure 32). From the laboratory work there is much overlap between the resistivity values of different Earth materials. The geologic units hypothesized in the subsurface of the Santo Domingo Basin are sedimentary units of various sands, silts, clays, gravel, and conglomerates containing varying amounts of water and salinity concentrations. Thus, based on resistivity values alone it was not possible to distinguish specific geologic units. However, the major conductive and resistive patterns present within the 2-D resistivity model were interpreted with the aid of additional geophysical data.

Resistivity well logs and DC resistivity measurements at the 3,367 m deep Shell Santa Fe Pacific No. 1 oil exploration well drilled in 1972 have aided the geologic interpretation of the medium to deeper sections of the smooth 2-D MT inversion model. The Shell Santa Fe well is located on the Ziana Horst at the southern end of the Santo Domingo basin (Figures 4 and 5) and has been interpreted as bottoming-out in Precambrian crystalline basement. Tops of stratigraphic horizons have been interpreted and published by Black and Hiss (1974). With minor exceptions, the geologic units identified in the borehole

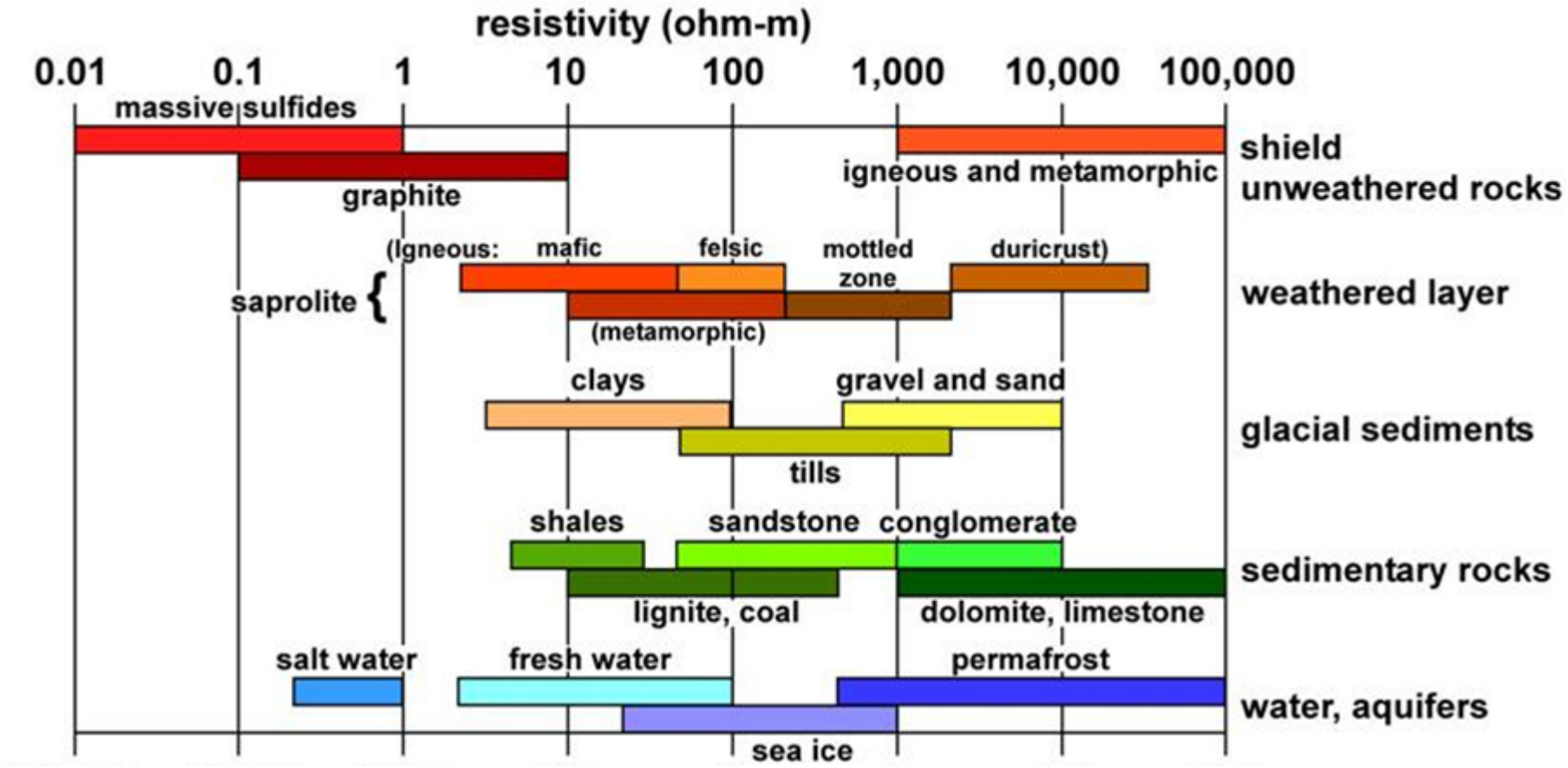

Figure 32. Laboratory resistivity values for various Earth materials. Very important values for the present work include fresh water, sandstones, conglomerates, clays, and sand/gravel (modified from Palacky, 1988).

geophysics well logs from Shell SFP No. 1 are the same as the ones hypothesized in the SAGE MT study. Figure 33a shows ranges of resistivity values for these units in the Shell SFP No. 1 borehole resistivity log. Also labeled in the figure are the major geologic units identified in the well log data that correlate to the hypothesized geologic units that underlie the SAGE MT study area. Two geologic units that stand out because of their low resistivity/high conductivity are the Eocene Galisteo Formation and the Triassic Chinle Group. The Eocene Galisteo Formation with its extremely low permeability and the underlying Late Cretaceous Mancos Shale act as a single hydrologic confining unit while the Triassic Chinle Group based on its high clay contents acts as the other hydrologic confining unit within the section (Minor, 2006). Notable highly resistive geologic units include the Permian Yeso and Abo Formations as well as the Pennsylvanian Madera limestone.

The resistivity proximity log cited here is not the most ideal data to compare with the MT results. This is because the electric current from the borehole resistivity instrument does not penetrate into the formations very far beyond the drilling effects of the borehole. Also, the applied and measured electric fields are mostly vertical and not horizontal as in MT measurements. A DC resistivity model based on the results of a deep Schlumberger-equatorial DC resistivity survey carried out at the Shell Santa Fe well site is shown in Figure 33b (Jiracek et al., 1976). DC resistivity measurements have similar resolution capabilities as MT soundings resulting in a better correlation then with borehole resistivity data. The DC resistivity model, however, does not appear to detect the presence of the highly resistive Permian units identified in the borehole results.

In Figure 34 the resistivity curves for MT soundings SDB-527 and SDB-522 derived from smoothed, finite difference cell values from the 2-D inversion model (Figure 30) are

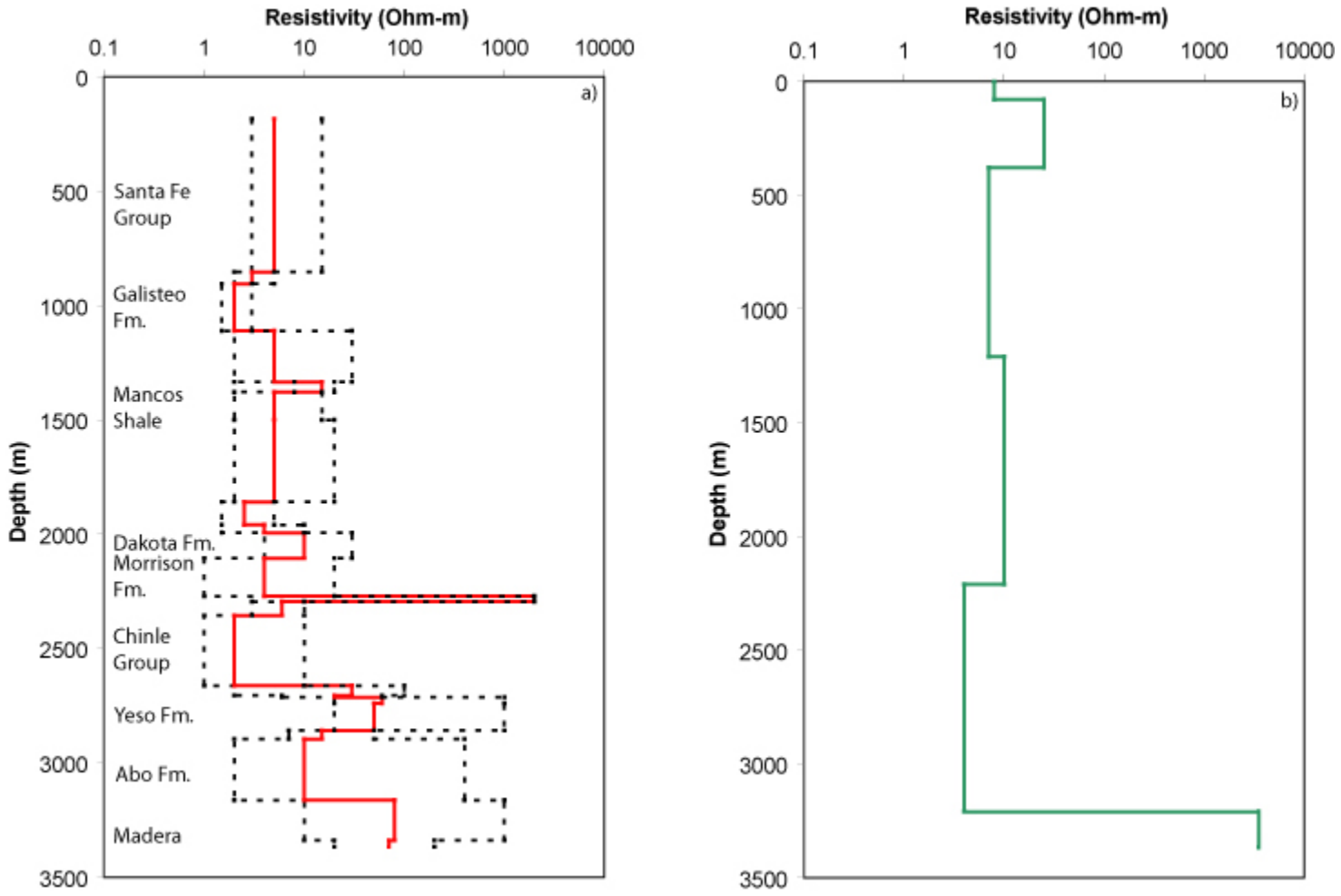

Figure 33. The Shell SFP No. 1 resistivity well log and Schlumberger-equatorial DC resistivity model centered at the well site. In (a) the interpreted geologic units are matched to the upper and lower bounds of resistivity values within each unit as indicated by the black dashed lines while the red line indicates the average value. In (b) the green curve is the DC resistivity model.

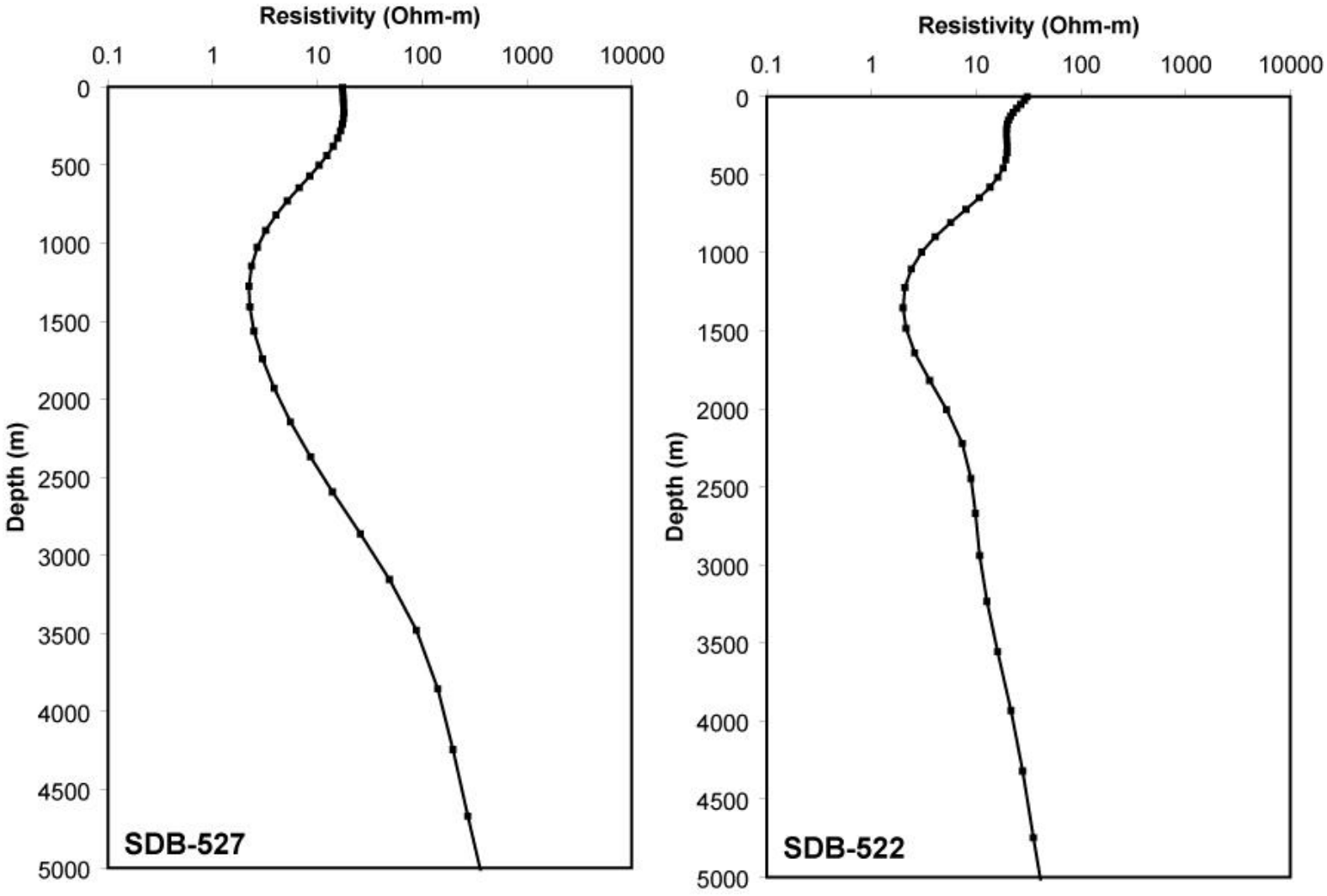

Figure 34. Resistivity curves extracted from the 2-D smooth inversion model (Figure 30). The plot on the left is from the long period Spartan SDB-527 sounding on the Santa Fe River floodplain while the plot on the right is from the Titan SDB-522 sounding near the 180 well.

presented. Sounding SDB-527 is a long period Quantec Spartan sounding recorded on the Santa Fe River floodplain while sounding SDB-522 is the closest Quantec Titan sounding to the 180 water well approximately 270 m due southwest. What is clear in both resistivity curves is the top of a low resistivity (2 ohm-m) section that can be directly correlated with the Eocene Galisteo Formation identified in the Shell Santa Fe Pacific No. 1 well (Figure 33a). The top of the Eocene Galisteo Formation was also identified at a depth of 695 m in the Yates Petroleum La Mesa No. 3 oil exploration well 14 km to the east of the study area (Quesada, 2004). This is in good agreement with a laterally projected top of the low resistivity layer. This very conductive unit has the effect of masking the deeper less conductive layers identified in the Shell SFP No. 1 resistivity well log. This is the case for the Triassic Chinle Group. In order for a deeper conductive layer like the Chinle Group with similar resistivity as the Galisteo Formation to manifest itself in the MT inversion results the conductivity-thickness product must be larger than the sum of all the layers above it (Jiracek et al., 1995). Much of the Mesozoic units that underlie the highly conductive Eocene Galisteo Formation are poorly resolved partly due to the masking effects of the Galisteo and partly due to the smoothing of the inversion code. To be able to resolve a resistive layer at depth with MT its thickness must be greater than the sum of the thicknesses above it. The deeper MT resistivity values do approach the higher resistivity values for the Paleozoic and Precambrian units identified in the Shell SFP No. 1 borehole resistivity well log which implies that the basement thickness exceeds its depth.

To aid in the interpretation of the shallower geologic section, water well logs from the city of Albuquerque and the nearby Cochiti Pueblo were examined. The near-surface geological units include Quaternary sediments overlying Santa Fe Group sediments (Figure

10). From induction logs of Albuquerque's 435 m deep West Mesa No. 3 well, 490 m deep Don Well No. 1, and 495 m deep Don Well No. 2 the resistivities range from 20 - 400 ohm-m with the average of 150 ohm-m. This average resistivity is much higher then most resistivity values in the upper 500 m of the Santo Domingo Basin (Figure 34) and is confirmed by results of a borehole resistivity log from the CEPO No. 2 Sliding well on the Cochiti Pueblo (Figure 35). This well is located approximately 10 km northwest and 62.5 m lower in elevation than station SDB-522 on the SAGE MT survey. The Sliding well recorded the water table at 37.5 m. The 180 well, 270 m southwest of MT sounding SDB-522, was drilled to 55 m with a recorded water table at 45 m (Minor, 2006). In Figure 36 the smooth resistivity curve from the 2-D inversion at MT station SDB-522 (Figure 34) is plotted to a depth of 2000 m. Also, in the right panel of Figure 36 are two three-layer, 1-D inversion models for the TE and TM modes. The TE and TM 1-D inversion models are very similar because the 2005 Titan soundings are approximately 1-D. In Figure 36, at the 180 well water table depth of 45 m, the resistivity values are between 14-16 ohm-m. This agrees with a resistivity value of 16 ohm-m for freshwater saturated undifferentiated Santa Fe Group on the Pajarito Plateau published by Baldridge et al. (2007).

Returning to the smooth 2-D MT inversion model (Figure 37), three distinct resistivity regions can be readily identified. Region 1 located to the west of MT station SDB-116 and comprises the very upper portion of the model extending from an elevation of ~1700 m at the surface down to an elevation of ~900 m under MT station SDB-210. The layer thickness ranges from ~350 m under MT station SDB-230 to ~800 m under MT station SDB-210. The resistivity values of region 1 range from 8 to 85 ohm-m. Region 2 occupies the majority of the model space and includes a highly conductive zone directly beneath region 1

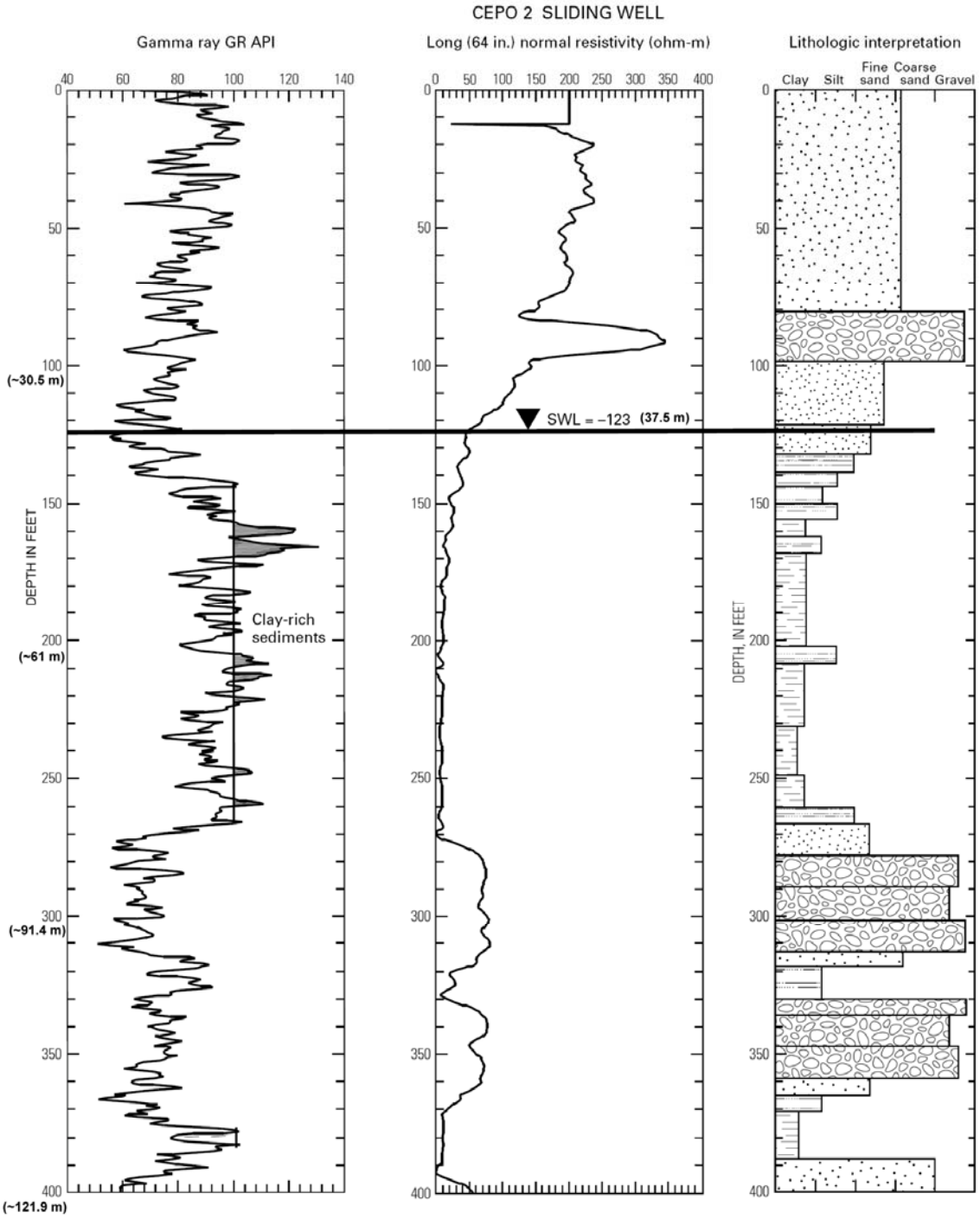

Figure 35. Well logs from of the CEPO (Cochiti Environmental Protection Office) No. 2 Sliding well. The logs include gamma ray, resistivity, and interpreted lithologic units. The CEPO No. 2 well is located approximately 10 km northwest of MT site SDB-522 and 62.5 m lower in elevation (modified from Minor, 2006).

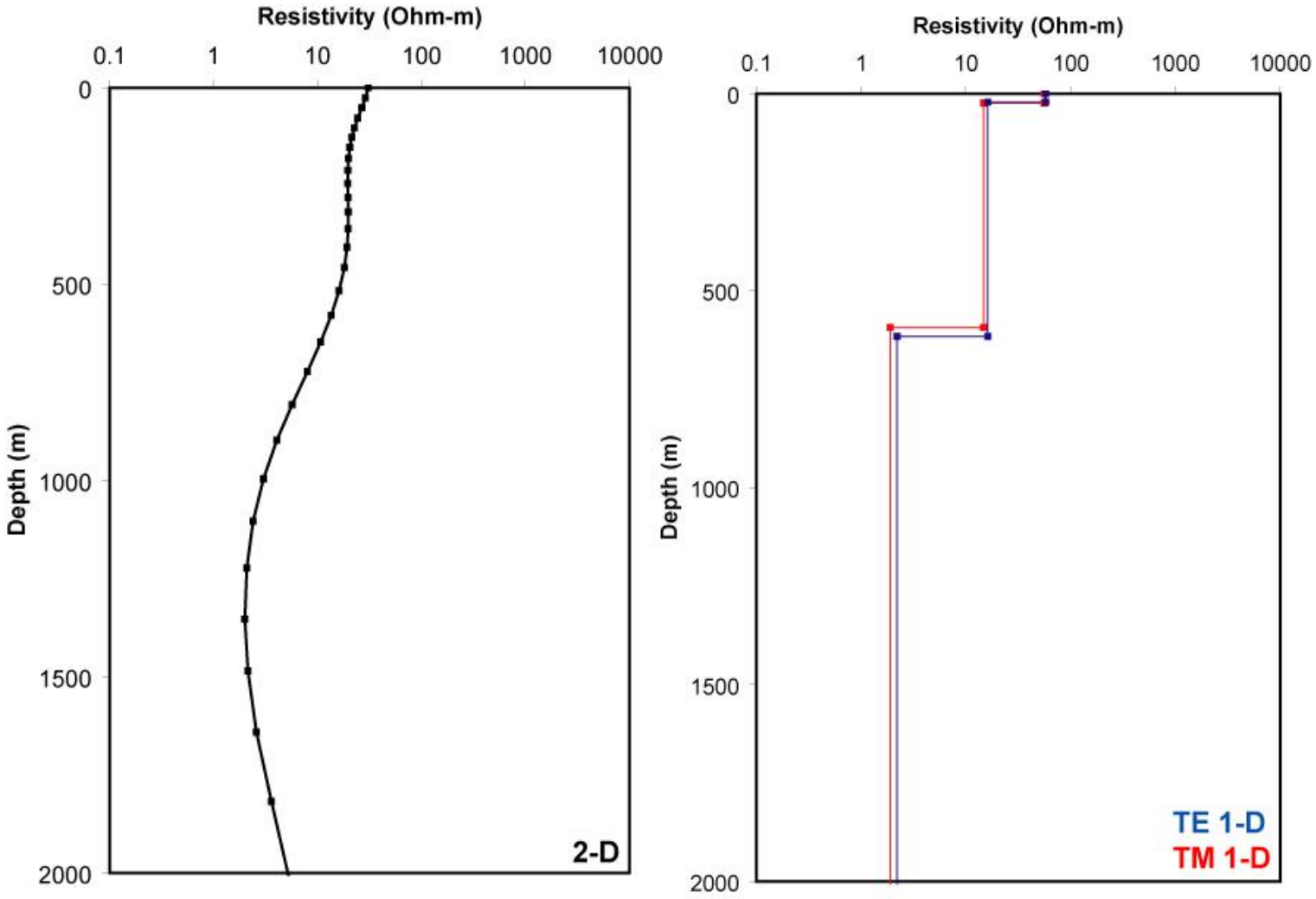

Figure 36. Resistivity curve and 1-D inversion results for MT sounding SDB-522. The resistivity curve on the left was extracted from the smooth 2-D inversion model (Figure 30). The 1-D inversion results on the right indicate a three layer resistivity model.

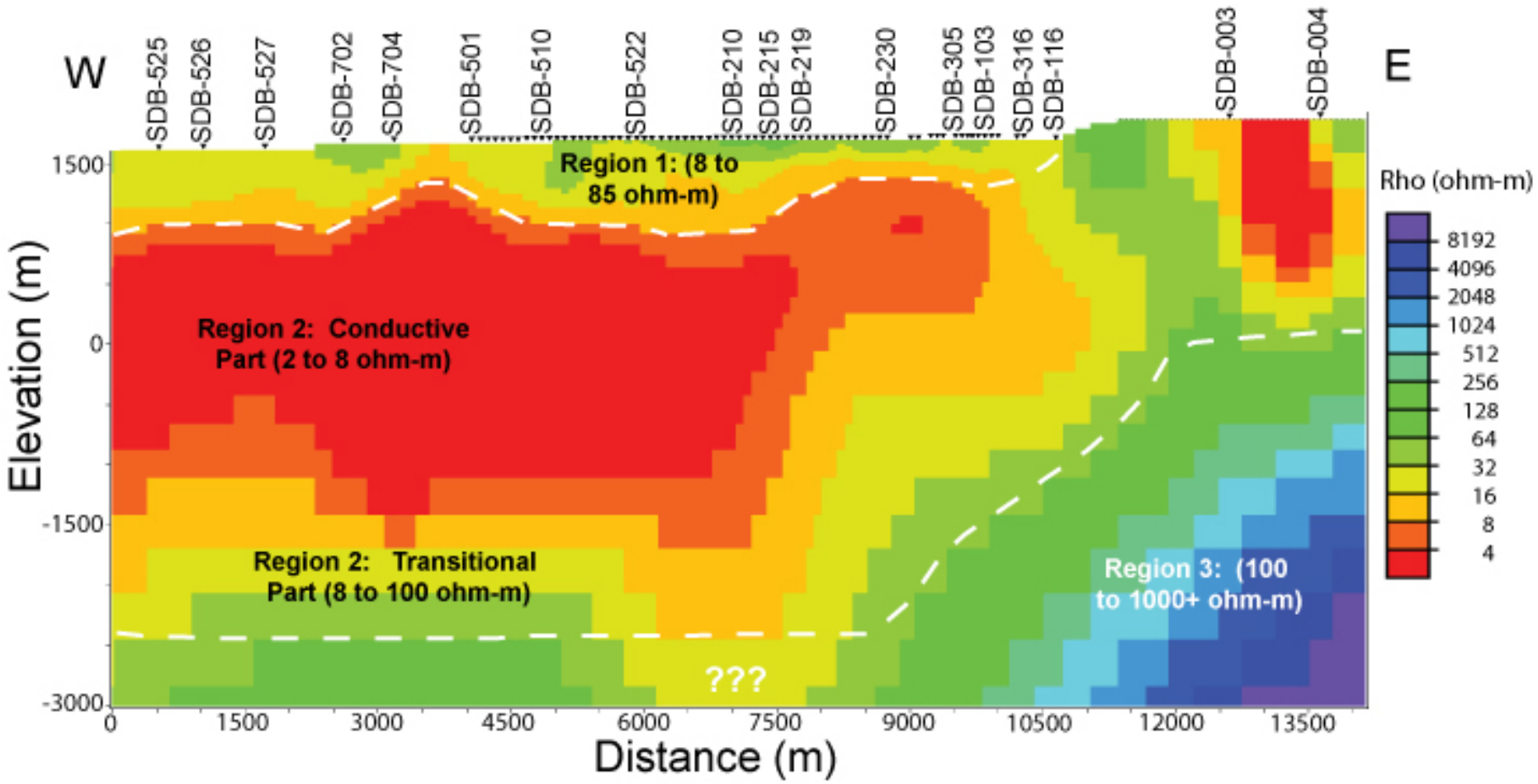

Figure 37. The three general resistivity regions present in the smooth 2-D MT inversion model. Region 1 has resistivity values in the range from 8-85 ohm-m. The conductive part of region 2 has resistivity values in the range from 2-8 ohm-m. The transitional part of region 2 has resistivity values in resistivity values in the range from 8-100 ohm-m. Region 3 has resistivity values in the range from 100 ohm-m to values well over 1000 ohm-m.

extending down to -1700 m in elevation (Figure 37). Resistivity values within this highly conductive zone varying from 2 to 8 ohm-m. Another component to region 2 is the bottom, transitional part where resistivity values gradually increase from 8 to 100 ohm-m (Figure 37). Region 3 which occupies the lower portion of the model is highly resistive with values ranging from 100 ohm-m to values that exceed 1000 ohm-m.

Region 1 is interpreted to be unsaturated to fresh water saturated basin fill. This is mainly based on well data from the 180 well that is centrally located to the profile, near MT station SDB-522. The water table depth in the 180 well was recorded at ~45 m and the water quality was recorded as fit for use in livestock grazing (Minor, 2006). The resistivity values for this region of 8 to 85 ohm-m also agree with the borehole resistivity values of Cochiti Sliding well mentioned above. From the thickness of region 1 and location within the geologic section, it is identified as the late to middle Cenozoic basin-fill. Because it is made-up of high porosity, high permeability, unconsolidated sands and gravel it is a prime freshwater aquifer (Minor, 2006 and Quesada, 2004).

Region 2 has a highly conductive section that must contain a larger percentage of clay and/or more saline water. The resistivities range from 2 to 8 ohm-m. This top of this section is associated with the Eocene Galisteo Formation that has also been identified at a similar depth, 695 m, in the Yates La Mesa No. 3, 14 km to the east. This highly conductive section includes Galisteo Formation through the Mesozoic units. Due to its higher conductivity, if pore fluids are present they will need to be brackish to highly saline. The amount of pore fluid is uncertain because resistivity measurements are highly sensitive to pore fluid interconnectivity and less than one percent, highly connected fluid can be measured (Jiracek et al., 1995). Beneath the highly conductive layer there is a transitional part of region 2 that

extends down to the highly resistive region 3. In MT, the depth to the top of the conductor, i.e. the thickness of the resistive layers above it, is the best constrained value. The bottom of the conductive layer is not well-defined because its conductivity-thickness product is what is best resolved, not it's thickness alone. The choice of trade-off parameter between model roughness and data misfit used in the smooth 2-D inversion of the data may be a large controlling factor as well. The choice of a $\tau = 1.00$ was slightly biased towards a smoother model. Therefore, the bottom of region 2 could be a sharp boundary between geologic units or it could be a gradual transition. This can not be resolved by the MT measurements. Well log results from the Shell SFP No. 1 well (Figure 33) indicate that the bottom of region 2 could be the Yeso and Abo Formations.

However, the Paleozoic Permian Yeso and Abo rocks maybe also be present in the top section of region 3 overlying the highly resistive early Paleozoic Pennsylvanian Madera limestone and Precambrian crystalline basement. The exact boundary between region 2 and 3 is uncertain and has arbitrarily been identified with the resistivity value of 100 ohm-m indicating a possible Abo Formation Madera limestone boundary as seen in the Shell SFP No. 1 well. The Shell SFP No. 1 well has been interpreted by Shell to bottom out into Precambrian granitic basement. The depth to basement is thought to be best estimated under the long period MT soundings on either end of the survey and not very well constrained in the rest of the survey as shown from the sensitivity testing preformed on the central part of region 3. From laboratory results (Figure 32) the high resistivity values may be attributed to either unweathered igneous and metamorphic crystalline rocks or to dolomite and limestone. An interpretation of early Paleozoic Pennsylvanian Madera limestone on top of Precambrian

granitic basement is in possible agreement with the Schlumberger-equatorial DC resistivity sounding. The interpreted regions are displayed in Figure 38.

There is considerable vertical variation within the three regions. Region 1 appears to thin between MT stations SDB-704 and SDB-501 and again east of MT station SDB-219. The conductive zone of region 2 thins beneath MT station SDB-219. There is a noticeable offset of 200-300 m in the conductive zone to the east of MT station SDB-219. The model is not very well-resolved to the east of MT sounding SDB-316 due to the reduced number of soundings and topographic influence of the La Bajada Fault escarpment. In region 3 the highly resistive (1000+ ohm-m) zone is shallower in the model to the east of SDB-316 with a maximum elevation of -1000 m. The highly resistive region also appears under the western MT stations from SDB-527 to SDB-501 at -5500 m in Figure 27, if we believe the model sensitivity here.

The variations in the regional thicknesses and overall patterns have been interpreted as relating to structural features. These interpreted structural features include a series of basin faults. Quesada (2004) recognized an offset in the highly conductive part of region 2 under MT stations to the east of SDB-215 (MT-220 in Figure 39). Quesada also inferred igneous intrusive bodies to the west and east of this offset from aeromagnetic data (Figure 39). With the extension of Quesada's work presented here, the indicators of the two parallel faults are reproduced and identified as being two different strands of the La Bajada Fault. The identification of the igneous intrusive bodies is unclear with the addition of the present work.

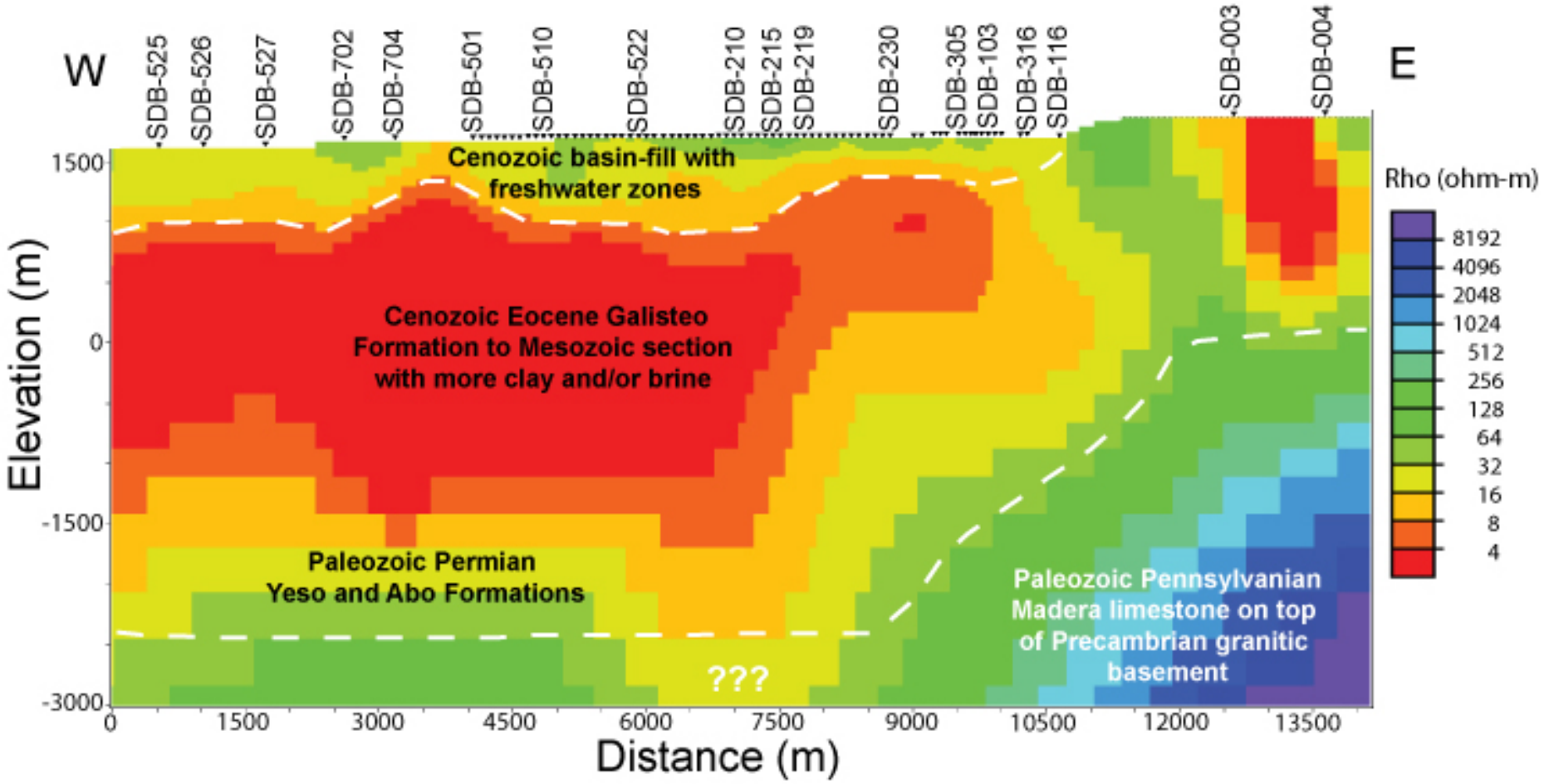

Figure 38. A geologic interpretation of each region presented in Figure 37. Region 1 is late to middle Cenozoic basin-fill. Region 2 includes the Cenozoic Eocene Galisteo Formation through the Paleozoic Permian Abo Formation. Region 3 includes the Paleozoic Pennsylvanian Madera limestone on top of Precambrian granitic basement.

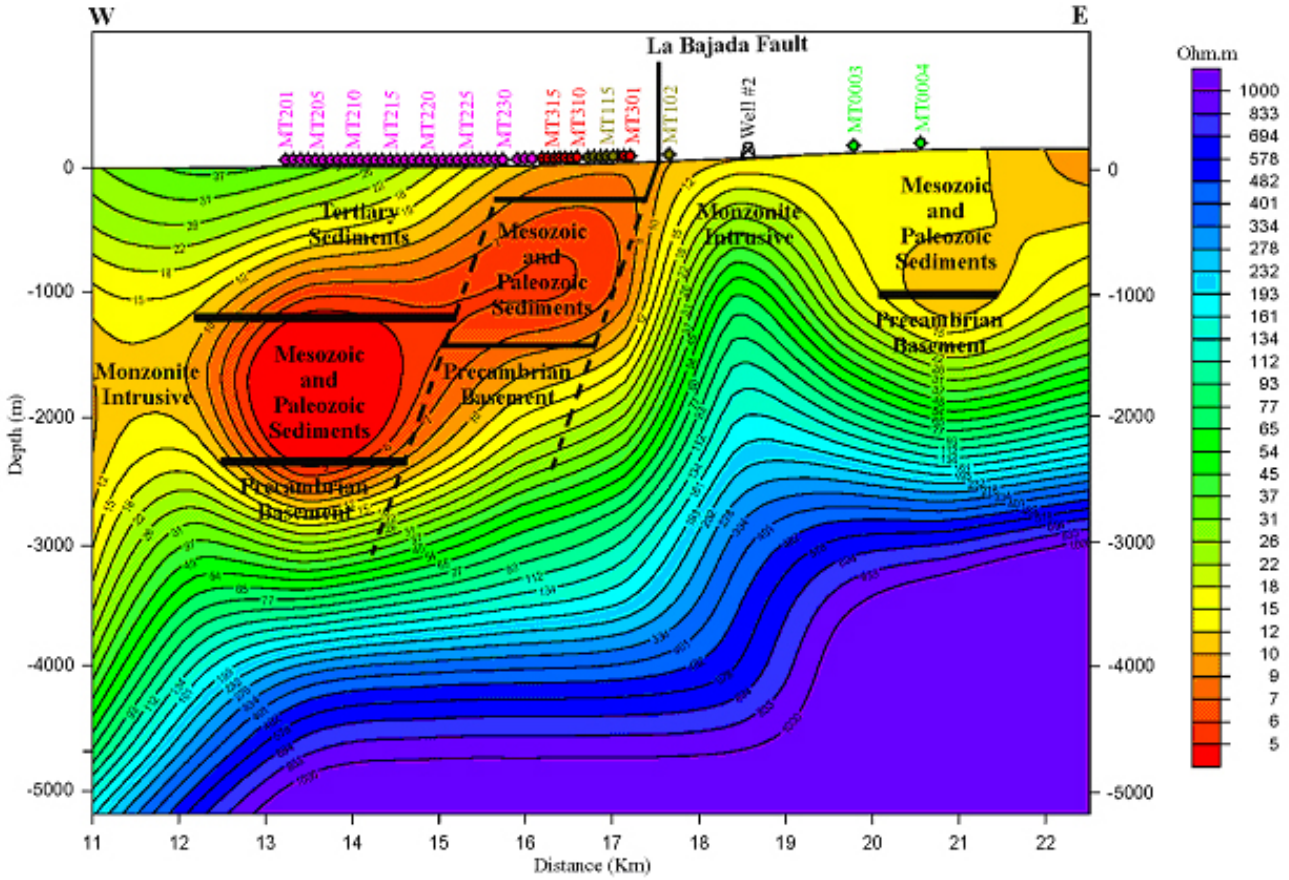

Figure 39. The smooth 2-D MT inversion results from Quesada (2004) with contours from a smoothing of the inversion grid. The offset seen in his Mesozoic and Paleozoic units is also represented in the present work. However, in the present work a slightly different structural interpretation is put forth.

Minor (2006) presented a more structurally complex model of the basin inferred from aeromagnetic and gravity data. The aeromagnetic data and gravity data were used to project several mapped fault traces into the basin (Figure 7). The geophysical model was presented along a profile with a bearing of N45W adjacent to SAGE MT survey (Figure 6). In the model Minor (2006) hypothesized a horst and graben structure that seems to match the 2-D inversion model (Figure 40). The USGS identified a La Majada graben section, the region between the Sanchez Fault and the La Bajada Fault, which agrees with the offset feature identified by Quesada (2004). The USGS La Bajada Fault dip angle, however, seems too shallow when compared to the results of the 2-D inversion model. The west dipping Cochiti fault is not as easily discernable in the 2-D inversion model due to larger distances between MT soundings between MT stations SDB-526 and SDB-501. Both MT soundings SDB-702 and SDB-704 are shallow noisy AMT sounding that are projected onto the survey from the Cochiti dam spillway, a region with slightly different near-surface geology (Figure 9). The region between the Cochiti and Sanchez Faults, the USGS Reservoir Horst block, appears lower than the La Majada graben from looking at the top of the highly conductive region 2, a detail not present in the Minor (2006) model (Figure 6).

In summary, several well log data sets were analyzed to help interpret three distinct regional features identified from the resistivity values and distinctive patterns of these regions within the smooth 2-D MT inversion model. A geologic stratigraphy is put forth to correlate geologic units within these regions. Region 1 is identified as late to middle Cenozoic basin-fill containing unsaturated to freshwater saturated sections. The highly conductive part of region 2 is identified as the Eocene Galiesteo Formation through Mesozoic section. The transitional part of region 2 is identified as Paleozoic Permian Yeso

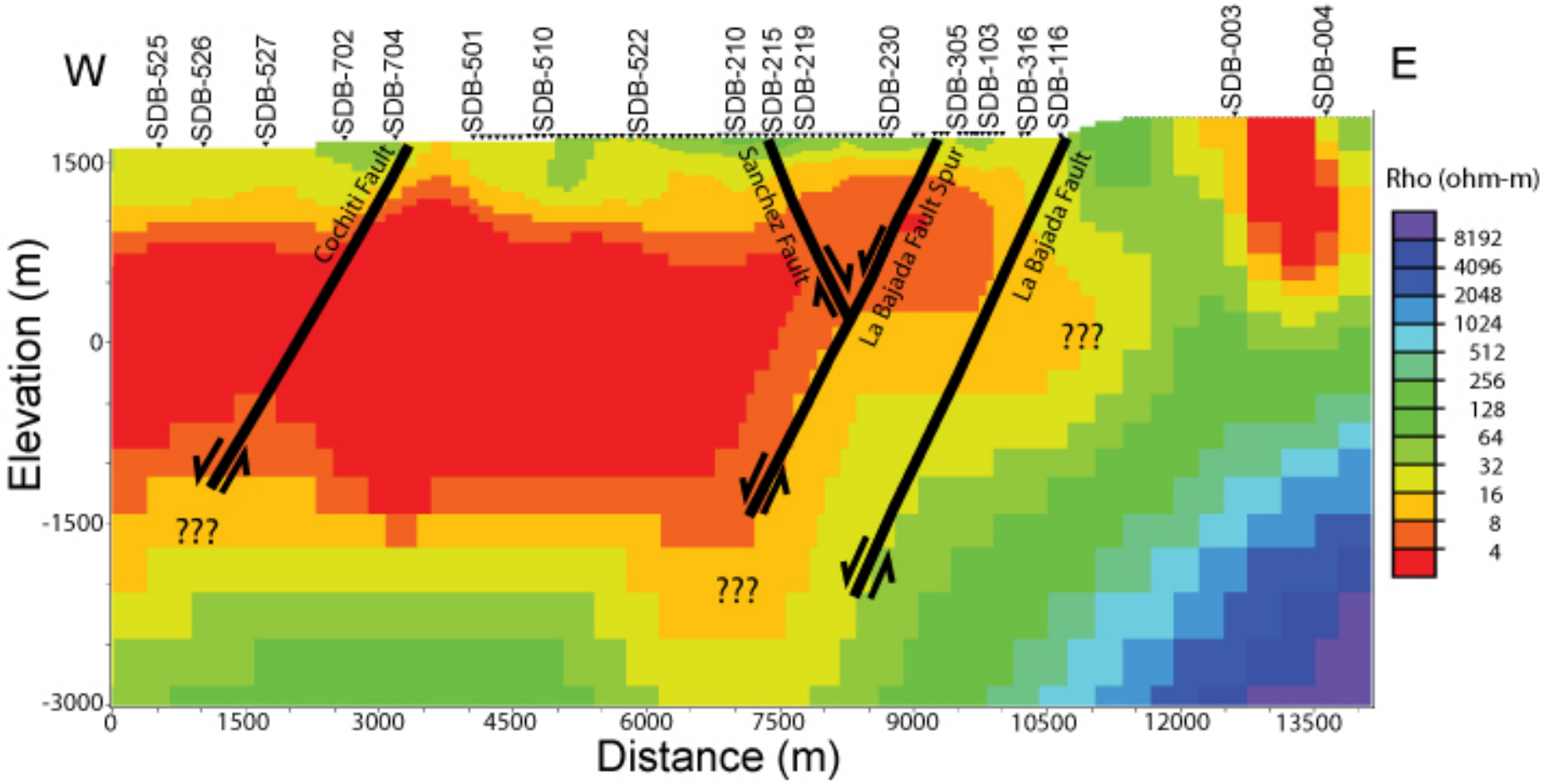

Figure 40. Geologic structural interpretation of the smooth 2-D MT inversion model. Faults were identified from extending USGS mapped faults at the surface to depth following resistivity contrasts presented in the smooth 2-D MT inversion model.

and Abo Formations. The highly resistive basement is identified with the early Paleozoic Pennsylvanian Madera rocks on top of Precambrian granitic basement. Geologic structural interpretations were based the work of Quesada (2004) and Minor (2006) with additional constraints and insight provided by the new, high quality MT data. The resulting new structural model suggest two grabens where the Resovior graben on the west has moved down in section with respect to the La Majada graben to the east. The complete interpreted geologic model is shown in Figure 41.

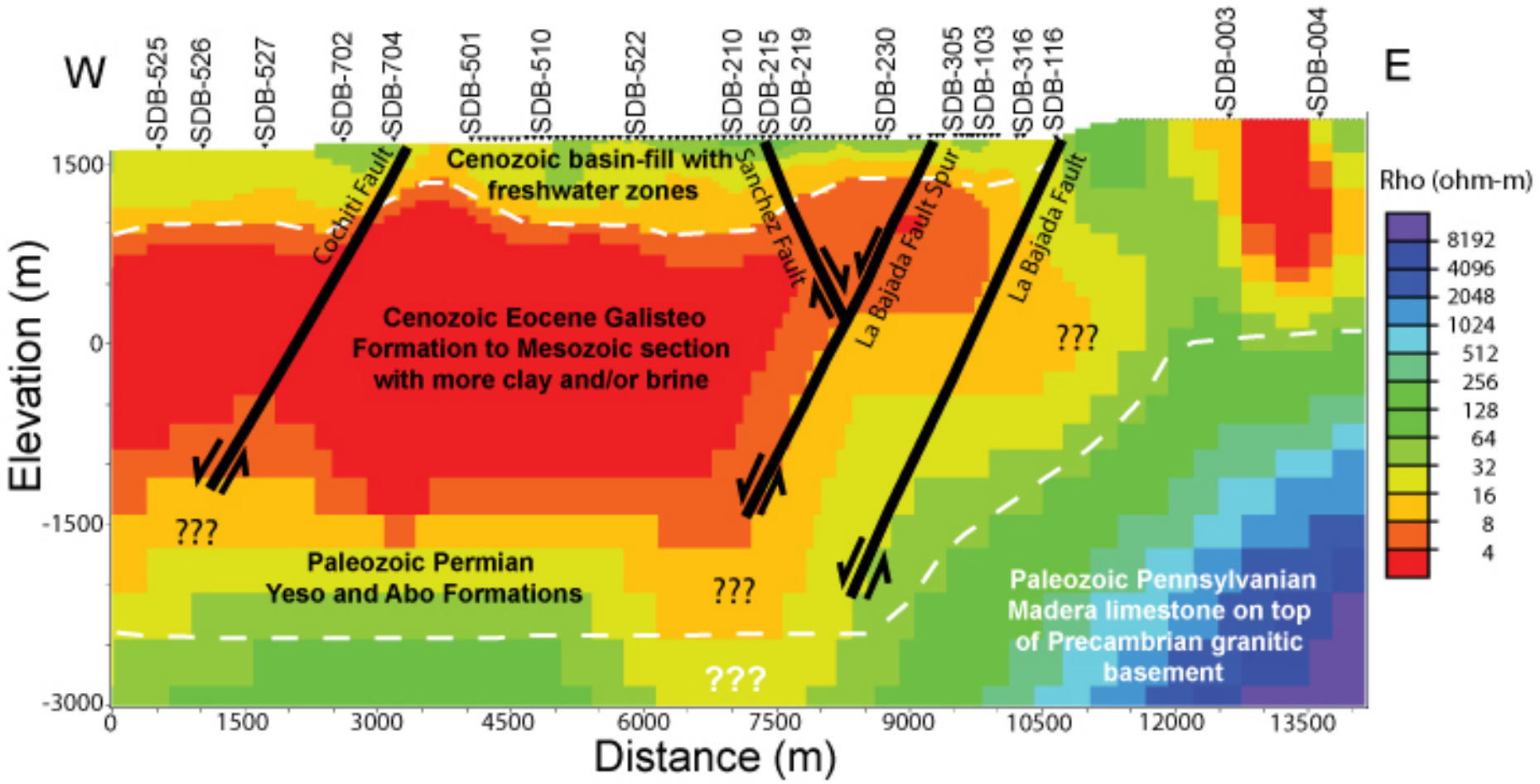

Figure 41. The combined geologic stratigraphic and structural interpreted smooth 2-D MT inversion model.

CHAPTER 5

CONCLUSIONS

From prior work in the Rio Grande rift and the Santo Domingo Basin, a complex tectonic history has emerged. Based on that work, SAGE has conducted geophysical measurements in the basin to extend what was presently known. From roughly 2000 to 2007, excluding the 2004 and 2006 years, SAGE has worked in and around the Santa Fe River and incised La Bajada fault escarpment on the Cochiti Pueblo. Data presented here include MT results along a 12 km-long profile line. The present work is a continuation of the study presented by Quesada (2004). The data have been carefully edited, rotated, and selected prior to smooth inversion using an algorithm in Geosystem's WinGLink software. Several different parameters were tested in the inversion process including the trade-off between a smoother resistivity model and a model with lesser misfit. Sensitivity tests were performed on questionable features within the model and some of these features were found to be not required by the data. A sensitivity map of the model indicated lower model sensitivity below an elevation of -3000 m resulting in the cropping of the model at -3000 m elevation.

Because the variations in the resistivities of common Earth materials overlap, resistivity values alone cannot be directly related to specific interpreted geologic units. However, three distinct regions within the 2-D inversion resistivity model were identified. Then borehole well logs from various wells were used to aid in the geologic interpretation of the three distinctive regions. In region 1 at the top of the model is a more resistive layer with resistivity values varying from 8 - 85 ohm-m and with a thickness varying from 350 - 800 m.

This region was interpreted to be a late to middle Cenozoic basin-fill. From data on water wells in the area this region contains both unsaturated and freshwater saturated sections. Beneath region 1 lies a thick, up to 3 km in places, conductive and transitional region 2 with resistivity values varying from 2 - 100 ohm-m interpreted to be early Cenozoic through late Paleozoic section. The upper, highly conductive, 2 - 8 ohm-m, section of region 2 is inferred to contain higher clay concentrations and/or brine. This part of region 2 has been identified as the Eocene Galisteo Formation and Mesozoic sections. The lower section of region 2 is a transitional zone where the bottom of the highly conductive, 8 ohm-m, upper section grades into a more resistive, 100 ohm-m, section at depth. This transitional part of region 2 has been interpreted to be late Paleozoic Permian Yeso and Abo Formations. Under lying regions 1 and 2 is a more resistive region 3. The upper part of region 3 with resistivity values varying from 100 - 1000 ohm-m has been interpreted to be the Paleozoic Pennsylvanian Madera limestone on top of Precambrian granitic basement.

Structural interpretations of these three regions agree with USGS extensions of several surface fault traces into the basin. Quesada (2004) identified a pair of parallel faults on the eastern end of the survey. Minor (2006) presented a more complex structural interpretation of the subsurface modeled from gravity and aeromagnetic data along a roughly parallel profile slightly offset to the north of the present work. The USGS model presents a horst and graben structure that is supported somewhat by the present work. The Minor (2006) model is slightly more oblique to the basin structure than the present work. A modified version of the USGS model is preferred where the area between the Cochiti and Sanchez Faults appears more like a down-dropped graben than a horst block.

Recommendations for future work include the collection of additional Titan MT soundings on both the western and eastern ends of the 2002 and 2005 Titan MT data as well as acquiring long period Spartan soundings at 1 km station spacing over the entire length of the survey. The new Titan and Spartan soundings should be collected along the same bearing of 107 degrees used in the 2002 and 2005 surveys. TEM measurements should continue to be collected at every second Titan sounding along the recommended extensions. Ideally the survey would extend across the entire width of the Santo Domingo Basin. Additional parallel profile lines 1 km to the north and south should be collected as well to check for lateral variations in the freshwater aquifer in region 1.

REFERENCES

Baldridge, W.S., F.V. Perry, D.T. Vaniman, L.D. Nealey, B.D. Leavy, A.W. Laughlin, P. Kyle, Y. Bartov, G. Steinitz, and E.S. Gladney, 1991, Middle to late Cenozoic magmatism of the southeastern Colorado Plateau and central Rio Grande rift, New Mexico and Arizona, U.S.A.: a model for continental rifting, *in* Gangi A.F. Ed., World rift systems: Tectonophysics, **197**, 327-354.

Baldridge, W.S., G.L. Cole, B.A. Robinson, and G.R. Jiracek, 2007, Application of time-domain airborne electromagnetic induction to hydrogeologic investigations on the Pajarito Plateau, New Mexico, USA: Geophysics, **72**, B31-B45.

Beamish, D., and J.M. Travassos, 1992, The use of the D+ solution in magnetotelluric interpretation: Journal of Applied Geophysics, **29**, 1-19.

Berdichevsky, M.N., and V.I. Dmitriev, 2002, Investigations in geophysics, Volume 11: Magnetotellurics in the context of the theory of ill-posed problems, G.V. Keller ed.: Soc. Expl. Geophy., 129-131.

Black, B.A., and W.L. Hiss, 1974, Structure and stratigraphy in the vicinity of the Shell Oil Co. Santa Fe Pacific No. 1 test well: New Mexico Geological Society 25th field conference, Ghost Ranch, Guidebook, 365-370.

Caldwell, T.G., H.M. Bibby and C. Brown, 2004, The magnetotelluric phase tensor: Geophys. J. Int., **158**, 457-469.

Gamble, T.D., W.M. Goubau, and J. Clark, 1979, Magnetotellurics with a remote magnetic reference: Geophysics, **44**, 53-68.

Geosystem SRL, 2008, A guide to using WinGLink Version 2.20.02.01: Geosystem SLR.

Grant, P.R., Jr., 1999, Subsurface geology and related hydrologic conditions, Santa Fe embayment and contiguous areas, New Mexico: New Mexico Geological, Guidebook, **50**, 425-435.

Jackson, J.D., 1998, Classical Electrodynamics, 3rd Ed: Wiley, 808.

Jiracek, G.R., C. Smith, and G.A. Dorn, 1976, Deep geothermal exploration in New Mexico using electrical resistivity: Proceedings of the second United Nations symposium on the development and use of geothermal resources, volume 2, 1095-1102.

Jiracek, G.R., V. Haak, and K.H. Olsen, 1995, Practical magnetotellurics in continental rift environments, *in* K.H. Olsen, ed., Continental rifts: evolution, structure, and tectonics, 103-129.

Keller, G.R., M.A. Khan, P. Morgan, R.F. Wendlandt, W.S. Baldridge, K.H. Olsen, C. Prodehl, and L.W. Braile, 1991, A comparative study of the Rio Grande and Kenya rifts: Tectonophysics, **197**, 355-371.

Manley, K., 1979, Stratigraphy and structure of the Espanola Basin, Rio Grande rift, New Mexico, *in* R.E. Riecker, Ed., Rio Grande rift: tectonics and magmatism: American Geophysical Union Special Publications, 71-86.

Minor, S.A., ed., 2006, The Cerrillos uplift, the La Bajada constriction, and hydrogeologic framework of the Santo Domingo Basin, Rio Grande rift, New Mexico: U.S. Geological Survey Professional Paper 1720, 189.

Oldenburg, D.W., and Y. Li, 2005, Inversion for applied geophysics: a tutorial, *in* Investigations in Geophysics Volume 13: Near-surface, D.K. Butler ed.: Soc. Expl. Geophy., 89-150.

Olsen, K.H., W.S. Baldridge, and J.F. Callender, 1987, Rio Grande rift: an overview: Tectonophysics, **143**, 119-139.

Palacky, G.J., 1988, Resistivity characteristics of geologic targets, *in* Investigations in Geophysics Volume 3: Electromagnetic methods in applied geophysics theory volume 1, M.N. Nabighian ed.: Soc. Expl. Geophys., 53–129.

Parker, R.L., 1980, The inverse problem of electromagnetic induction: Existence and construction of solutions based on incomplete data: J. Geophys. Res., **85**, 4421-4428.

Pellerin, L., and G.W. Hohmann, 1990, Transient electromagnetic inversion: A remedy for magnetotelluric static shifts: Geophysics, **55**, 1242-1250.

Quesada, R.M., 2004, Continuous Magnetotelluric Profiling across the La Bajada Fault, Rio Grande rift, New Mexico: San Diego State University Master Thesis.

Rodi, W., and R.L. Mackie, 2001, Nonlinear conjugate gradients algorithm for 2-D magnetotelluric inversion: Geophysics, **66**, 174-187.

Simpson, F., and K. Bahr, 2005, Practical Magnetotellurics: Cambridge University Press, 254.

Stearns, C.E., 1943, The Galisteo Formation of north-central New Mexico: Journal of Geology, **51**, 301-319.

Stearns, C.E., 1953a, Early Tertiary volcanism in the Galisteo-Tongue area, north-central New Mexico: American Journal of Science, **251**, 415-452.

Stearns, C.E., 1953b, Tertiary geology of the Galisteo-Tonque area, New Mexico: Geological Society of America, **64**, 459-508.

Vozoff, K., 1991, The magnetotelluric method *in* Investigations in Geophysics Volume 3: Electromagnetic methods in applied geophysics theory volume 2, M.N. Nabighian ed.: Soc. Expl. Geophys., 641–711.

Ward, S.H., and G.W. Hohmann, 1988, Electromagnetic theory for geophysical applications, *in* Investigations in Geophysics Volume 3: Electromagnetic methods in applied geophysics theory volume 1, M.N. Nabighian ed.: Soc. Expl. Geophys., 131–311.

APPENDIX A

MAGNETOTELLURIC SOURCES

The MT method involves measuring naturally occurring, time varying magnetic and electric fields at the Earth's surface. There are two main naturally occurring sources of these fields. One source is from lighting discharges around the world that produce electromagnetic waves with a frequency above about 1 Hz. The other source consists of the complex interactions between the solar wind (charged particles given off by the sun) and the Earth's magnetosphere and ionosphere which produce electromagnetic waves with a frequency below roughly 1 Hz. What follows are the essential equations relating the electromagnetic fields produced by these sources and their interaction with a homogeneous, nondispersive, isotropic, and linear Earth loosely following Berdichevsky and Dmitriev (2002), Jiracek (1995), and Ward and Hohmann (1988).

The behavior of electromagnetic (EM) fields can be concisely described through Maxwell's Equations. The two most pertinent equations are Faraday's Law and the Ampere-Maxwell Law. Faraday's Law in matter can be represented as

$$\nabla \times \mathbf{e} = -\mu \frac{\partial}{\partial t} \mathbf{h}\,, \qquad (A-1)$$

where $\mathbf{e} = \mathbf{e}(t, x, y, z)$ is the electrical field strength, μ is the magnetic permeability, and $\mathbf{h} = \mathbf{h}(t, x, y, z)$ is the magnetic field strength. The Ampere-Maxwell Law in matter can be represented as

$$\nabla \times \mathbf{h} = \varepsilon \frac{\partial}{\partial t} \mathbf{e} + \sigma \mathbf{e}\,, \qquad (A-2)$$

where ε is electrical permittivity or dielectric constant and σ is electrical conductivity. The first term on the right hand side of equation A-2 represents displacement current density and was Maxwell's contribution to Ampere's Law. The second term is conduction current

density. Assuming a charge free, homogeneous, nondispersive, isotropic (μ and ε are constant), and linear medium the two Maxwell equations can be combined to form the time domain propagating EM wave equations in a conductive medium represented by the following equations

$$\begin{aligned} \nabla^2\mathbf{e} - \mu\varepsilon\frac{\partial^2}{\partial t^2}\mathbf{e} - \mu\sigma\frac{\partial}{\partial t}\mathbf{e} = 0 \\ \nabla^2\mathbf{e} - \frac{1}{v^2}\frac{\partial^2}{\partial t^2}\mathbf{e} - \frac{1}{\kappa}\frac{\partial}{\partial t}\mathbf{e} = 0 \end{aligned} \qquad (A-3)$$

and

$$\begin{aligned} \nabla^2\mathbf{h} - \mu\varepsilon\frac{\partial^2}{\partial t^2}\mathbf{h} - \mu\sigma\frac{\partial}{\partial t}\mathbf{h} = 0 \\ \nabla^2\mathbf{h} - \frac{1}{v^2}\frac{\partial^2}{\partial t^2}\mathbf{h} - \frac{1}{\kappa}\frac{\partial}{\partial t}\mathbf{h} = 0 \end{aligned} . \qquad (A-4)$$

The second-order, time-derivative terms represent the wave or oscillating terms where the coefficients are $1/v^2$ where v is velocity of the propagating EM wave in the medium. The first-order, time-derivative terms represent damping terms where the coefficients represent $1/\kappa$ where κ is the diffusivity of the wave amplitude in the medium. From equations A – 3 and A – 4, the propagation of an EM wave in a conductive media is both a wave and a diffusion process (Berdichevsky and Dmitriev, 2002).

In MT theory several assumptions are made that simplify things. First, the magnetic permeability is taken to be that of a free space, $\mu = \mu_0 = 4\pi \times 10^{-7}$ H/m (henrys per meter). Second, in the low frequency range associated with MT measurements (Ward and Hohmann,

1988), the conduction currents dominate over the displacement currents, i.e. from the Ampere-Maxwell Law (equation A – 2)

$$\varepsilon \frac{\partial}{\partial t}\mathbf{e} < \sigma \mathbf{e}\,. \qquad (A-5)$$

This assumption has the effect of negating the Maxwell contribution to the Ampere-Maxwell Law and is known as the "quasi-static approximation" where the speed of the wave can be treated as instantaneous (Jackson, 1998). This also means that the Earth behaves as a good conductor (poor insulator) at the frequencies used in MT (Jiracek, 1995). As a result of the quasi-static approximation, the diffusive nature of propagating EM waves in a conductive medium dominates. The EM wave equations (equations A – 3 and A – 4) then reduce to

$$\nabla^2 \mathbf{e} - \mu_0 \sigma \frac{\partial}{\partial t}\mathbf{e} = 0 \qquad (A-6)$$

and

$$\nabla^2 \mathbf{h} - \mu_0 \sigma \frac{\partial}{\partial t}\mathbf{h} = 0\,. \qquad (A-7)$$

A third assumption made in MT theory is that the EM waves generated by the natural sources are planer in nature and normally incident to the Earth's surface. This means that the electric and magnetic fields are constant in direction and magnitude over planes perpendicular to the direction of propagation the z direction (Jiracek, 1995) and that the Laplacian terms can be replaced by the second partial derivatives with respect to z

$$\frac{\partial^2}{\partial z^2}\mathbf{e} - \mu_0 \sigma \frac{\partial}{\partial t}\mathbf{e} = 0 \qquad (A-8)$$

and

$$\frac{\partial^2}{\partial z^2}\mathbf{h} - \mu_0\sigma\frac{\partial}{\partial t}\mathbf{h} = 0\,. \qquad (A-9)$$

The time domain propagating electromagnetic wave equations (equations A – 3 and A – 4) can be Fourier transformed into the frequency domain using the following Fourier transforms

$$\mathbf{E}(\omega) = \int_{-\infty}^{+\infty} e(t)e^{-i\omega t}dt \qquad (A-10)$$

and

$$\mathbf{H}(\omega) = \int_{-\infty}^{+\infty} \mathbf{h}(t)e^{-i\omega t}dt\,, \qquad (A-11)$$

where i is the imaginary number and ω is the angular frequency equal to 2πf where f is frequency. The frequency domain propagating electromagnetic wave equations are represented by the following equations

$$\begin{aligned} &\nabla^2\mathbf{E} - (i\omega)^2\mu\varepsilon\mathbf{E} - (i\omega)\mu\sigma\mathbf{E} = 0 \\ &\nabla^2\mathbf{E} - [(i\omega)^2\mu\varepsilon + (i\omega)\mu\sigma]\mathbf{E} = 0 \\ &(\nabla^2 + k^2)\mathbf{E} = 0 \end{aligned} \qquad (A-12)$$

and

$$\begin{aligned} &\nabla^2\mathbf{H} - (i\omega)^2\mu\varepsilon\mathbf{H} - (i\omega)\mu\sigma\mathbf{H} = 0 \\ &\nabla^2\mathbf{H} - [(i\omega)^2\mu\varepsilon + (i\omega)\mu\sigma]\mathbf{H} = 0\,, \\ &(\nabla^2 + k^2)\mathbf{H} = 0 \end{aligned} \qquad (A-13)$$

where k is the complex wave number defined as

$$k^2 = -(i\omega)^2 \mu\varepsilon - (i\omega)\mu\sigma \,. \qquad \text{(A – 14)}$$

Equations A – 12 and A – 13 are known as the Helmholtz equations. This means that the time variation can be represented as $e^{i\omega t}$.

In the frequency domain the quasi-static assumption is normally represented by the inequality $\sigma > \omega\varepsilon$. The normally incident plane wave assumption again reduces the Laplacian terms to the second partial derivatives with respect to z and equations A – 12 and A – 13 then reduce to

$$\begin{aligned} \frac{\partial^2}{\partial z^2}\mathbf{E} - i\omega\mu_0\sigma\mathbf{E} &= 0 \\ \frac{\partial^2}{\partial z^2}\mathbf{E} + k^2\mathbf{E} &= 0 \end{aligned} \qquad \text{(A -15)}$$

and

$$\begin{aligned} \frac{\partial^2}{\partial z^2}\mathbf{H} - i\omega\mu_0\sigma\mathbf{H} &= 0 \\ \frac{\partial^2}{\partial z^2}\mathbf{H} + k^2\mathbf{H} &= 0 \end{aligned} \qquad \text{(A -16)}$$

where again magnetic permeability is taken to be that of a free space, $\mu = \mu_0$. The complex wave number equation (equation A – 14) then reduces to

$$k^2 = -i\omega\mu_0\sigma \,. \qquad \text{(A – 17)}$$

The complex wave number equation can be further simplified to

$$\begin{aligned} k &= \sqrt{-i}\sqrt{\omega\mu\sigma} \\ k &= \sqrt{\omega\mu\sigma}e^{-i\pi/4} \\ k &= \left(\frac{\omega\mu\sigma}{2}\right)^{1/2}(1-i) \\ k &= \mathrm{Re}\{k\} - i\,\mathrm{Im}\{k\} \end{aligned}, \qquad (A-18)$$

where Re{k} = Im{k}, for the quasi-static approximation. Equations A - 15 and A - 16 are already ordinary, second order-differential equations for the spatial dependence (z) where the solution bases are

$$\mathbf{E} = Ae^{ikz} + Be^{-ikz}. \qquad (A-19)$$

and

$$\mathbf{H} = Ce^{ikz} + De^{-ikz}. \qquad (A-20)$$

Now applying the boundary conditions which are

$$\begin{aligned} \mathbf{E}(0) &= \mathbf{E}_0 \\ \mathbf{E}(\infty) &= 0 \end{aligned} \qquad (A-21)$$

and

$$\begin{aligned} \mathbf{H}(0) &= \mathbf{H}_0 \\ \mathbf{H}(\infty) &= 0 \end{aligned} \qquad (A-22)$$

to the solutions are then

$$\mathbf{E}(z) = \mathbf{E}_0 e^{-ikz} \qquad (A-23)$$

and

$$\mathbf{H}(z) = \mathbf{H}_0 e^{-ikz}. \qquad (A-24)$$

The complex nature of the wave number, k, can be inserted into these solutions resulting in

$$\begin{aligned}\mathbf{E}(z) &= \mathbf{E}_0 e^{-i(\mathrm{Re}\{k\}-i\,\mathrm{Im}\{k\})z} \\ \mathbf{E}(z) &= \mathbf{E}_0 e^{-i\,\mathrm{Re}\{k\}z} e^{-\mathrm{Im}\{k\}z}\end{aligned} \qquad (A-25)$$

and

$$\begin{aligned}\mathbf{H}(z) &= \mathbf{H}_0 e^{-i(\mathrm{Re}\{k\}-i\,\mathrm{Im}\{k\})z} \\ \mathbf{H}(z) &= \mathbf{H}_0 e^{-i\,\mathrm{Re}\{k\}z} e^{-\mathrm{Im}\{k\}z}\end{aligned}. \qquad (A-26)$$

The term $e^{-\mathrm{Im}\{k\}z}$ represents attenuation because as z increases and since $\mathrm{Im}\{k\}$ is real the resulting amplitude decreases.

The distance at which the amplitude of the EM wave in the medium is reduce to e^{-1} holds a special meaning and is known as the skin depth, δ. This is represented by

$$\begin{aligned}e^{-\mathrm{Im}\{k\}z} &= e^{-1} \\ \mathrm{Im}\{k\}z &= 1 \\ z &= \frac{1}{\mathrm{Im}\{k\}} \\ z &= \left(\frac{2}{\omega\mu_0\sigma}\right)^{1/2} \\ \delta &\approx 503\sqrt{\rho T}\end{aligned} \qquad (A-27)$$

in m, where $\omega = 2\pi / T$, $\sigma = 1 / \rho$, and $\mu_0 = 4\pi \times 10^{-7}$ H/m. T is the wave period and ρ is the electrical resistivity. The skin depth can be used to determine the wavelength, λ,

$$\lambda = 2\pi\delta. \qquad (A-28)$$

The wave velocity, v, can be calculated

$$\begin{aligned}v &= \frac{\lambda}{T} \\ v &= \omega\delta\end{aligned}. \qquad (A-29)$$

These simple relationships for δ, λ, and v where derived again for the homogeneous, nondispersive, isotropic Earth, under the quasi-static assumption. The real Earth is never so simple (Jiracek, 1995).

APPENDIX B

MT DATA PROCESSING

In the Quantec processing routine the processor first inspects and corrects the time series data for tares, time offsets, and polarity problems with the signals. "Events" are built with the remote reference data corresponding to the same absolute time, sampling rate, and record length as the survey line sounding data. Remote reference processing is effective in reducing incoherent noise between two simultaneous MT recordings (Gamble et al., 1979). In the processing code the electric field, **e**(t), and magnetic field, **h**(t), time series data are Fourier transformed using the following equations

$$\mathbf{E}(\omega) = \int_{-\infty}^{+\infty} \mathbf{e}(t) e^{-i\omega t} dt \qquad \text{(B – 1)}$$

and

$$\mathbf{H}(\omega) = \int_{-\infty}^{+\infty} \mathbf{h}(t) e^{-i\omega t} dt \qquad \text{(B – 2)}$$

into the frequency, ω (angular frequency), domain. The frequency domain data are then "notch" filtered to remove the common electrical power line frequency, 60 Hz or 50 Hz. In a 1-D resistivity Earth model, ρ(z), the electrical fields, **E**(ω), and the magnetic fields, **H**(ω), in the frequency domain are related to each other through the following transfer functions:

$$\mathbf{E}_x(\omega) = \mathbf{Z}(\omega)\mathbf{H}_y(\omega) \qquad \text{(B – 3)}$$

and

$$\mathbf{E}_y(\omega) = -\mathbf{Z}(\omega)\mathbf{H}_x(\omega)\,, \qquad \text{(B – 4)}$$

where **Z**(ω) is the transfer function or impedance. For the multi-dimensional case where **E**(ω) and **H**(ω) fields are no longer required to be orthogonal, they are related to each other through the following transfer functions:

$$\mathbf{E}_x(\omega) = \mathbf{Z}_{xx}(\omega)\mathbf{H}_x(\omega) + \mathbf{Z}_{xy}(\omega)\mathbf{H}_y(\omega) \qquad \text{(B – 5)}$$

and

$$\mathbf{E}_y(\omega) = \mathbf{Z}_{yx}(\omega)\mathbf{H}_x(\omega) + \mathbf{Z}_{yy}(\omega)\mathbf{H}_y(\omega) \tag{B - 6}$$

which can be restated in the magnetotelluric tensor equation

$$\begin{bmatrix} \mathbf{E}_x \\ \mathbf{E}_y \end{bmatrix} = \begin{bmatrix} \mathbf{Z}_{xx} & \mathbf{Z}_{xy} \\ \mathbf{Z}_{yx} & \mathbf{Z}_{yy} \end{bmatrix} \begin{bmatrix} \mathbf{H}_x \\ \mathbf{H}_y \end{bmatrix}. \tag{B - 7}$$

Equations B -5 and B – 6 can be viewed as two inputs, $\mathbf{H}_i(\omega)$ and $\mathbf{H}_j(\omega)$, into two transfer functions with the result being a single output, $\mathbf{E}_i(\omega)$ and can be solved using the techniques used to solve a bivariate linear regression problem (Simpson and Bahr, 2005). The impedance elements are isolated by utilizing least-squares estimates for the band-averaged auto-power density and the cross-power density. Prior to the band averaging, auto and cross-power estimates from N MT time series records are ensemble averaged. Since any noise present in the auto-power calculation and correlated noise in the cross-power calculation is amplified by these estimates, the method of remote referencing was established where a second set of **H**-field measurements are substituted in for the survey site measurements (Gamble et al., 1979). This method assumes that the noise in the **H** fields at the survey site and remote site are uncorrelated while the signals in **H** fields at the two sites are correlated. Therefore, through destructive interference the noise is minimized. A bracket notation is introduced as a way simplifying the equations where an example for an auto-power density is

$$\left\langle \mathbf{A}\mathbf{A}^* \right\rangle = \sum_{j=1}^{N} \left(\mathbf{A}_j \mathbf{A}_j^* \right) \tag{B – 8}$$

and an example for a cross-power density

$$\left\langle \mathbf{A}\mathbf{B}^* \right\rangle = \sum_{j=1}^{N} \left(\mathbf{A}_j \mathbf{B}_j^* \right) \tag{B – 9}$$

where the superscript ***** indicates complex conjugate. The MT transfer functions/impedance elements are then computed using the following equations

$$\mathbf{Z}_{xx} = \frac{\left\langle \mathbf{E}_x \mathbf{H}^*_{xr} \right\rangle \left\langle \mathbf{H}_y \mathbf{H}^*_{yr} \right\rangle - \left\langle \mathbf{E}_x \mathbf{H}^*_{yr} \right\rangle \left\langle \mathbf{H}_y \mathbf{H}^*_{xr} \right\rangle}{\left\langle \mathbf{H}_x \mathbf{H}^*_{xr} \right\rangle \left\langle \mathbf{H}_y \mathbf{H}^*_{yr} \right\rangle - \left\langle \mathbf{H}_x \mathbf{H}^*_{yr} \right\rangle \left\langle \mathbf{H}_y \mathbf{H}^*_{xr} \right\rangle} \qquad \text{(B – 10)}$$

$$\mathbf{Z}_{xy} = \frac{\left\langle \mathbf{E}_x \mathbf{H}^*_{yr} \right\rangle \left\langle \mathbf{H}_x \mathbf{H}^*_{xr} \right\rangle - \left\langle \mathbf{E}_x \mathbf{H}^*_{xr} \right\rangle \left\langle \mathbf{H}_x \mathbf{H}^*_{yr} \right\rangle}{\left\langle \mathbf{H}_x \mathbf{H}^*_{xr} \right\rangle \left\langle \mathbf{H}_y \mathbf{H}^*_{yr} \right\rangle - \left\langle \mathbf{H}_x \mathbf{H}^*_{yr} \right\rangle \left\langle \mathbf{H}_y \mathbf{H}^*_{xr} \right\rangle} \qquad \text{(B – 11)}$$

$$\mathbf{Z}_{yx} = \frac{\left\langle \mathbf{E}_y \mathbf{H}^*_{xr} \right\rangle \left\langle \mathbf{H}_y \mathbf{H}^*_{yr} \right\rangle - \left\langle \mathbf{E}_y \mathbf{H}^*_{yr} \right\rangle \left\langle \mathbf{H}_y \mathbf{H}^*_{xr} \right\rangle}{\left\langle \mathbf{H}_x \mathbf{H}^*_{xr} \right\rangle \left\langle \mathbf{H}_y \mathbf{H}^*_{yr} \right\rangle - \left\langle \mathbf{H}_x \mathbf{H}^*_{yr} \right\rangle \left\langle \mathbf{H}_y \mathbf{H}^*_{xr} \right\rangle} \qquad \text{(B – 12)}$$

and

$$\mathbf{Z}_{yy} = \frac{\left\langle \mathbf{E}_y \mathbf{H}^*_{yr} \right\rangle \left\langle \mathbf{H}_x \mathbf{H}^*_{xr} \right\rangle - \left\langle \mathbf{E}_y \mathbf{H}^*_{xr} \right\rangle \left\langle \mathbf{H}_x \mathbf{H}^*_{yr} \right\rangle}{\left\langle \mathbf{H}_x \mathbf{H}^*_{xr} \right\rangle \left\langle \mathbf{H}_y \mathbf{H}^*_{yr} \right\rangle - \left\langle \mathbf{H}_x \mathbf{H}^*_{yr} \right\rangle \left\langle \mathbf{H}_y \mathbf{H}^*_{xr} \right\rangle} \qquad \text{(B – 13)}$$

where the subscript r on select **H**-field terms indicates the remote reference value. The final result of the MT processing step is the output of a SEG (Society of Exploration Geophysicists) standardized data file called an ".edi file" which contains complex values for the impedance elements.

APPENDIX C

DIMENSIONALITY, POLAR DIAGRAMS, AND PHASE TENSOR PLOTS

The subsurface resistivity distribution can be classified into three general cases: 1-D, 2-D, and 3-D Earth models. In the simplest 1-D case, $\rho(z)$, the resistivity distribution consists of homogenous, isotropic layers where the boundaries are strictly horizontal. In the 2-D case, $\rho(x, z)$, the resistivity distribution is inhomogeneous and/or anisotropic but invariant in the y direction where the boundaries are confined to the y direction and are arbitrary long. In the 3-D case, $\rho(x, y, z)$, the resistivity distribution is inhomogeneous and can be anisotropic where the boundaries are completely arbitrary.

In the 2-D case there is a geoelectric strike direction associated with a lateral boundary where electric charges can build-up on the surfaces between different resistivity distributions, Figure 42. The normal components of current density, J_n, must be continuous across an interface, $\mathbf{J}_{n1} = \mathbf{J}_{n2}$, in cases wherein displacement currents are neglected (Ward and Hohmann, 1988 and Appendix A). From Ohm's law, $\mathbf{J} = \sigma \mathbf{E}$, where σ is conductivity it follows that $\sigma_1\mathbf{E}_{n1} = \sigma_2\mathbf{E}_{n2}$. If $\mathbf{J}_n$ is continuous and the conductivity on each side of the interface is different, $\sigma_1 \neq \sigma_2$, then the E_n must be discontinuous such that $\mathbf{E}_{n1} / \mathbf{E}_{n2} = \sigma_2 / \sigma_1$. Differences in the total, normal electrical field strengths across boundaries are due to secondary electric fields that are setup in response to the electrical charge build up along boundaries. The result is that the total electrical field strength on the more conductive side is reduced while the total electric field strength on the more resistive side is increased. This is illustrated in Figure 42 through the vector addition of the primary electric fields (E_x) and the secondary fields (E_s).

Two graphical methods used to investigate the dimensionality of MT data are polar diagrams and phase tensor plots. The two methods are illustrated in Figure 43 for a 1-D, a

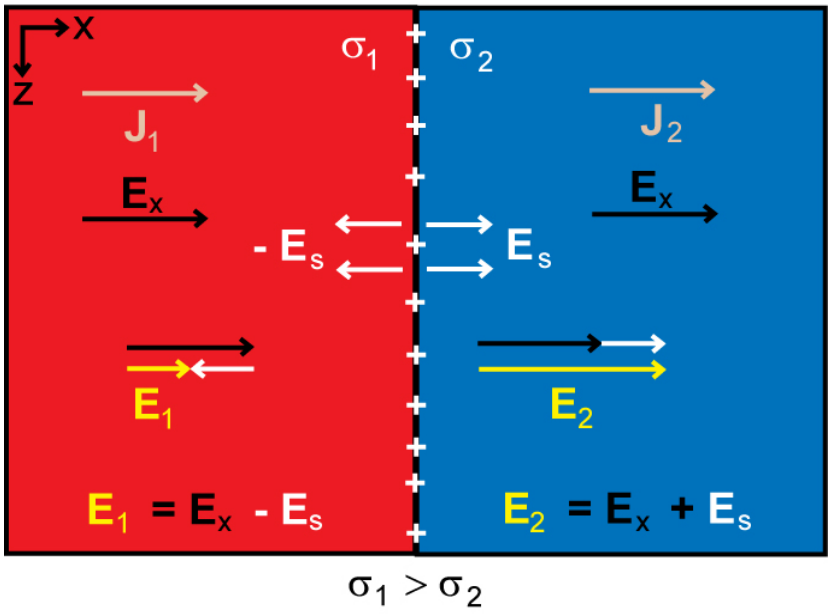

Figure 42. A schematic representation of a 2-D vertical boundary condition. Charges build up along the boundary resulting in a secondary electric field that opposes the applied electric field on the conductive side while adding to the applied electric field on the more resistive side (modified from Vozoff, 1991).

2-D, and two different 3-D idealistic cases (see also Appendix D for additional information). The first method is the standard polar diagram which consists of two figures as displayed in the top two rows and is usually displayed as a superposition of both figures. Polar diagrams are plots of the magnitude values of various impedance elements (equations B-10 to B-13) traced out in cardinal directions as the impedance tensor is rotated through an angle (Figure 44) varying from 0 to 2π (0 is usually taken to be true north),

$$\mathbf{Z}' = \mathbf{R}\mathbf{Z}\mathbf{R}^{T} \qquad (C-1)$$

where

$$\mathbf{Z} = \begin{bmatrix} \mathbf{Z}_{xx} & \mathbf{Z}_{xy} \\ \mathbf{Z}_{yx} & \mathbf{Z}_{yy} \end{bmatrix} \qquad (C-2)$$

and

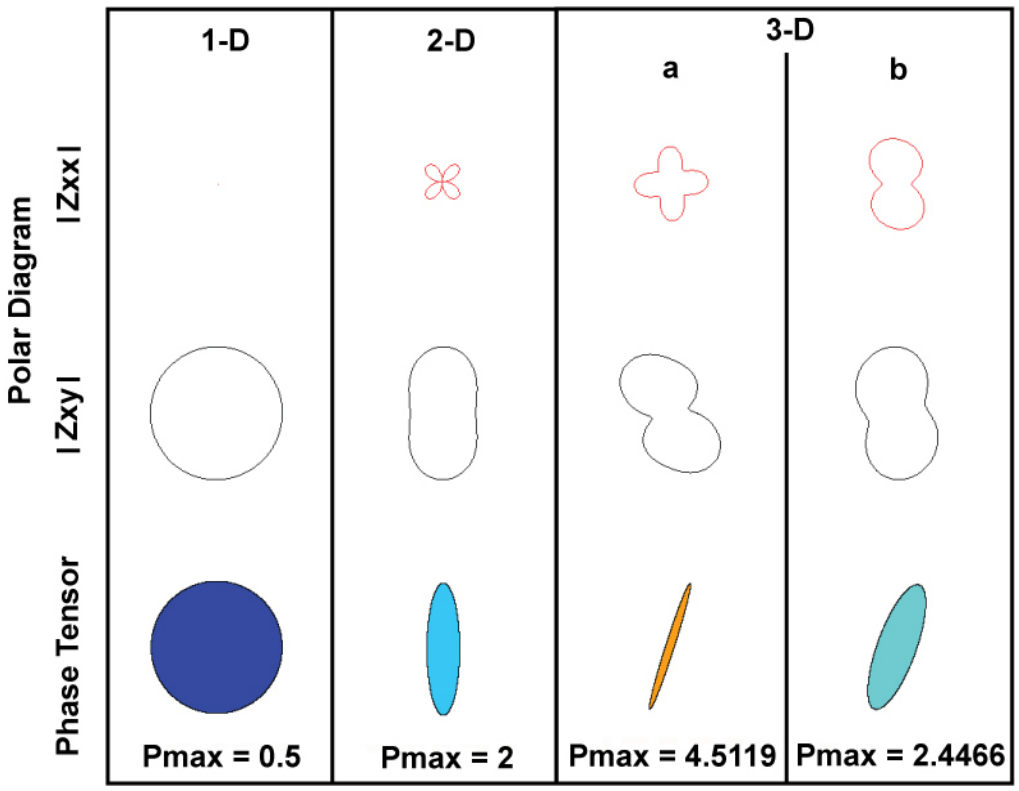

Figure 43. Polar diagrams and phase tensor plots for 1-D, 2-D, and two 3-D impedance tensors. The top two rows display the two polar diagram curves while the bottom row displays the phase tensor plots. In the phase tensor plots both the fill color and Pmax value indicate the maximum phase value used to normalize the plots. The appearance of polar diagram and phase tensor plots for the 1-D and 2-D cases are similar with identical principal directions while in the 3-D case there are significant differences (modified from Berdichevsky and Dmitriev, 2002).

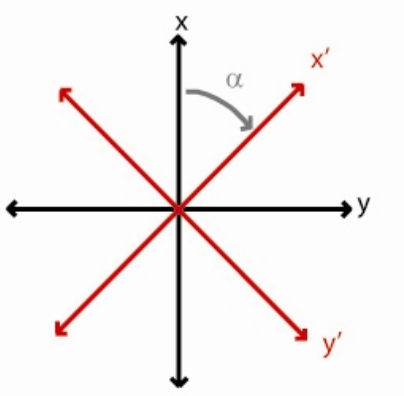

Figure 44. The rotational reference frame for rotating the impedance tensor. The rotation angle, α, is measured from the vertical (normally representing true north) in the clockwise direction.

$$\mathbf{R} = \begin{bmatrix} \cos\alpha & \sin\alpha \\ -\sin\alpha & \cos\alpha \end{bmatrix}. \qquad (C-3)$$

Traced out in the top row (Figure 43) are examples of the magnitude of $\mathbf{Z}_{xx}$, a diagonal element of the of the impedance tensor (equation B-10). The second row (Figure 43) traces out the magnitude of $\mathbf{Z}_{xy}$, an off diagonal element of the impedance tensor (equation B-11). Maxima and minima in the polar diagrams provide insight into the dimensionality of the MT sounding and the selection of impedance rotation directions corresponding to the TE and TM modes in 2-D Earth models.

For example, the off diagonal impedance tensor element ($\mathbf{Z}_{xy}$) polar diagram can vary from a circle in 1-D cases to a quasi-elliptical shape to a peanut shape (ovals of Cassini) in 2-D and 3-D cases. In the 1-D case, the $\mathbf{Z}_{xy}$ diagram is independent of the rotation angle and therefore, a circle because the magnitude of $\mathbf{Z}_{xy}$ is a constant value with all rotation directions. In the 1-D case, the magnitude of $\mathbf{Z}_{xx}$ is a constant value equal to zero therefore, it plots as a point in the polar diagram (Figure 43).

In 2-D, polar diagrams are quasi-elliptical shaped indicating that the magnitude of the impedance tensor ($\mathbf{Z}_{xy}$) has a minimum and a maximum value**.** These values are related to unique impedance rotation angles, called principal directions, that are parallel and perpendicular to geoelectric strike in 2-D subsurface resistivity distributions. The $\mathbf{Z}_{xx}$ "four-leaf" curve has zero values for the same unique angles that produce the maximum and minimum values in the $\mathbf{Z}_{xy}$ curve. At these principal directions the diagonal impedance elements are zero and the off diagonal impedance elements can be represented by the magnitudes of the TE and TM mode ratios of the electric field over the magnetic field

$$\begin{bmatrix} \mathbf{E}_x \\ \mathbf{E}_y \end{bmatrix} = \begin{bmatrix} 0 & \mathbf{Z}_{xy} \\ \mathbf{Z}_{yx} & 0 \end{bmatrix} \begin{bmatrix} \mathbf{H}_x \\ \mathbf{H}_y \end{bmatrix}. \qquad (C-4)$$

The reason for the principal directions stems directly from the boundary conditions associated with a 2-D resistivity distribution. This means that the two unique MT polarizations, based on the electrical field being normal and parallel to the vertical boundary, associated with the 2-D boundary condition can be directly related to the 2-D impedance elements. Figure 45 illustrates how a 2-D vertical boundary between a more conductive resistivity distribution and a more resistive resistivity distribution can affect the shape of polar diagrams. These differences are clearly visible in the magnitude of the impedance vectors normal to the boundary, corresponding to the TM mode impedance. The magnitudes are smaller on the conductive side and larger on the resistive side because the electrical field is discontinuous across the boundary with a larger resultant electric field on the more

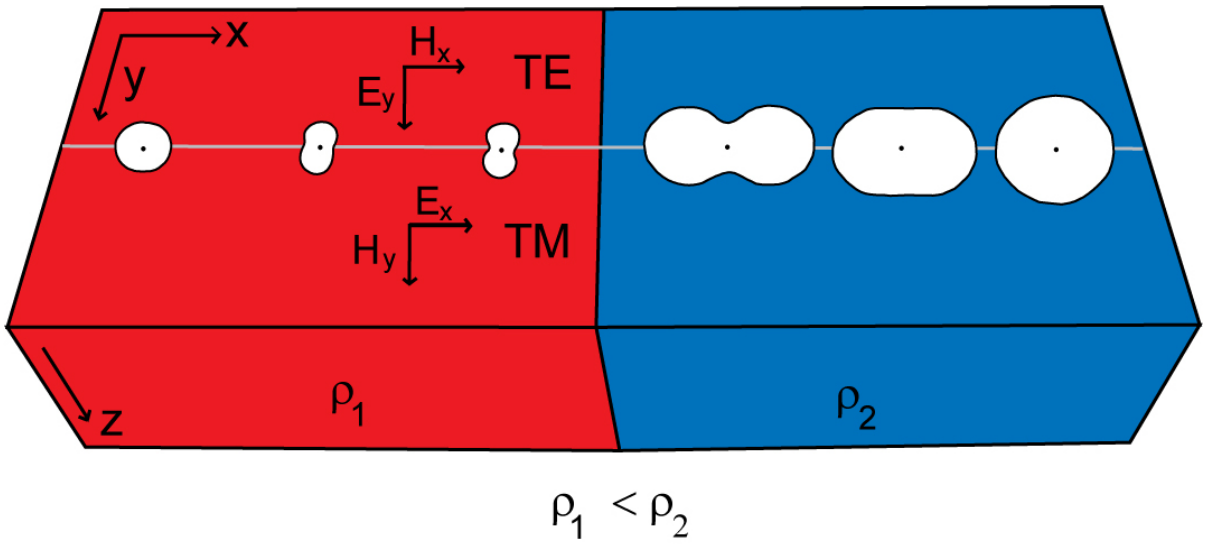

Figure 45. A 2-D resistivity distribution resulting from a vertical boundary condition illustrating the effects on the polar diagrams. The block on the left is more conductive then the more resistive block on the right. The electromagnetic polarizations/MT modes are labeled. (modified from Vozoff, 1991)

resistive side (Figure 42). The magnetic fields, parallel and normal to the boundary, are both continuous across boundaries if the magnetic permeability does not change (Ward and Hohmann ,1988). The magnitudes of the impedance vectors parallel to the boundary, the TE mode impedance, are the same length on either side of the boundary at the boundary because both the electric and magnetic fields are continuous across the boundary.

In 3-D polar diagrams (Figure 43) the $\mathbf{Z}_{xy}$ and $\mathbf{Z}_{xx}$ curves do not exhibit the same relations as in 2-D cases. The subsurface resistivity distribution is more complex, i.e. $\rho(x,y,z)$ and for example the magnitude of diagonal impedance element, $\mathbf{Z_{xx}}$, does not go to zero for any rotation angle. The concept of TE and TM polarizations/modes is not applicable here since it is strictly defined 2-D resistivity distributions only. The implications are that it is not appropriate to use 2-D inversion method here, a full 3-D inversion method is required.

The second, newer method of MT dimensional analysis are phase tensor plots which consists of ellipses and a tensor invariant values that is used to shade in the ellipses (third row of Figure 43). The phase tensor extends the concept of the phase of a complex vector defined as the ratio of its imaginary and real vectors, i.e. the impedance phase, to a complex matrix or tensor, defined as the ratio of its imaginary and real matrices. The phase tensor is formed by

$$\mathbf{\Phi} = \mathrm{Re}\{\mathbf{Z}\}^{-1}\,\mathrm{Im}\{\mathbf{Z}\} \qquad (C-5)$$

where $\mathbf{Z}$ is the impedance tensor (Equation C - 2) (Caldwell et al., 2004). The phase tensor plot is then constructed by

$$\begin{bmatrix} \mathbf{\Phi}_{11} & \mathbf{\Phi}_{12} \\ \mathbf{\Phi}_{21} & \mathbf{\Phi}_{22} \end{bmatrix} \begin{bmatrix} \cos\alpha \\ \sin\alpha \end{bmatrix} = \begin{bmatrix} x \\ y \end{bmatrix} \qquad (C-6)$$

which is a mapping of one vector into another (Caldwell et al., 2004). As α is allowed to vary from 0 to 2π, the vector $[\cos\alpha \ \ \sin\alpha]^{T}$ represents a set of unit vectors that trace out a unit circle. These vectors are then transformed by the phase tensor and the resultant is plotted. This explains why the plots can only be circles or ellipses with varying degrees of eccentricity. Two invariants that are sometimes used to shade in the ellipse are the maximum and minimum phase values. The choice of the invariant is arbitrary, but the choice should display the greatest variety in the data. The maximum phase value is sometimes used to normalize the plot so displaying this invariant will allow for quick visual representation of the amount of normalization applied to the plot. An advantage for using the phase tensor plots over the polar diagrams is that the phase tensor is insensitive to galvanic distortion that cause static shifts (parallel shifts in MT apparent resistivity curves due to electrical charge build-up as illustrated in Figure 42 in near-surface, small scale, inhomogeneities) (Caldwell et al., 2004).

Like the polar diagrams the phase tensor plot can also be used to identify the dimensionality of the resistivity distribution. Even though the phase tensor plots are derived differently than the polar diagrams, they both yield a circle in 1-D Earth models and the identical principal directions in 2-D Earth models. The polar diagrams and phase tensor plots for 3-D resistivity distributions do not contain the same information because the former are affected by galvanic distortions. Caldwell et al. (2004) showed that the phase tensor is independent of galvanic distortion and provides the direction of maximum inductive response, which is the closest equivalent to the strike direction in 3-D. This information can not be obtained from polar diagrams.

APPENDIX D

MORE ON POLAR DIAGRAMS AND PHASE TENSOR PLOTS

What follows is the essential equations used to construct Figure 43. The polar diagram portion of the figure is a reproduction from Berdichevsky and Dmitriev (2002) where the impedance tensors for the different dimensional cases are as follows, for the 1-D case

$$\mathbf{Z} = \begin{bmatrix} 0.0 + 0.0i & 4.0 - 2.0i \\ -4.0 + 2.0i & 0.0 + 0.0i \end{bmatrix}, \tag{D - 1}$$

for the 2-D case

$$\mathbf{Z} = \begin{bmatrix} 0.0 + 0.0i & 4.0 - 2.0i \\ -1.0 + 2.0i & 0.0 + 0.0i \end{bmatrix}, \tag{D – 2}$$

for the 3-D case a

$$\mathbf{Z} = \begin{bmatrix} -0.5 - 3.0i & 4.0 - 2.0i \\ -1.0 + 2.0i & 0.5 + 3.0i \end{bmatrix}, \tag{D – 3}$$

and for the 3-D case b

$$\mathbf{Z} = \begin{bmatrix} -0.5 - 3.0i & 4.0 - 2.0i \\ -1.0 + 2.0i & 0.1 - 1.0i \end{bmatrix} \tag{D – 4}$$

(Berdichevsky and Dmitriev, 2002).

In polar diagrams, the components of the impedance tensor are rotated through an angle of α in the following equations:

$$[\mathbf{Z}(\alpha)] = [\mathbf{R}(\alpha)][\mathbf{Z}][\mathbf{R}(-\alpha)] \tag{D – 5}$$

where

$$[\mathbf{R}(\alpha)] = \begin{bmatrix} \cos\alpha & \sin\alpha \\ -\sin\alpha & \cos\alpha \end{bmatrix}, \tag{D – 6}$$

(Berdichevsky and Dmitriev, 2002). The equation for $\mathbf{Z}_{xx}$ polar diagrams is

$$|\mathbf{Z}_{xx}(\alpha)| = \left(|\mathbf{Z}_2|^2 + |\mathbf{Z}_3|^2 \sin^2 2\alpha + |\mathbf{Z}_4| \cos^2 + 2\,\mathrm{Re}\left(\mathbf{Z}_2 \mathbf{Z}_3^*\right) \sin 2\alpha \right.$$

$$+ 2\,\mathrm{Re}\left(\mathbf{Z}_2\mathbf{Z}_4^*\right)\cos 2\alpha + \mathrm{Re}\left(\mathbf{Z}_3\mathbf{Z}_4^*\right)\sin 4\alpha\Big)^{\frac{1}{2}} \qquad \text{(D – 7)}$$

and the equation for $\mathbf{Z}_{xy}$ polar diagrams is

$$\left|\mathbf{Z}_{xy}(\alpha)\right| = \Big(\left|\mathbf{Z}_1\right|^2 + \left|\mathbf{Z}_3\right|^2\cos^2 2\alpha + \left|\mathbf{Z}_4\right|\sin^2 + 2\,\mathrm{Re}\left(\mathbf{Z}_1\mathbf{Z}_3^*\right)\cos 2\alpha$$

$$- 2\,\mathrm{Re}\left(\mathbf{Z}_1\mathbf{Z}_4^*\right)\sin 2\alpha - \mathrm{Re}\left(\mathbf{Z}_3\mathbf{Z}_4^*\right)\sin 4\alpha\Big)^{\frac{1}{2}} \qquad \text{(D – 8)}$$

where

$$\mathbf{Z}_1 = \frac{1}{2}\left(\mathbf{Z}_{xy} - \mathbf{Z}_{yx}\right) \qquad \text{(D – 9)}$$

$$\mathbf{Z}_2 = \frac{1}{2}\left(\mathbf{Z}_{xx} + \mathbf{Z}_{yy}\right) \qquad \text{(D – 10)}$$

$$\mathbf{Z}_3 = \frac{1}{2}\left(\mathbf{Z}_{xy} + \mathbf{Z}_{yx}\right) \qquad \text{(D – 11)}$$

and

$$\mathbf{Z}_4 = \frac{1}{2}\left(\mathbf{Z}_{xx} - \mathbf{Z}_{yy}\right) \qquad \text{(D – 12)}$$

(Berdichevsky and Dmitriev, 2002).

The phase tensor is formed from the real and imaginary components of the impedance tensor in the following equation

$$\begin{bmatrix}\mathbf{\Phi}_{11} & \mathbf{\Phi}_{12}\\ \mathbf{\Phi}_{21} & \mathbf{\Phi}_{22}\end{bmatrix} = \frac{1}{\det(\mathrm{Re}(\mathbf{Z}))}\begin{bmatrix}\mathrm{Re}(\mathbf{Z}_{yy})\,\mathrm{Im}(\mathbf{Z}_{xx}) - \mathrm{Re}(\mathbf{Z}_{xy})\,\mathrm{Im}\left(\mathbf{Z}_{yx}\right) & \mathrm{Re}(\mathbf{Z}_{yy})\,\mathrm{Im}(\mathbf{Z}_{xy}) - \mathrm{Re}(\mathbf{Z}_{xy})\,\mathrm{Im}\left(\mathbf{Z}_{yy}\right)\\ \mathrm{Re}(\mathbf{Z}_{xx})\,\mathrm{Im}(\mathbf{Z}_{yx}) - \mathrm{Re}(\mathbf{Z}_{yx})\,\mathrm{Im}\left(\mathbf{Z}_{xx}\right) & \mathrm{Re}(\mathbf{Z}_{xx})\,\mathrm{Im}(\mathbf{Z}_{yy}) - \mathrm{Re}(\mathbf{Z}_{yx})\,\mathrm{Im}\left(\mathbf{Z}_{xy}\right)\end{bmatrix} \qquad \text{(D – 13)}$$

where

$$\det(\mathrm{Re}(\mathbf{Z})) = \mathrm{Re}\left(\mathbf{Z}_{xx}\right)\mathrm{Re}\left(\mathbf{Z}_{yy}\right) - \mathrm{Re}\left(\mathbf{Z}_{yx}\right)\mathrm{Re}\left(\mathbf{Z}_{xy}\right) \qquad \text{(D – 14)}$$

(Caldwell et al., 2004). The phase tensor plot is constructed by

$$\begin{bmatrix} \mathbf{\Phi}_{11} & \mathbf{\Phi}_{12} \\ \mathbf{\Phi}_{21} & \mathbf{\Phi}_{22} \end{bmatrix} \begin{bmatrix} \cos\alpha \\ \sin\alpha \end{bmatrix} = \begin{bmatrix} x \\ y \end{bmatrix} \qquad \text{(D – 15)}$$

which can be thought of as a mapping of one vector into another (Caldwell et al., 2004). Two invariants that are sometimes used to shade in the ellipse are the maximum phase and the minimum phase and are represented by the following equations

$$\mathbf{\Phi}_{\min} = \left(\mathbf{\Phi}_1^2 + \mathbf{\Phi}_3^2\right)^{\frac{1}{2}} - \left(\mathbf{\Phi}_1^2 + \mathbf{\Phi}_3^2 - \mathbf{\Phi}_2^2\right)^{\frac{1}{2}} \qquad \text{(D – 16)}$$

$$\mathbf{\Phi}_{\max} = \left(\mathbf{\Phi}_1^2 + \mathbf{\Phi}_3^2\right)^{\frac{1}{2}} + \left(\mathbf{\Phi}_1^2 + \mathbf{\Phi}_3^2 - \mathbf{\Phi}_2^2\right)^{\frac{1}{2}} \qquad \text{(D – 17)}$$

where

$$\mathbf{\Phi}_1 = \frac{1}{2}\left(\mathbf{\Phi}_{11} + \mathbf{\Phi}_{22}\right) \qquad \text{(D – 18)}$$

$$\mathbf{\Phi}_2 = \left(\mathbf{\Phi}_{11}\mathbf{\Phi}_{22} - \mathbf{\Phi}_{12}\mathbf{\Phi}_{21}\right)^{\frac{1}{2}} \qquad \text{(D – 19)}$$

$$\mathbf{\Phi}_3 = \frac{1}{2}\left(\mathbf{\Phi}_{12} - \mathbf{\Phi}_{21}\right), \qquad \text{(D – 20)}$$

(Caldwell et al., 2004). The invariant displayed in Figure 43 to shade in the phase tensor plots is the maximum phase, Φ_{max} (Pmax), which is also the term that is used to normalize the plots.

APPENDIX E

MT SITE COORDINATES

Table 4. Coordinates for MT Sounding Sites (NAD27 and UTM Zone 13)

MT Site	Northing	Easting	Latitude	Longitude	Elevation
SDB-525	3939450	380191	35°35'36.00"N	106°19'21.00"W	1605
SDB-526	3939289	380743	35°35'31.00"N	106°18'59.00"W	1610
SDB-527	3938911	381342	35°35'19.00"N	106°18'35.00"W	1613
SDB-701	3937852	381398	35°34'44.66"N	106°18'32.20"W	1660
SDB-702	3937810	381497	35°34'43.34"N	106°18'28.25"W	1661
SDB-703	3937378	381659	35°34'29.39"N	106°18'21.59"W	1670
SDB-704	3937258	381749	35°34'25.53"N	106°18'17.95"W	1672
SDB-501	3936225	381967	35°33'52.10"N	106°18'08.75"W	1671
SDB-502	3936197	382063	35°33'51.24"N	106°18'04.92"W	1671
SDB-503	3936170	382159	35°33'50.40"N	106°18'01.09"W	1672
SDB-504	3936142	382255	35°33'49.53"N	106°17'57.27"W	1672
SDB-505	3936114	382351	35°33'48.67"N	106°17'53.44"W	1672
SDB-506	3936086	382447	35°33'47.80"N	106°17'49.61"W	1673
SDB-507	3936059	382543	35°33'46.96"N	106°17'45.78"W	1673
SDB-508	3936031	382639	35°33'46.10"N	106°17'41.96"W	1674
SDB-509	3936004	382736	35°33'45.26"N	106°17'38.09"W	1675
SDB-510	3935976	382832	35°33'44.39"N	106°17'34.26"W	1676
SDB-511	3935949	382928	35°33'43.56"N	106°17'30.44"W	1677
SDB-512	3935921	383024	35°33'42.69"N	106°17'26.61"W	1678
SDB-513	3935894	383121	35°33'41.85"N	106°17'22.74"W	1678
SDB-514	3935867	383217	35°33'41.02"N	106°17'18.92"W	1678
SDB-515	3935840	383313	35°33'40.18"N	106°17'15.09"W	1679
SDB-516	3935813	383409	35°33'39.35"N	106°17'11.26"W	1679
SDB-517	3935780	383503	35°33'38.32"N	106°17'07.51"W	1679
SDB-518	3935746	383597	35°33'37.25"N	106°17'03.76"W	1679
SDB-519	3935713	383692	35°33'36.22"N	106°16'59.97"W	1679
SDB-520	3935680	383786	35°33'35.19"N	106°16'56.22"W	1678

Table 4. (continued)

MT Site	Northing	Easting	Latitude	Longitude	Elevation
SDB-521	3935643	383879	35°33'34.03"N	106°16'52.51"W	1679
SDB-522	3935608	383973	35°33'32.93"N	106°16'48.76"W	1678
SDB-523	3935575	384067	35°33'31.90"N	106°16'45.01"W	1679
SDB-524	3935542	384162	35°33'30.87"N	106°16'41.22"W	1679
SDB-201	3935503	384275	35°33'29.65"N	106°16'36.71"W	1679
SDB-202	3935475	384371	35°33'28.79"N	106°16'32.89"W	1679
SDB-203	3935447	384467	35°33'27.92"N	106°16'29.06"W	1680
SDB-204	3935419	384563	35°33'27.05"N	106°16'25.23"W	1680
SDB-205	3935391	384659	35°33'26.18"N	106°16'21.41"W	1680
SDB-206	3935363	384755	35°33'25.31"N	106°16'17.58"W	1680
SDB-207	3935335	384851	35°33'24.44"N	106°16'13.75"W	1680
SDB-208	3935307	384947	35°33'23.57"N	106°16'09.93"W	1681
SDB-209	3935279	385043	35°33'22.71"N	106°16'06.10"W	1682
SDB-210	3935251	385139	35°33'21.84"N	106°16'02.27"W	1682
SDB-001	3933011	385217	35°32'09.16"N	106°15'58.05"W	1679
SDB-211	3935223	385234	35°33'20.97"N	106°15'58.49"W	1682
SDB-212	3935195	385330	35°33'20.10"N	106°15'54.66"W	1682
SDB-213	3935167	385426	35°33'19.23"N	106°15'50.83"W	1683
SDB-214	3935139	385522	35°33'18.36"N	106°15'47.01"W	1683
SDB-215	3935110	385617	35°33'17.46"N	106°15'43.22"W	1684
SDB-216	3935081	385713	35°33'16.56"N	106°15'39.39"W	1684
SDB-217	3935052	385808	35°33'15.66"N	106°15'35.60"W	1684
SDB-218	3935024	385904	35°33'14.79"N	106°15'31.78"W	1684
SDB-219	3934996	386000	35°33'13.92"N	106°15'27.95"W	1684
SDB-220	3934968	386096	35°33'13.05"N	106°15'24.13"W	1684
SDB-221	3934939	386191	35°33'12.15"N	106°15'20.34"W	1683
SDB-222	3934910	386287	35°33'11.25"N	106°15'16.51"W	1682
SDB-223	3934881	386383	35°33'10.35"N	106°15'12.68"W	1683

Table 4. (continued)

MT Site	Northing	Easting	Latitude	Longitude	Elevation
SDB-224	3934853	386479	35°33'09.48"N	106°15'08.86"W	1684
SDB-225	3934824	386574	35°33'08.58"N	106°15'05.07"W	1684
SDB-226	3934796	386670	35°33'07.71"N	106°15'01.24"W	1683
SDB-227	3934767	386766	35°33'06.80"N	106°14'57.42"W	1684
SDB-228	3934739	386862	35°33'05.94"N	106°14'53.59"W	1685
SDB-229	3934711	386957	35°33'05.07"N	106°14'49.81"W	1686
SDB-301	3933932	386998	35°32'39.80"N	106°14'47.79"W	1696
SDB-230	3934683	387053	35°33'04.20"N	106°14'45.98"W	1687
SDB-302	3933936	387100	35°32'39.97"N	106°14'43.74"W	1697
SDB-231	3934655	387149	35°33'03.33"N	106°14'42.15"W	1687
SDB-303	3933938	387203	35°32'40.08"N	106°14'39.65"W	1698
SDB-232	3934627	387245	35°33'02.46"N	106°14'38.33"W	1687
SDB-304	3933941	387306	35°32'40.22"N	106°14'35.56"W	1699
SDB-233	3934599	387340	35°33'01.59"N	106°14'34.54"W	1686
SDB-305	3933951	387404	35°32'40.59"N	106°14'31.67"W	1699
SDB-234	3934571	387436	35°33'00.72"N	106°14'30.71"W	1685
SDB-306	3933948	387509	35°32'40.53"N	106°14'27.50"W	1700
SDB-235	3934542	387531	35°32'59.82"N	106°14'26.93"W	1683
SDB-307	3933952	387602	35°32'40.70"N	106°14'23.81"W	1701
SDB-236	3934514	387627	35°32'58.95"N	106°14'23.10"W	1683
SDB-308	3933956	387701	35°32'40.87"N	106°14'19.88"W	1702
SDB-237	3934486	387722	35°32'58.08"N	106°14'19.32"W	1683
SDB-309	3933945	387799	35°32'40.55"N	106°14'15.99"W	1702
SDB-101	3934070	387801	35°32'44.61"N	106°14'15.97"W	1696
SDB-238	3934458	387818	35°32'57.21"N	106°14'15.49"W	1682
SDB-310	3933960	387885	35°32'41.07"N	106°14'12.58"W	1701
SDB-102	3934069	387895	35°32'44.61"N	106°14'12.24"W	1697
SDB-239	3934430	387914	35°32'56.34"N	106°14'11.66"W	1681

Table 4. (continued)

MT Site	Northing	Easting	Latitude	Longitude	Elevation
SDB-002	3933346	387965	35°32'21.17"N	106°14'09.08"W	1706
SDB-103	3934064	387997	35°32'44.49"N	106°14'08.19"W	1697
SDB-311	3933960	388004	35°32'41.12"N	106°14'07.86"W	1701
SDB-240	3934402	388011	35°32'55.47"N	106°14'07.80"W	1678
SDB-104	3934060	388100	35°32'44.41"N	106°14'04.09"W	1696
SDB-312	3933962	388103	35°32'41.23"N	106°14'03.93"W	1699
SDB-241	3934374	388107	35°32'54.60"N	106°14'03.97"W	1676
SDB-105	3934054	388198	35°32'44.25"N	106°14'00.20"W	1696
SDB-313	3933957	388201	35°32'41.10"N	106°14'00.03"W	1698
SDB-106	3934051	388297	35°32'44.19"N	106°13'56.27"W	1690
SDB-314	3933957	388300	35°32'41.14"N	106°13'56.10"W	1696
SDB-107	3934059	388396	35°32'44.49"N	106°13'52.34"W	1691
SDB-315	3933954	388402	35°32'41.09"N	106°13'52.05"W	1695
SDB-108	3934085	388488	35°32'45.38"N	106°13'48.70"W	1689
SDB-316	3933954	388502	35°32'41.13"N	106°13'48.08"W	1697
SDB-109	3934112	388580	35°32'46.29"N	106°13'45.06"W	1686
SDB-110	3934142	388672	35°32'47.30"N	106°13'41.42"W	1682
SDB-111	3934147	388753	35°32'47.49"N	106°13'38.21"W	1682
SDB-112	3934139	388863	35°32'47.28"N	106°13'33.84"W	1685
SDB-113	3934135	388962	35°32'47.19"N	106°13'29.90"W	1686
SDB-114	3934141	389055	35°32'47.42"N	106°13'26.21"W	1686
SDB-115	3934165	389151	35°32'48.24"N	106°13'22.41"W	1686
SDB-116	3934189	389250	35°32'49.06"N	106°13'18.49"W	1686
SDB-117	3934209	389346	35°32'49.75"N	106°13'14.69"W	1686
SDB-118	3934224	389439	35°32'50.27"N	106°13'11.01"W	1688
SDB-003	3933307	391138	35°32'21.18"N	106°12'03.08"W	1866
SDB-004	3934050	393338	35°32'46.15"N	106°10'36.09"W	1867

Sites highlighted in grey were not used in the smooth 2-D inversion model.

APPENDIX F

2-D INVERSION MODEL FITS TO D+

SMOOTHED DATA FROM WEST TO EAST

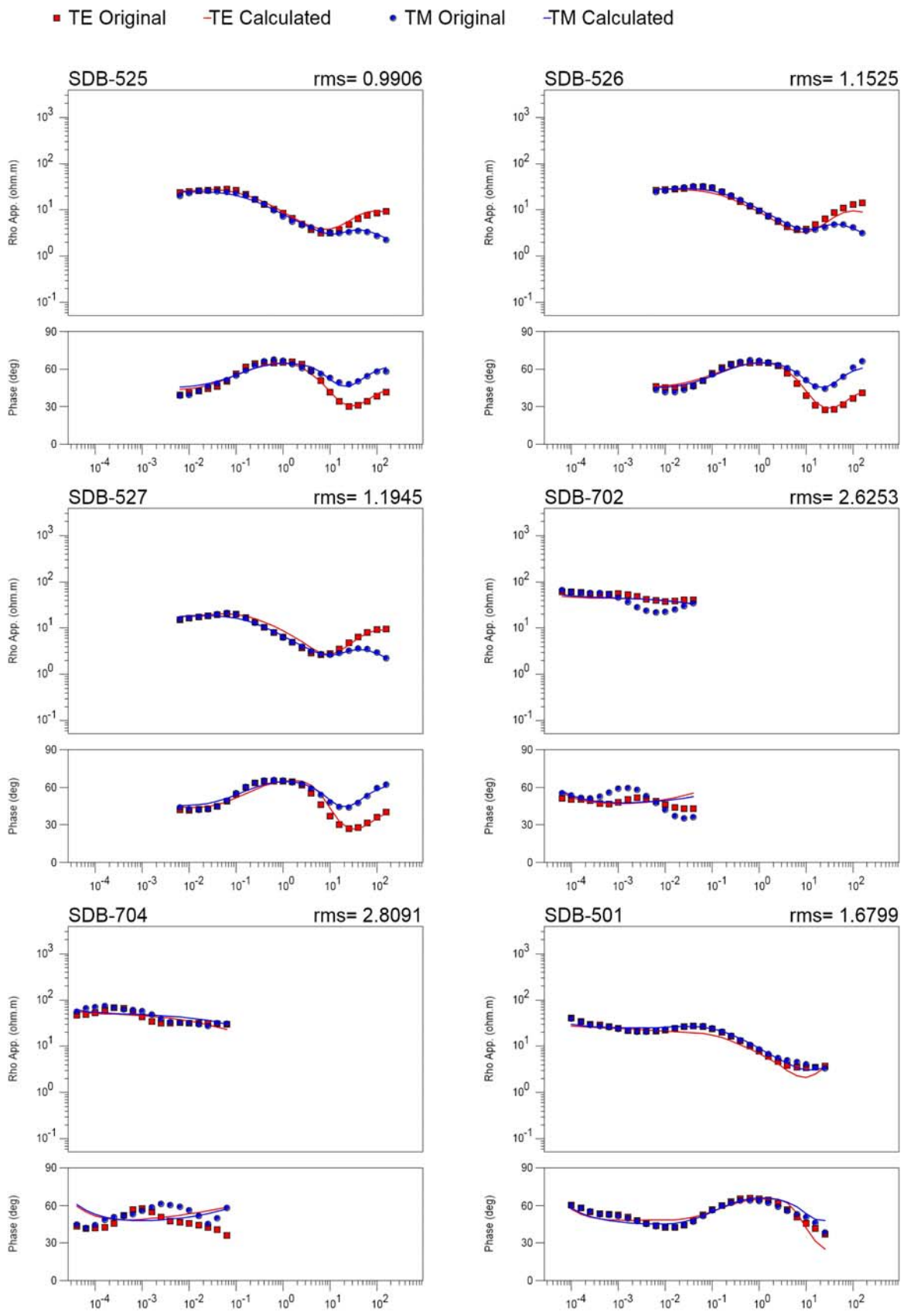
TE Original
TE Calculated
TM Original
TM Calculated
SDB-525
rms= 0.9906
SDB-526
rms= 1.1525
SDB-527
rms= 1.1945
SDB-702
rms= 2.6253
SDB-704
rms= 2.8091
SDB-501
rms= 1.6799
Rho App. (ohm.m)
Phase (deg)

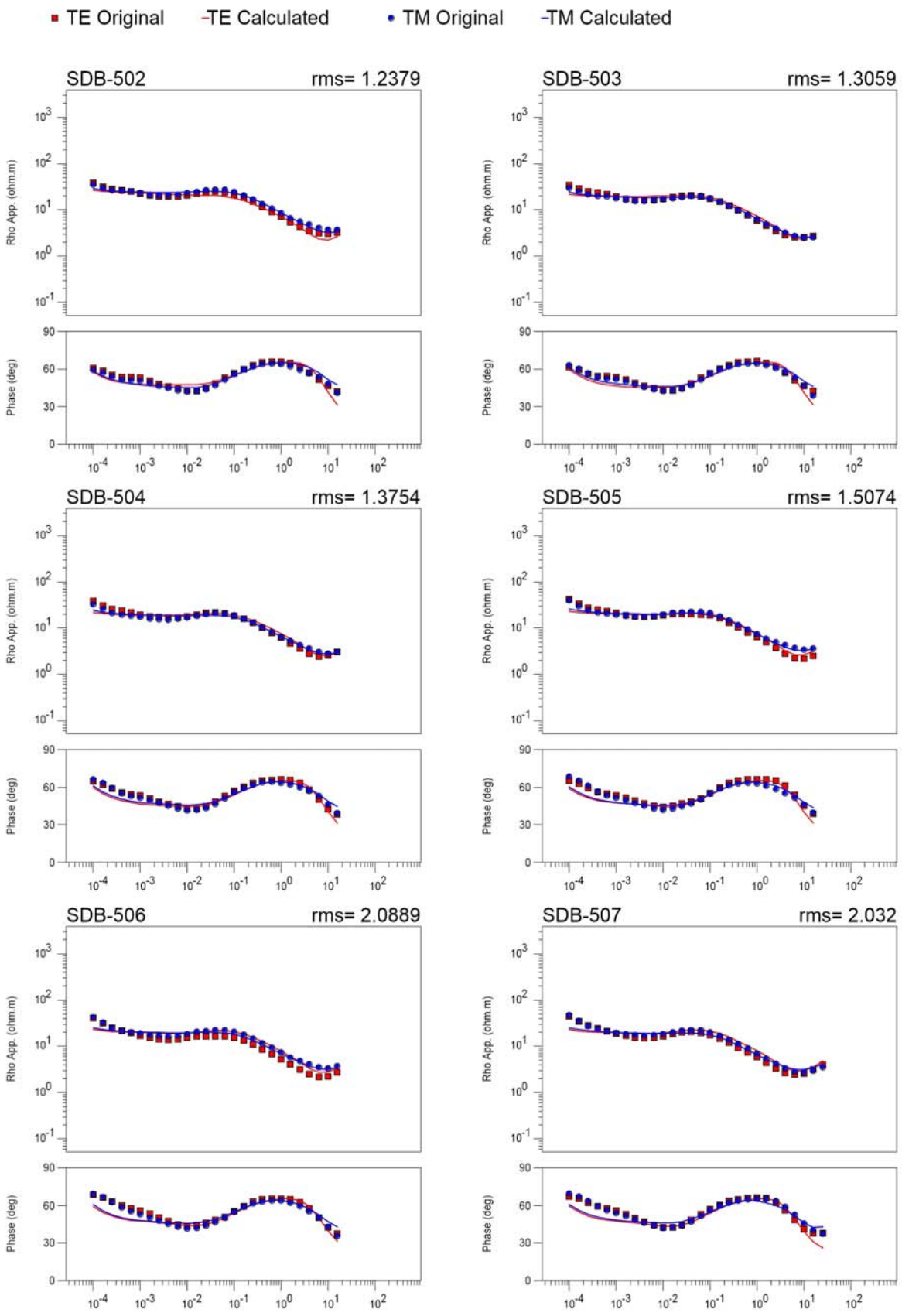
TE Original
TE Calculated
TM Original
TM Calculated
SDB-502
rms= 1.2379
SDB-503
rms= 1.3059
SDB-504
rms= 1.3754
SDB-505
rms= 1.5074
SDB-506
rms= 2.0889
SDB-507
rms= 2.032
Rho App. (ohm.m)
Phase (deg)

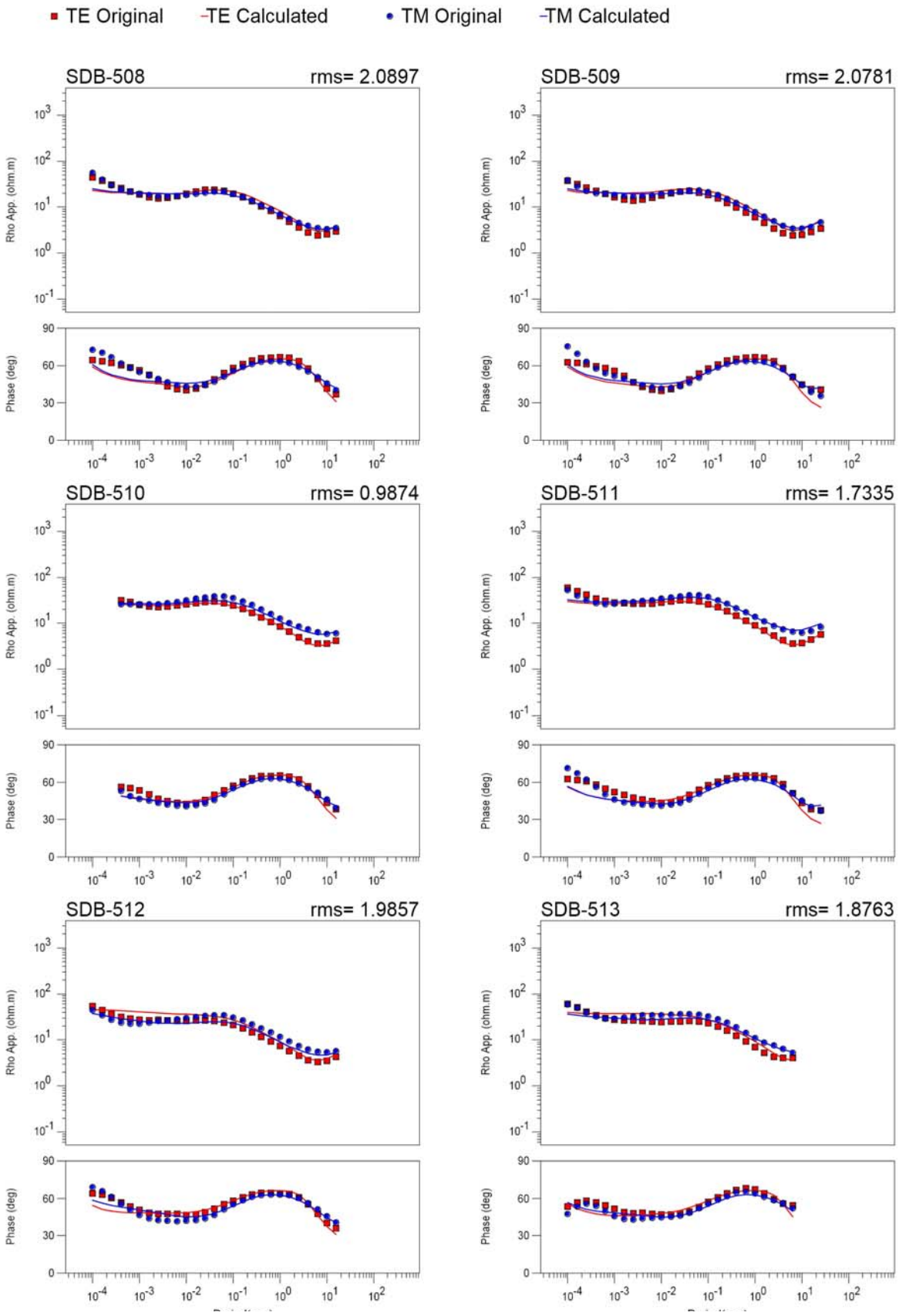
TE Original
TE Calculated
TM Original
TM Calculated
SDB-508
rms= 2.0897
SDB-509
rms= 2.0781
SDB-510
rms= 0.9874
SDB-511
rms= 1.7335
SDB-512
rms= 1.9857
SDB-513
rms= 1.8763
Rho App. (ohm.m)
Phase (deg)

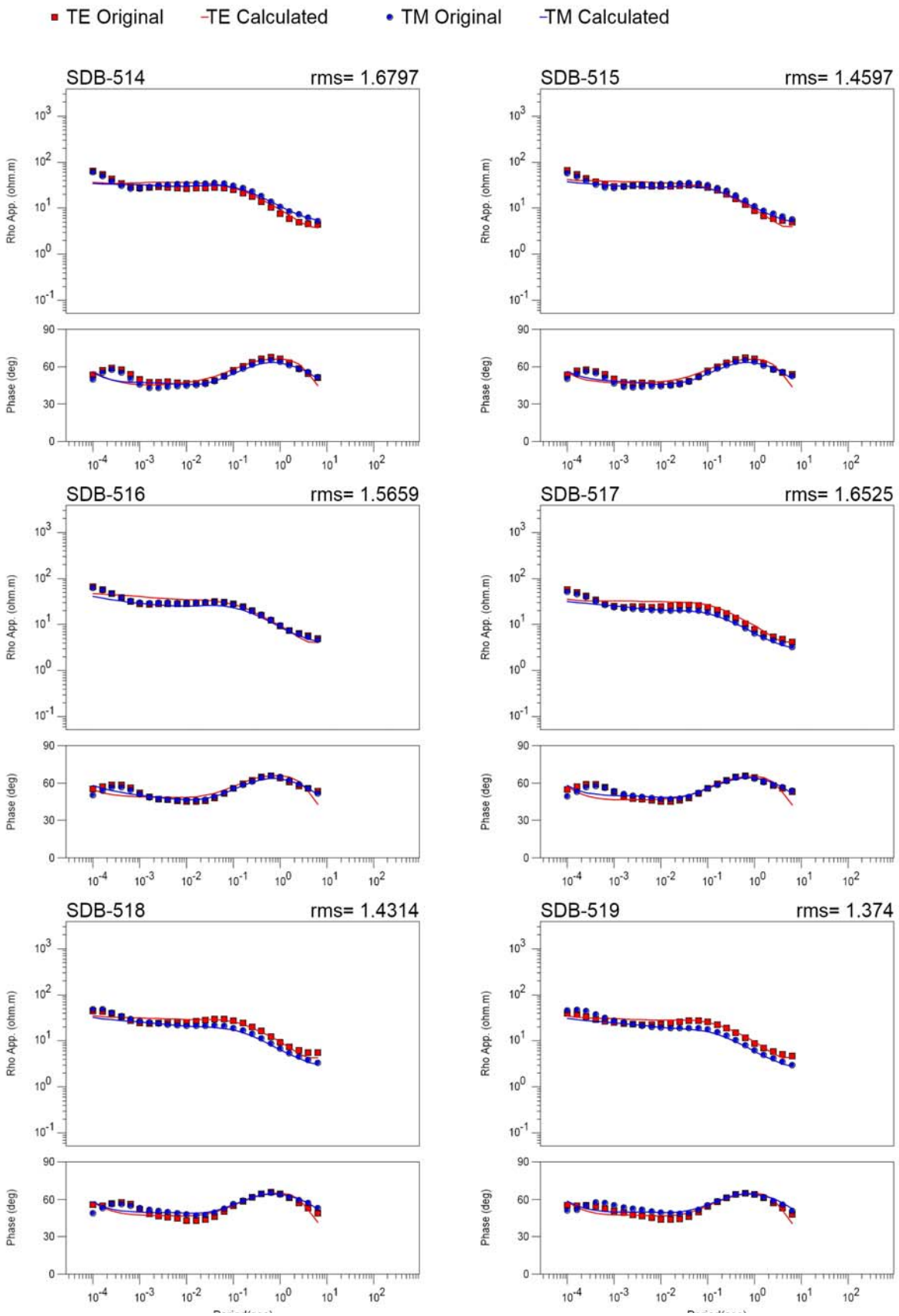
TE Original
TE Calculated
TM Original
TM Calculated
SDB-514
rms= 1.6797
SDB-515
rms= 1.4597
SDB-516
rms= 1.5659
SDB-517
rms= 1.6525
SDB-518
rms= 1.4314
SDB-519
rms= 1.374
Rho App. (ohm.m)
Phase (deg)

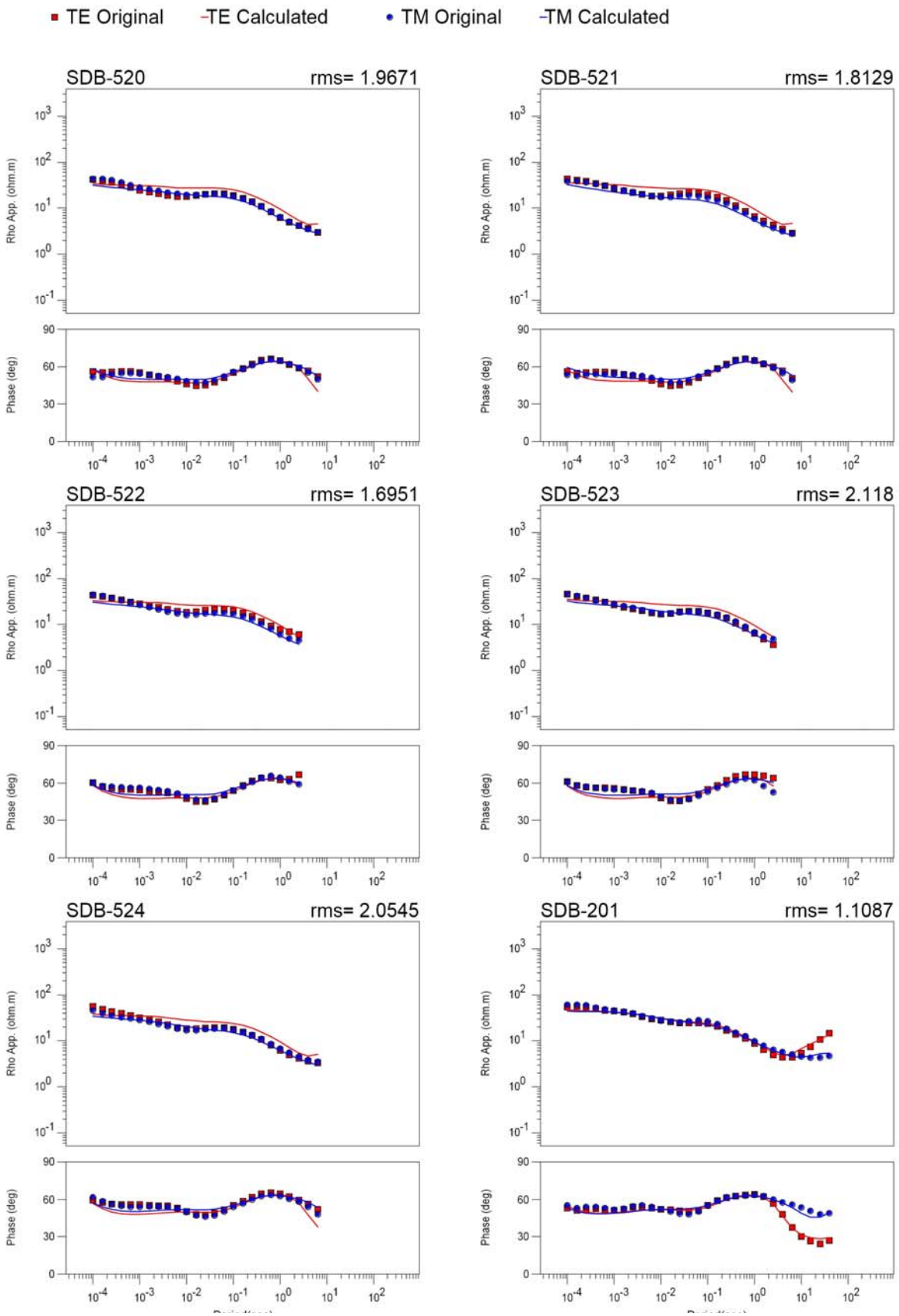
TE Original
TE Calculated
TM Original
TM Calculated
SDB-520
rms= 1.9671
SDB-521
rms= 1.8129
SDB-522
rms= 1.6951
SDB-523
rms= 2.118
SDB-524
rms= 2.0545
SDB-201
rms= 1.1087
Rho App. (ohm.m)
Phase (deg)

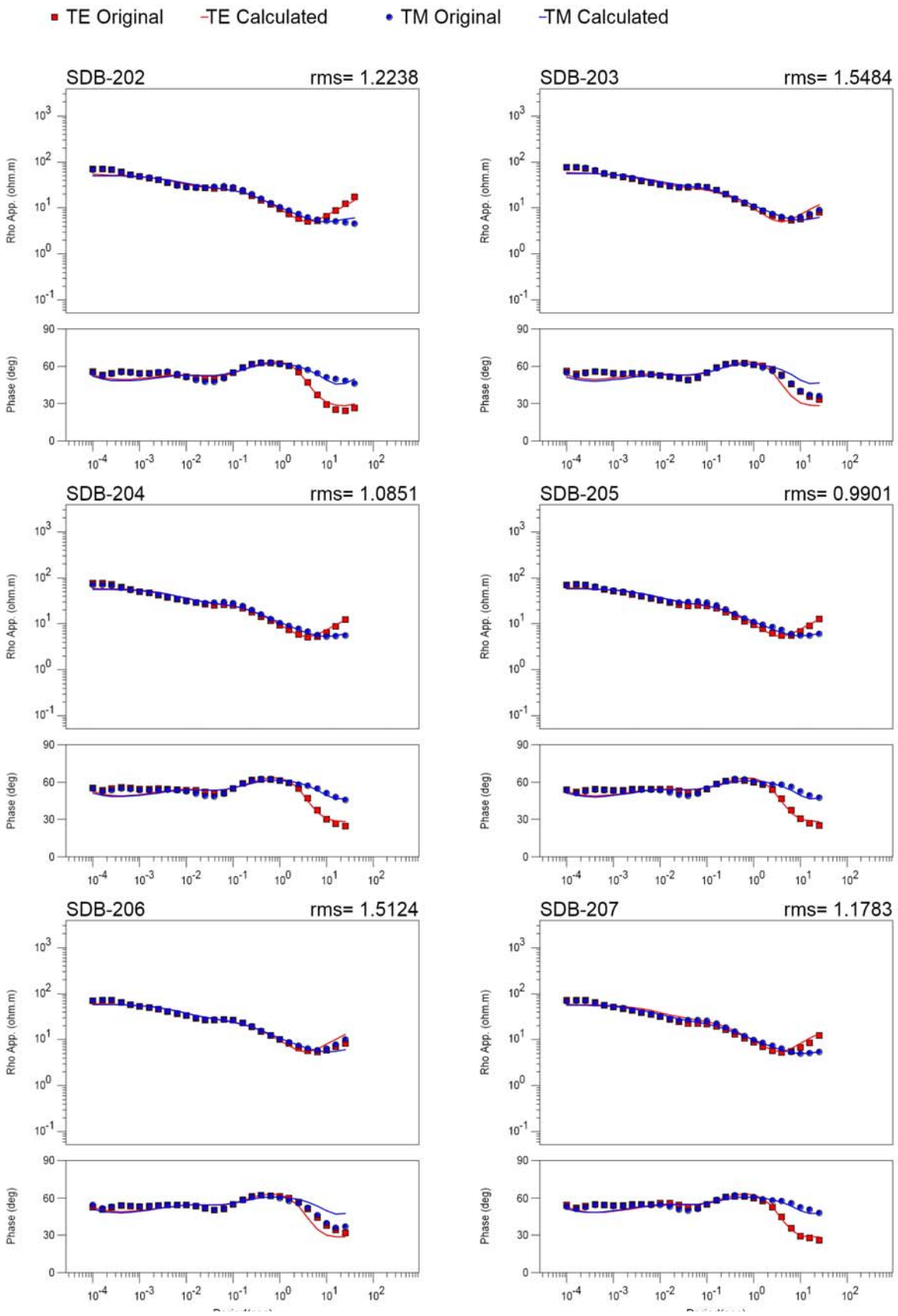
TE Original
TE Calculated
TM Original
TM Calculated
SDB-202
rms= 1.2238
SDB-203
rms= 1.5484
SDB-204
rms= 1.0851
SDB-205
rms= 0.9901
SDB-206
rms= 1.5124
SDB-207
rms= 1.1783
Rho App. (ohm.m)
Phase (deg)

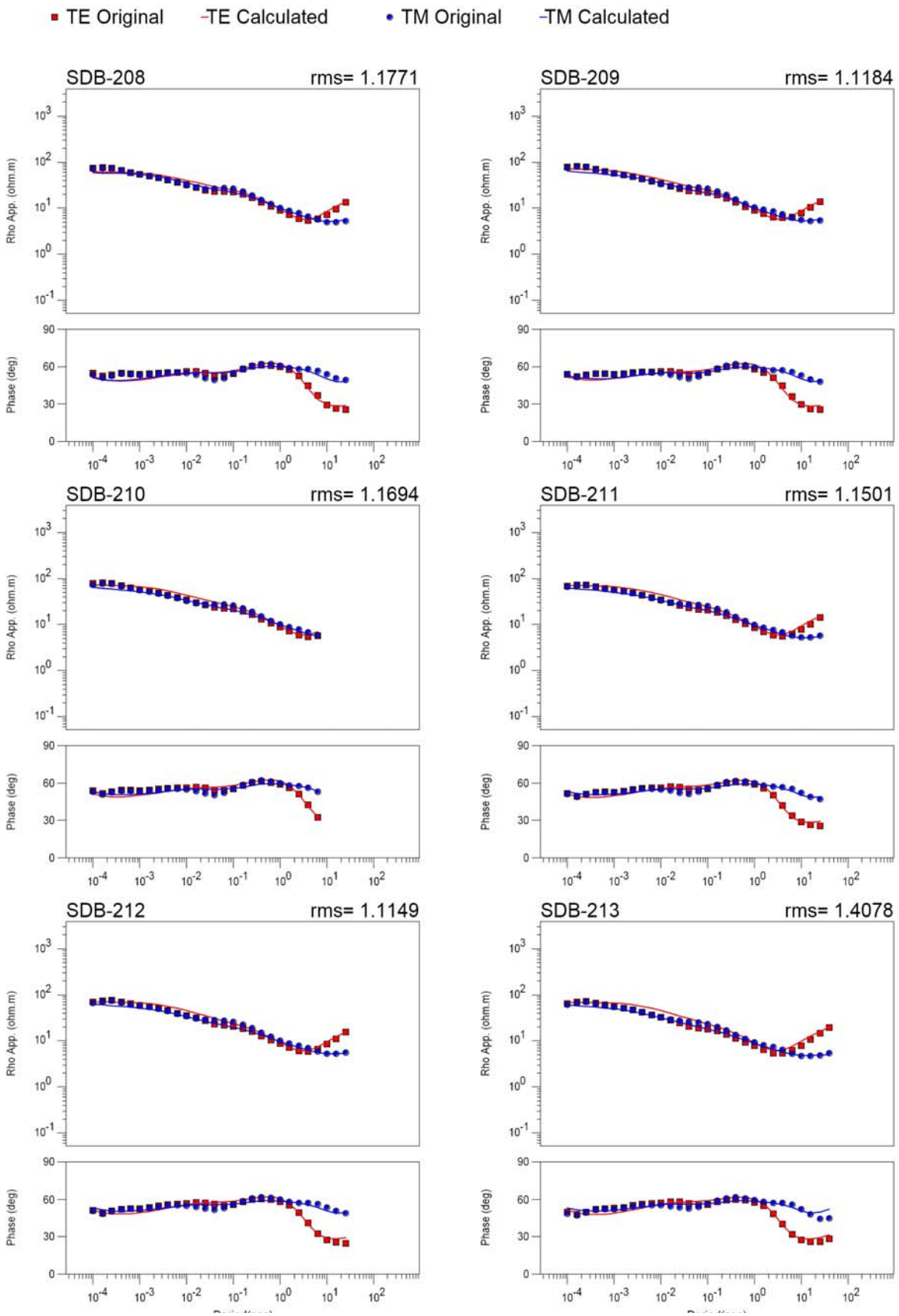
TE Original
TE Calculated
TM Original
TM Calculated
SDB-208
rms= 1.1771
SDB-209
rms= 1.1184
SDB-210
rms= 1.1694
SDB-211
rms= 1.1501
SDB-212
rms= 1.1149
SDB-213
rms= 1.4078
Rho App. (ohm.m)
Phase (deg)

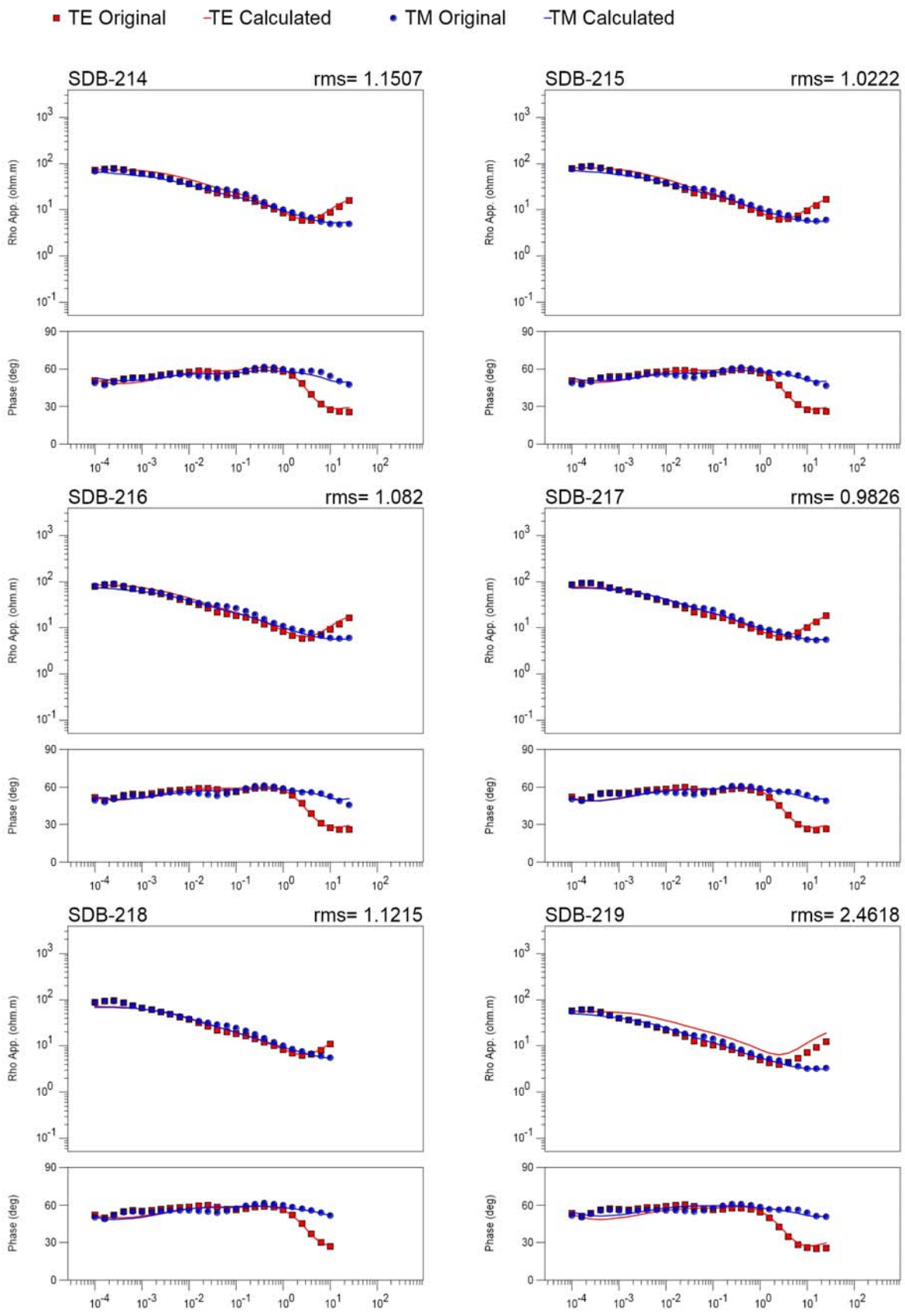
TE Original
TE Calculated
TM Original
TM Calculated
SDB-214
rms= 1.1507
SDB-215
rms= 1.0222
SDB-216
rms= 1.082
SDB-217
rms= 0.9826
SDB-218
rms= 1.1215
SDB-219
rms= 2.4618
Rho App. (ohm.m)
Phase (deg)

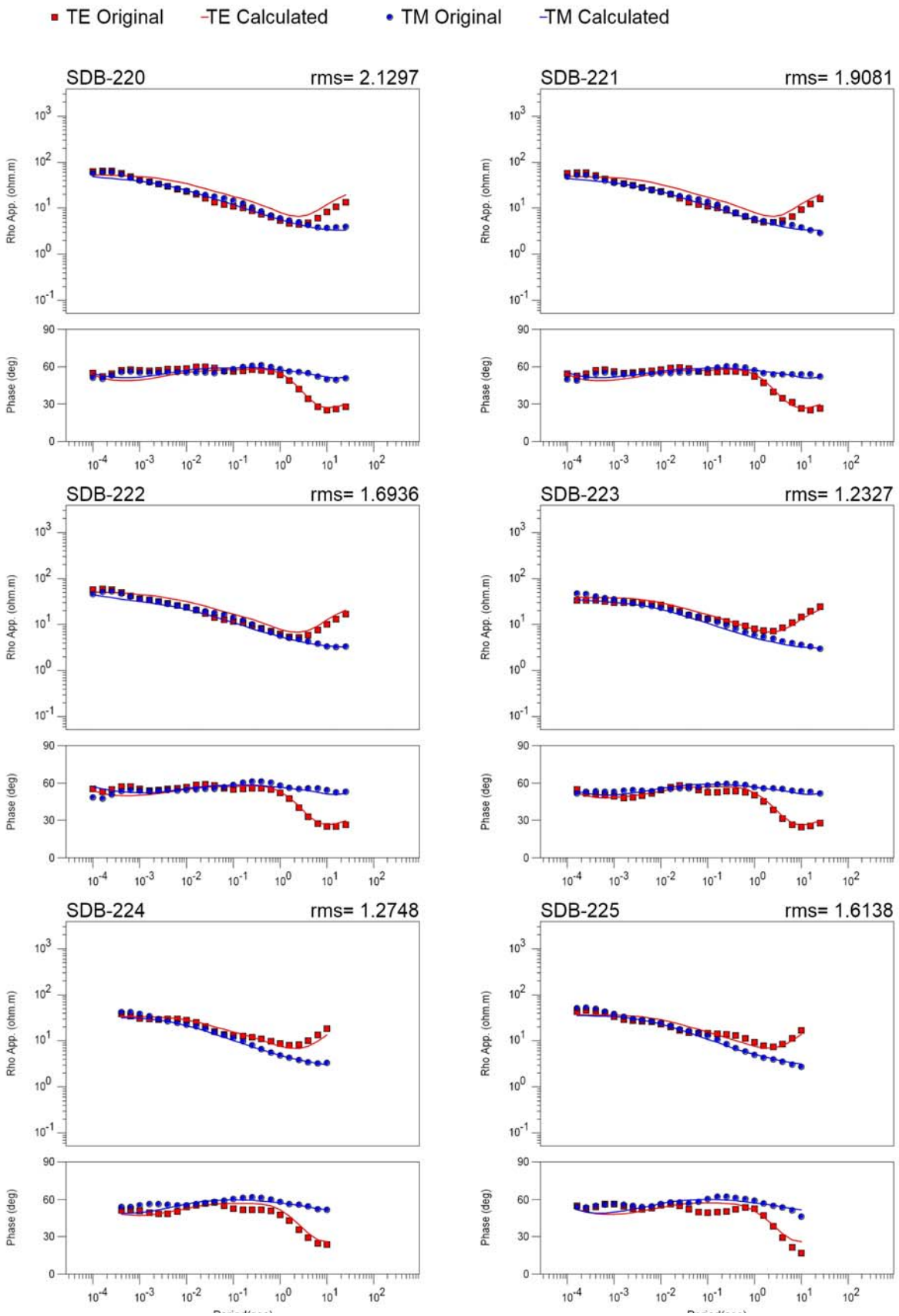
TE Original
TE Calculated
TM Original
TM Calculated
SDB-220
rms= 2.1297
SDB-221
rms= 1.9081
SDB-222
rms= 1.6936
SDB-223
rms= 1.2327
SDB-224
rms= 1.2748
SDB-225
rms= 1.6138
Rho App. (ohm.m)
Phase (deg)

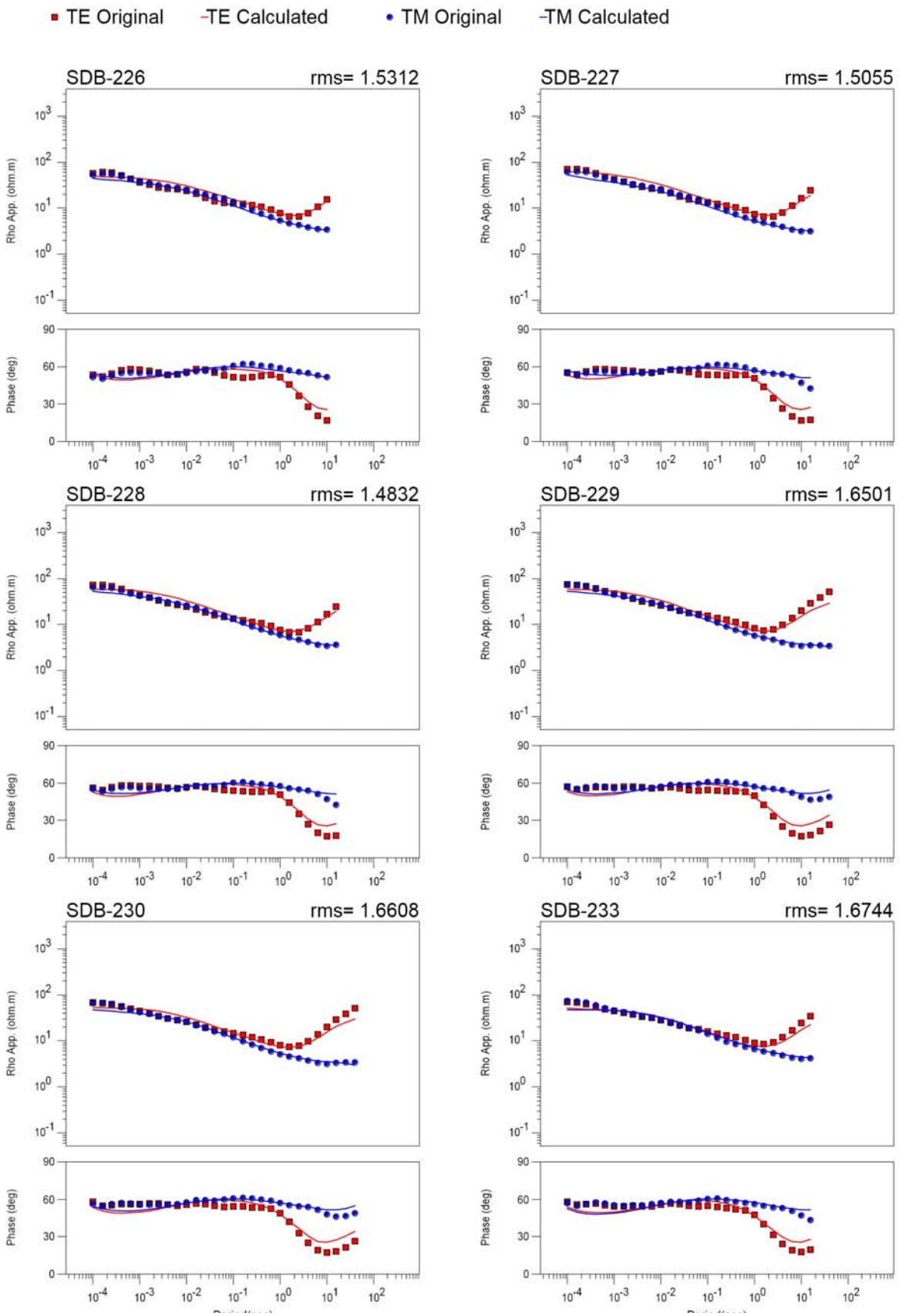
TE Original
TE Calculated
TM Original
TM Calculated
SDB-226
rms= 1.5312
SDB-227
rms= 1.5055
SDB-228
rms= 1.4832
SDB-229
rms= 1.6501
SDB-230
rms= 1.6608
SDB-233
rms= 1.6744
Rho App. (ohm.m)
Phase (deg)

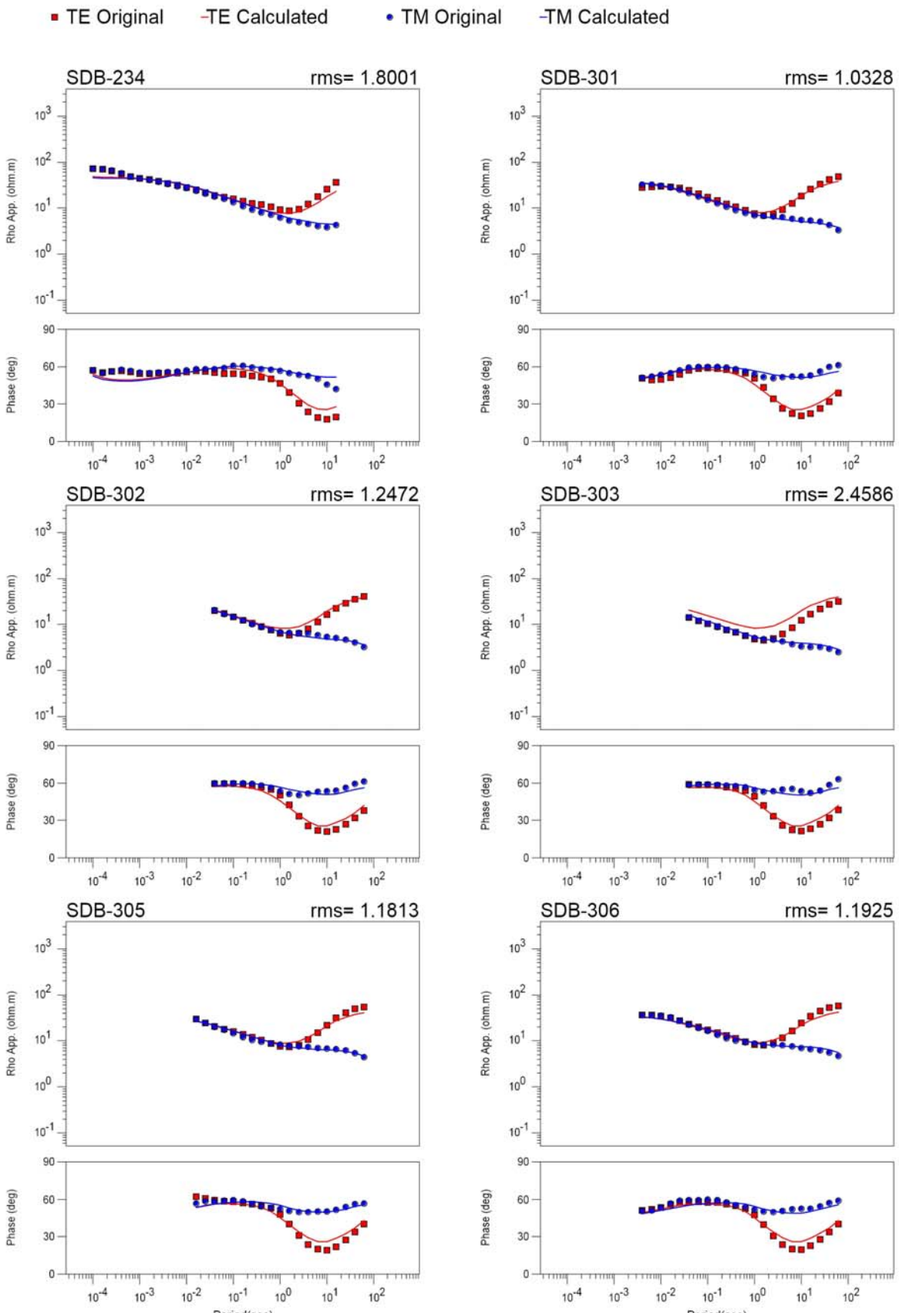
TE Original
TE Calculated
TM Original
TM Calculated
SDB-234
rms= 1.8001
SDB-301
rms= 1.0328
SDB-302
rms= 1.2472
SDB-303
rms= 2.4586
SDB-305
rms= 1.1813
SDB-306
rms= 1.1925
Rho App. (ohm.m)
Phase (deg)

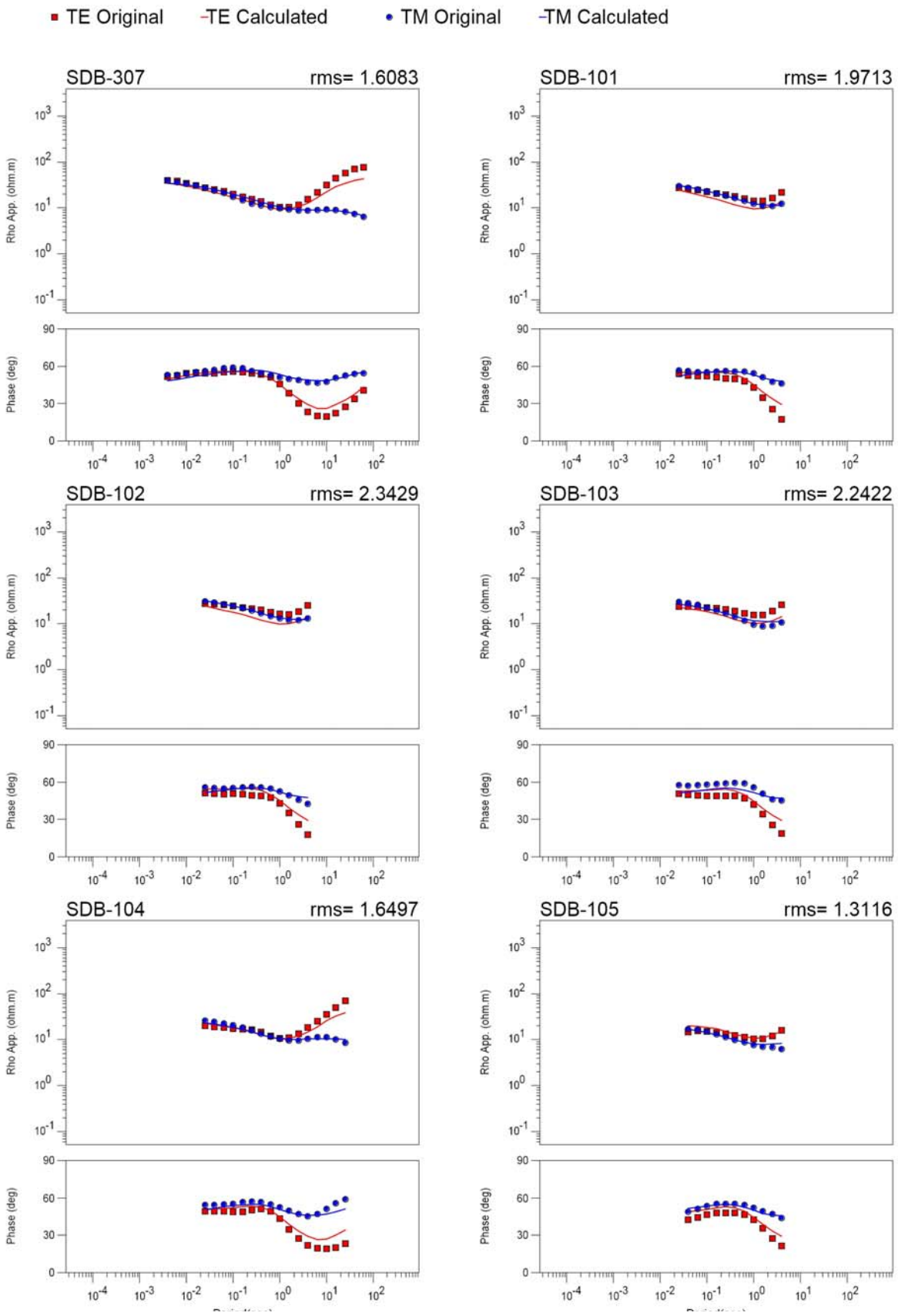
TE Original
TE Calculated
TM Original
TM Calculated
SDB-307
rms= 1.6083
SDB-101
rms= 1.9713
SDB-102
rms= 2.3429
SDB-103
rms= 2.2422
SDB-104
rms= 1.6497
SDB-105
rms= 1.3116
Rho App. (ohm.m)
Phase (deg)

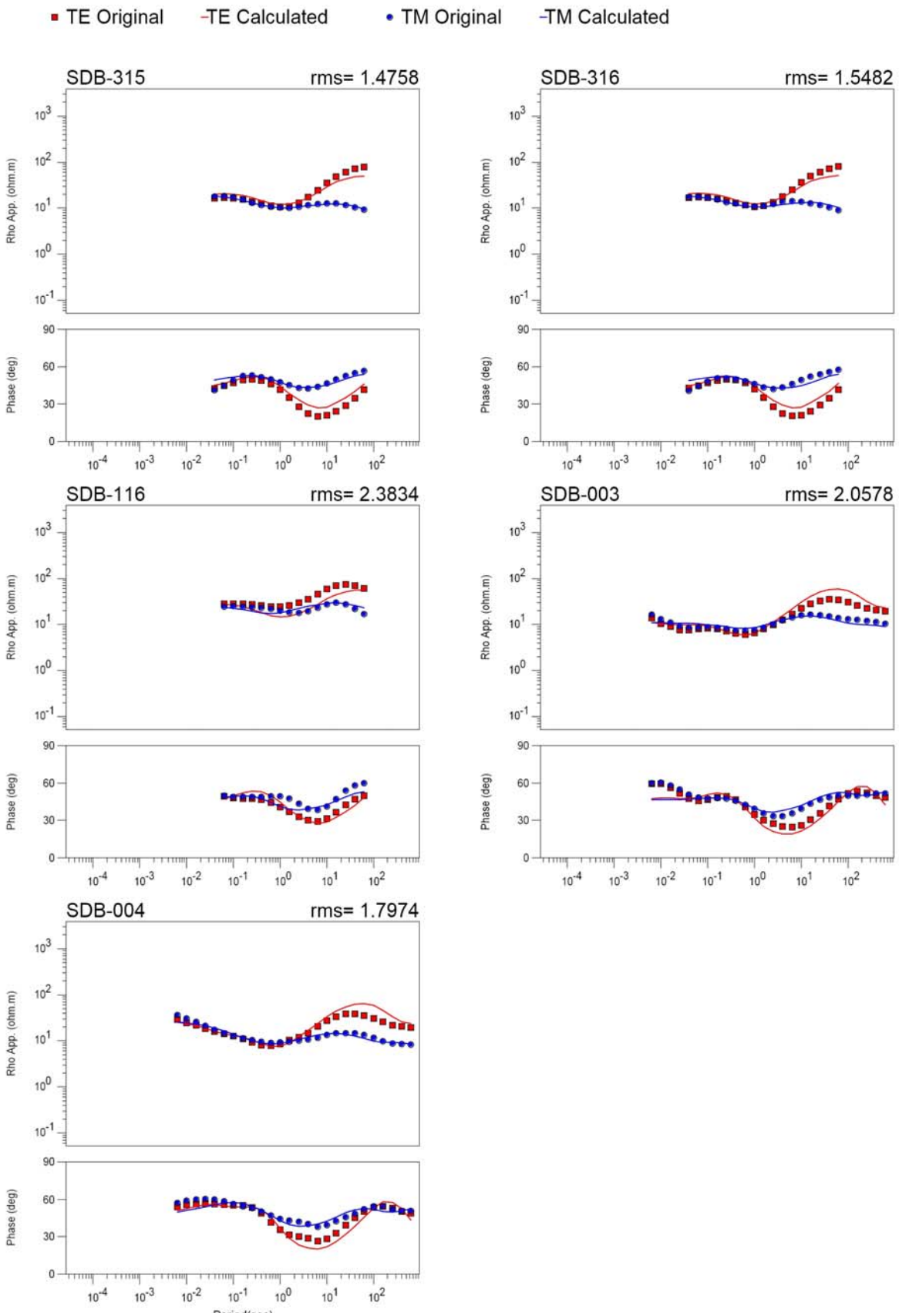
TE Original
TE Calculated
TM Original
TM Calculated
SDB-315
rms= 1.4758
SDB-316
rms= 1.5482
SDB-116
rms= 2.3834
SDB-003
rms= 2.0578
SDB-004
rms= 1.7974
Rho App. (ohm.m)
Phase (deg)

ABSTRACT OF THE THESIS

Magnetotelluric Investigation of the Santo Domingo Basin, Rio Grande Rift, New Mexico

by
Peter Karl Winther
Master of Science in Geological Sciences
San Diego State University, 2009

Magnetotelluric (MT) investigations of the Santo Domingo Basin were made in 2000-2007 to assess the deep stratigraphy and tectonics of an intra rift basin. The studies were conducted during the SAGE (Summer of Applied Geophysical Experience) program to provide 'hands-on' learning experiences for students and to evaluate the local hydrologic regime. Most MT soundings were accomplished using Quantec Geoscience's Titan 24 MT system. The Titan system is a distributed array MT instrument that allows the collection of up to 24 MT soundings simultaneously with a station spacing of 100 m. Sixty-five Titan MT soundings were collected along a 6.4 km-long profile where a petroleum exploration seismic survey was recorded during the 1970's. The MT data were modeled using a smooth, two-dimensional (2-D) inversion code developed by Geosystem, Inc. Modeled resistivity values vary from 2-1000 ohm-m in the 2 - 4.5 km-thick sedimentary section. Resistivities exceed 1000 ohm-m in the basement interpreted to underlie the sediments. The sedimentary sequence indicates three distinct regimes: (1) an upper, unsaturated and freshwater saturated, basin-fill that ranges from 350 - 800 m-deep with resistivities of 8 - 85 ohm-m, (2) a deeper, mostly conductive region with higher brine and/or clay concentrations approximately 3 km thick with resistivities varying between 2 - 100 ohm-m and (3) a resistive sedimentary cover over the crystalline basement that ranges from 100 - 1000 ohm-m. Tectonic interpretations of the 2-D MT inversion model agree with the locations of several fault traces extended into the basin by the U. S. Geological Survey from aeromagnetic interpretations. A geologic structure model for the area includes two grabens with the graben on the west down dropped with respect to the graben on the east.